
Yuji Hasegawa



DIPLOMARBEIT

Simultaneous Measurement of a Quantum Cheshire Cat

ausgeführt am Atominstitut
der Technischen Universität Wien
unter der Anleitung von

Associate Prof. Dipl.-Ing. Dr. Yuji Hasegawa

durch

Wenzel Kersten

Wallensteinstraße 50/6

1200 Wien

24. Mai 2017

Wenzel Kersten

Abstract

In 2014 the first experimental observation of the quantum Chesire Cat effect was made using neutron interferometry [T. Denkmayr et al., Nat. Commun. 5 (2014)]. By pre and postselecting the neutrons, i.e. adjusting the spin and path state, in which they enter the interferometer, and which state they need to have in order to reach the detector, a seemingly paradox situation can arise. A weak intermediate interaction involving the spin will have an influence on the intensity at the detector only on one arm of the interferometer – this is the cat's grin. Another interaction probing the path influences the intensity only on the other arm – the cat's body is spatially separated from its grin. Nevertheless, there is a drawback in the experiment of 2014; the interaction of the beam with a weak absorber used in order to measure the path is not of unitary nature and can only be made for one path at a time. A new experiment carried out in the course of this master thesis seeks to demonstrate this effect – the separation of body and grin – simultaneously, unlike the 2014 experiment, where measurements were made consecutively. For this purpose a new way of attaining the path information was implemented using the neutron's energy degree of freedom as a which-way marker, inspired by multiphoton exchange processes, that leave the spin unchanged. The experiment was conducted at the Institute Laue-Langevin in Grenoble, France. The final results qualitatively agree with the theory and show the separation of the cat from its grin.

Zusammenfassung

Im Jahr 2014 wurde zum ersten Mal die sogenannte Quanten-Grinsekatze in einem Neutronen-Interferometer beobachtet [T. Denkmayr et al., Nat. Commun. 5 (2014)]. Durch Prä- und Postselektion, d.h. die Auswahl des Spin- und Pfad-Zustandes, den Neutronen haben, wenn sie in das Interferometer kommen, und den sie brauchen, um den Detektor zu erreichen, kann eine scheinbar paradoxe Situation erzeugt werden. Eine schwache zwischenzeitliche Beeinflussung des Spins hat einen Einfluss auf die Intensität am Detektor nur auf einem Arm des Interferometers – dies ist das Grinsen der Katze. Eine andere Beeinflussung, die den Pfadzustand des Neutrons überprüft, ist nur auf dem anderen Arm wirksam – der Körper der Katze ist räumlich von ihrem Grinsen getrennt. Nichtsdestotrotz gibt es einen Nachteil am Experiment aus 2014; die Wechselwirkung des Neutronenstrahls mit einem schwachen Absorber, die zur Messung des Pfades eingesetzt wurde, ist nicht unitär und kann nur für jeweils einen der Pfade genutzt werden. Ein neues Experiment das im Zuge dieser Masterarbeit durchgeführt wurde, demonstriert den Effekt – die Aufteilung von Körper und Grinsen der Katze – gleichzeitig, im Unterschied zum Experiment aus 2014, bei dem die Messungen nacheinander erfolgten. Zu diesem Zweck wurde eine neue Möglichkeit zur Messung des Pfadzustandes implementiert, die den Energiefreiheitsgrad der Neutronen als Welcher-Weg-Markierung verwendet, inspiriert von Multiphoton-Austauschprozessen, die den Spin unverändert lassen. Dieses Experiment wurde am Institute Laue-Langevin in Grenoble, Frankreich durchgeführt. Das Messresultat stimmt qualitativ mit der theoretischen Beschreibung überein und zeigt die Trennung der Katze von ihrem Grinsen.

Acknowledgments

I want to thank my supervisor Yuji Hasegawa for giving me the opportunity to expand my knowledge of physics in an experimental way. Whenever questions arose, his door was always open and answers were willingly given.

Next I want to thank my colleagues Stephan Sponar and Hermann Geppert-Kleinrath, who were of great help in the planning and preparation of this work through their continuous support. I also owe thanks to Richard Wagner, Stefan Lindner and Bülent Demirel for their help during the practical phase of my experiment. I profited greatly from your shared knowledge.

Furthermore, I want to thank my fellow student David Ellmeyer, with whom learning for exams was always fun and entertaining. Without you I do not know how I would have fared in my studies.

I owe deep gratitude to my parents Emma and Thomas Kersten for supporting my academic education. You made it possible for me to pursue my interests and dreams.

Last but not least I want to thank Bernadette Wittmann, who is always there for me when I need her. Your support means everything to me.

Contents

1	Introduction	1
2	Cheshire Cat Emerging in Neutron Interferometry	3
2.1	Measurement in Quantum Mechanics	4
2.1.1	Weak Measurements	5
2.2	Weak Values	6
2.3	Experimental Studies of Weak Measurements/Weak Values	8
2.3.1	Direct Measurement of the Quantum Wavefunction	8
2.3.2	Ultrasensitive Beam Deflection Measurement via Interferometric Weak Value Amplification	10
2.4	Neutron Optical Approach	12
2.4.1	Neutron Interferometry	12
2.4.2	Neutron Spin: A Two-Level Quantum System	13
2.4.3	Manipulation of the Spin: Spin-Rotation	15
2.5	Spin and Path Weak Values and the Quantum Cheshire Cat in Neutron Optical Experiments	16
2.6	Other Experimental and Further Theoretical Studies of the Quantum Cheshire Cat Effect	17
3	Theory	19
3.1	Scheme of the Previous Quantum Cheshire Cat Experiment	19
3.2	Resonant Frequency Spin Flippers	22
3.3	Simultaneous Spin Localization Measurement	25
3.4	Realization of a Which Way Measurement for Neutrons	26
3.5	Energy Manipulator Coils	28
3.5.1	Theoretical Treatment	28
3.5.2	Associated Experiment by Summhammer	30
3.6	Experimental Scheme	32
3.6.1	Calculation of the O Beam Intensity	33
4	Neutron Optical Setup	37
4.1	Neutron Source	37
4.2	Neutron Detectors	37
4.3	Perfect Crystal Interferometer and Phase Shifter Plates	38

4.4	Polarizing Magnets	42
4.5	Supermirror	42
4.6	Guide Field	43
4.7	Optical Bench	44
4.8	Spin-Manipulation Assembly	45
4.8.1	Coil Assembly Dimensions	47
4.8.2	EM-Coil Field Simulation	49
4.9	Measurement Control and Data Acquisition	50
5	Measurement	53
5.1	Search of the Interferometer Sweet Spot	53
5.2	Adjustment of the RF-Flippers	59
5.3	Setting up the Detectors for Time-Dependent Measurements	61
5.4	Adjustment of the Energy Manipulator Coils	62
5.5	Phase Shifter Scans	67
6	Results	69
6.1	Data	71
6.2	Discussion	74
7	Conclusion and Outlook	77
	Bibliography	79

1 Introduction

The theory of quantum mechanics describes the world on the microscopic scale. Its validity has been confirmed experimentally time and time again, using various systems, e.g. photons, electrons, or neutrons [1]. Many results of quantum mechanics seem counter-intuitive, one of which is the wave-particle duality, whereby a massive particle, e.g. a neutron, behaves as a wave, which goes through the two paths of an interferometer at once and, after recombination, is detected as a particle through a nuclear reaction.

This behavior, at non relativistic speeds, is best described using the Schrödinger equation. Its solutions are waves that have the properties associated with a classical particle: energy, momentum and position. However, in contrast to classical mechanics, this description of a particle using the mathematical tool of a wavefunction is only probabilistic, not deterministic. The mathematics are precise in the sense that we can accurately calculate the probability to measure the particle at a specified location in space and time, but where it will manifest itself in the experiment is up to chance. This is called the collapse of the wavefunction, it is the transition from a description of many possible physical realizations to one single such manifestation upon measurement [2].

Yet the many possible realizations before the collapse are not without mutual influence. They show interference through the phase information the wavefunction carries [3][4]. A measurement of beam intensity only reveals the probabilities to register a particle count, given by the absolute square of the wavefunction – a real number. However, the phase information, i.e. the interplay of the real and complex valued parts of the wavefunction, can be accessed using so called weak measurements. These are weak intermediate interactions that influence the quantum system in a predictable way before detection, which do not lead to a collapse of the wavefunction. The weak value [5], which takes into account the preparation of the quantum system in an initial state (preselection), and also the measurement process (postselection), is a complex number characterizing the wavefunction, which directly appears in physical measurable quantities.

Interferometric phenomena – the superposition of waves – are a feature exhibited by many physical systems. In the case of neutrons as massive particles, in comparison with photons, there is no classical theory to explain the phenomenon of interference. For this reason neutron interferometry has long been established as an excellent tool to study the foundations of quantum mechanics [6].

An application of weak measurements and interferometry is the so called Cheshire Cat effect. Through a clever way of preparing the neutrons entering the interferometer and also choosing the quantum state, in which they are measured, i.e. the pre and postselection of the system, a counter-intuitive experimental situation arises [7]. A weak interaction involving the spin – the cat’s grin – will have a noticeable effect only on one path of the interferometer, whereas a measurement of the path will find the neutron’s path location – the cat’s body – to have taken the other way. Thereby these two properties, the spin and path degree of freedom, seem to be spatially separated. The name of the experiment is based on the Cheshire Cat in Lewis Caroll’s book *Alice in Wonderland* [8], where the cat is separated from its grin.

The first experimental observation of this effect was made in 2014 by Denkmayr et al. [7]. In the 2014 experiment, the measurements of spin and path were carried out consecutively for the two interferometer paths. The experiment conducted in the course of this master thesis seeks to make these four measurements simultaneously. This would confirm that the separation of the cat and its grin take place at the same time. For this purpose a new way of making a which-way measurement is implemented using the neutron’s energy degree of freedom. This is inspired by a similar method employed in [9] which uses small spin rotations that come with a shift in energy to mark the paths in an interferometer. However, the method of which-way marking using the energy degree of freedom implemented in this master thesis leaves the spin state unchanged. Inspiration for this method comes from multiphoton exchange processes observed in [10].

The two paths of the interferometer, one of which contains the grin and the other the body of the cat, are shifted in energy by different amounts, marking the different paths. When they recombine, together with a reference beam, an intensity oscillation with only one frequency corresponding to one path can be measured, when the neutrons are subject to pre and postselection. From this it is possible to say, on which path of the interferometer the cat’s body is located.

2 Cheshire Cat Emerging in Neutron Interferometry

This chapter gives a description of the quantum Cheshire Cat state and introduces both the neutron's spin and path degree of freedom as two-level quantum systems. It presents the weak value as a way of investigating the Cheshire Cat paradox.

The neutron, as a fundamental particle and building block of the material world, adheres to quantum mechanics and is associated with several properties, two of them being its magnetic characteristic – the spin – and its position in space [11]. A quantum Cheshire Cat experiment can realize a situation, where the two properties seem to be spatially separated on two opposite paths of a neutron interferometer (see fig. 2.1).

This, depending on interpretation, seemingly paradoxical situation was first proposed by Aharonov and Rohrlich in [12] and also Aharonov et al. in [13]. A first experimental confirmation using neutron interferometry was observed by Denkmayr et al. in 2014 [7], an equivalent experiment was carried out in 2015 [14] with a laser beam and in 2016 [15] using single photons. These experiments use a weak absorber in order to measure the path system, with the disadvantage, that its interaction with the quantum state is non-unitary and cannot be carried out simultaneously for both paths. The experiment conducted in the course of this diploma thesis takes a modified approach using neutrons and is an attempt to improve upon these shortcomings of the 2014 experiment.

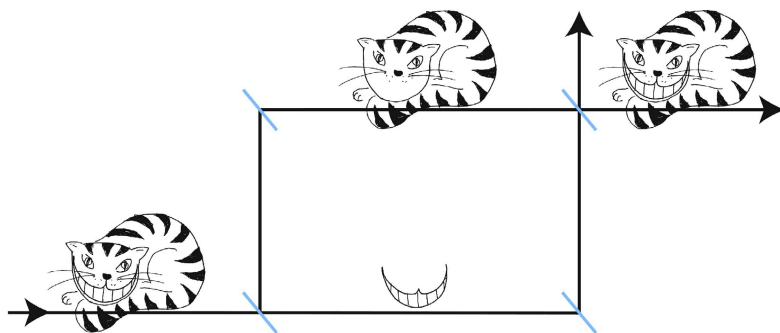


Figure 2.1: Artistic rendering of the quantum Cheshire Cat, body and grin take opposite paths in the interferometer. Picture taken from [7].

A necessary condition for the quantum Cheshire Cat experiment is the so called pre and postselection of the quantum state. The preselection prepares the system in an initial state, which then is subject to small localized influences on the two interferometer paths. These influences probe the system for the two properties mentioned above, the positions of the spin and path degree of freedom. Afterwards the quantum state is subject to postselection, i.e. adjusting the final state neutrons coming from the two paths need to have in order to reach the detector. When the quantum state is successfully pre and postselected a situation can arise, where a position measurement finds the spin on one arm, and the path degree of freedom on the other arm of the interferometer.

2.1 Measurement in Quantum Mechanics

Suppose a quantum state $|a_n\rangle$, which is a non-degenerate eigenstate of the Hermitian operator \hat{A} , then $|a_n\rangle$ is said to have the eigenvalue a_n corresponding to the observable \hat{A} .

$$\hat{A} |a_n\rangle = a_n |a_n\rangle \quad (2.1)$$

The eigenvalue corresponding to an observable must be a real number, whereas a general quantum state is represented by complex coefficients. Through the measurement of \hat{A} , a quantum state $|\psi\rangle$ turns out to be in one of the n eigenstates. Therefore, the state can be written in the basis of \hat{A} 's eigenstates.

$$|\psi\rangle = \sum_n c_{a_n} |a_n\rangle = \sum_n \langle a_n | \psi \rangle |a_n\rangle \quad (2.2)$$

Similarly, the observable can be expressed as the sum of the projection operators of the complete basis as

$$\hat{A} = \sum_n a_n |a_n\rangle \langle a_n|. \quad (2.3)$$

Before a measurement of \hat{A} on the state $|\psi\rangle$ is made, it is said to be represented by a superposition of many of its possible eigenstates, characterized by the coefficients c_{a_n} . After the measurement, of which the outcome was recorded, we found the quantum state in one of its eigenstates $|a_n\rangle$. The corresponding coefficient c_{a_n} has become equal to one and all the others are zero.

The probability to measure the eigenvalue a_n , when the quantum state on which the measurement is conducted is $|\psi\rangle$, is simply given by the absolute square of the corresponding coefficient c_{a_n} , i.e.

$$P(a_n) = c_{a_n}^* \cdot c_{a_n} = |\langle a_n | \psi \rangle|^2. \quad (2.4)$$

Lastly, the expectation value of \hat{A} is defined as

$$\langle \hat{A} \rangle = \sum_n a_n |\langle a_n | \psi \rangle|^2 = \langle \psi | \sum_n a_n |a_n\rangle \langle a_n | \psi \rangle = \langle \psi | \hat{A} | \psi \rangle, \quad (2.5)$$

and weights the possible eigenvalues a_n with their respective probabilities.

A practical example would be the passing of an arbitrarily polarized photon beam through an absorbing polarizer. Before the polarizer, the polarization state of the photon beam is in a (complex) superposition of its two mutually orthogonal eigenstates, namely $|H\rangle$ or $|V\rangle$. Suppose this arbitrary incident state is given by $|\psi_i\rangle = \frac{1}{\sqrt{2}}(|H\rangle + |V\rangle)$, i.e. the beam is polarized at an angle of 45° between the horizontal and vertical polarization direction. When the polarizer is set to the vertical direction, then the probability for a photon with polarization $|\psi_i\rangle$ to go through the polarizer is simply given by $P(V) = |\langle V | \psi_i \rangle|^2 = \frac{1}{2}$. Afterwards the quantum state is just found in $|\psi_f\rangle = \frac{1}{\sqrt{2}}|V\rangle$, the factor $\frac{1}{\sqrt{2}}$ represents the fact, that half of the photons make it through the polarizer and the other half is absorbed. The type of measurement described here is called a strong or projective measurement, since the state after the measurement is given by the projection of $|\psi_i\rangle$ onto the state of vertical polarization $|\psi_f\rangle = \hat{\Pi}_V |\psi_i\rangle = |V\rangle \langle V | \psi_i \rangle$, with the projection operator defined as $\hat{\Pi}_V = |V\rangle \langle V|$.

2.1.1 Weak Measurements

In a more formal way of treating the measurement process described above, the measurement device itself is treated as a quantum system. The whole system can be written as a product $|\Psi\rangle = |\psi\rangle |\Phi\rangle$ consisting of the measurement device $|\Phi\rangle$ (also called ancilla or pointer state) and the quantum state $|\psi\rangle$ under study. The product states interact via a Hamiltonian of the form [2]

$$\mathcal{H}_{int} = -g(t)\hat{q}\hat{A}, \quad (2.6)$$

where $g(t)$ is a function whose time integral over the interaction time is unity, \hat{q} is a canonical position variable of the measuring device, of which \hat{p} is the conjugate momentum, and \hat{A} is the observable to be measured. The difference of $p_f - p_i$ of the momentum operator \hat{p} corresponding to the measuring device before and after the measurement has taken place is called the pointer reading and encodes the value of \hat{A} .

A realistic treatment of the measuring device assumes it to have an initial state

$$|\Phi_i\rangle = \int dp e^{-\Delta^2 p^2} |p\rangle = \int dq e^{-q^2/(2\Delta)^2} |q\rangle, \quad (2.7)$$

which is a Gaussian centered around $p = 0$ with an initial spread of $\Delta q = \Delta$ and

$\Delta p = \frac{1}{2\Delta}$ in position, respectively momentum space (here $\hbar = 1$). The q and p space representations are obtained via mutual Fourier transformations. After the interaction via \mathcal{H}_{int} the whole system has evolved into [16]

$$\begin{aligned} |\Psi'\rangle &= e^{-i \int \mathcal{H}_{int} dt} |\Psi_i\rangle = e^{i \hat{q} \hat{A}} |\psi_i\rangle |\Phi_i\rangle \\ &= \sum_n c_{a_n} \int dq e^{iq a_n} e^{-q^2/(2\Delta)^2} |a_n\rangle |q\rangle \\ &= \sum_n c_{a_n} \int dp e^{-\Delta^2(p-a_n)^2} |a_n\rangle |p\rangle, \end{aligned} \quad (2.8)$$

expanding the state $|\psi\rangle$ in the basis of the observable \hat{A} 's eigenstates.

Now two cases can be distinguished, the first having a small initial spread of Δp , which makes Δ very large compared to the spacing between the a_n 's. Then the sum in eq. (2.8) consists of n distinct sharp Gaussian peaks, each centered around a possible value of a_n . This corresponds to a strong measurement as described in the preceding section.

The other case has a large initial Δp , which gives a sum of n broad Gaussians, appearing similar to one large Gaussian distribution, whose center is now shifted to the mean value of \hat{A} . This situation is called a weak measurement and does not give any considerable information when it is performed once. However, by repeating the measurement many times, the momentum shift, and therefore the mean value of \hat{A} , can be determined up to any required precision .

2.2 Weak Values

The weak value, first introduced by Aharonov, Albert and Vaidman [5], is a measure of an observable \hat{A} conditioned on pre and postselection, which is defined as

$$\langle \hat{A} \rangle_w = \frac{\langle \psi_f | \hat{A} | \psi_i \rangle}{\langle \psi_f | \psi_i \rangle}. \quad (2.9)$$

In this equation $|\psi_i\rangle$ is the initial preselected and $|\psi_f\rangle$ the postselected final state.

When the measurement scheme from the previous section is extended by a projective measurement of state $|\psi\rangle$, by choosing the final state $|\psi_f\rangle = \sum_n c'_{a_n} |a_n\rangle$ the quantum system must have, in order to be able to reach the detector, an interesting

phenomenon occurs.

$$\begin{aligned}
|\Phi_f\rangle &= \langle\psi_f|\Psi'\rangle = \langle\psi_f|e^{i\hat{q}\hat{A}}|\psi_i\rangle|\Phi_i\rangle \\
&\approx \langle\psi_f|(1+i\hat{q}\hat{A}+\dots)|\psi_i\rangle|\Phi_i\rangle \\
&= \langle\psi_f|\psi_i\rangle(1+i\hat{q}\langle\hat{A}\rangle_w+\dots)|\Phi_i\rangle \\
&\approx \langle\psi_f|\psi_i\rangle \int dq e^{iq\langle\hat{A}\rangle_w} e^{-q^2/(2\Delta)^2}|q\rangle \\
&= \langle\psi_f|\psi_i\rangle \int dp e^{-\Delta^2(p-\langle\hat{A}\rangle_w)^2}|p\rangle
\end{aligned} \tag{2.10}$$

Now the momentum distribution of the pointer state $|\Phi_f\rangle$ is shifted away from the center by an amount equal to the weak value $\langle\hat{A}\rangle_w$. This suggests a possibility to access weak values in practical situations.

The weak value has a number of interesting properties [17]:

- Weak values are complex quantities that characterize relative corrections to detection probabilities caused by an intermediate interaction.
- When the pre and postselected states are nearly orthogonal the weak value becomes large, because the denominator of eq. (2.9) goes to zero. This can be used in order to amplify certain signals corresponding to unknown experimental parameters above technical noise backgrounds.
- It can be used in order to completely characterize a quantum state up to a global phase, a technique also termed direct quantum state tomography. Direct in this context signifies that no complicated computational data processing is needed and the desired information appears linearly in measurable quantities, e.g. beam intensity.
- The real part of $\langle\hat{A}\rangle_w$ can be interpreted as a conditioned average of the observable \hat{A} on the condition of pre and postselection.
- The weak value is generally a complex number, whose imaginary part causes a position shift in the pointer state (center of the Gaussian is shifted in the fourth line of eq. (2.10) in q representation) and whose real part causes a momentum shift of the pointer (last line of eq. (2.10)).
- The weak value can be used in order to investigate quantum paradoxes.
- Critics of the weak value do not ascribe physical realism to it and treat it as just a mathematical result of quantum measurement theory.

It should be noted that weak values cannot be extracted from a single particle measurement, but are obtained as averages over many detected particles. They are called weak because originally the theory of weak values was formulated as such, that the measurement of the observable \hat{A} only perturbs the wavefunction lightly, meaning the interaction is only appreciable in the first order.

2.3 Experimental Studies of Weak Measurements/Weak Values

In this section two examples of experiments using weak values are presented. The first experiment uses the weak value in order to directly measure a quantum state, the second is an application of the weak value as a tool for amplification.

2.3.1 Direct Measurement of the Quantum Wavefunction

An example of the use of weak values to directly determine the wavefunction of a quantum state is the experiment performed by Lundeen et al. in 2011 [18]. The wavefunction that was directly measured is the transverse spatial wavefunction of a photon beam $\Psi(x)$. The experimental setup is depicted in fig. 2.2.

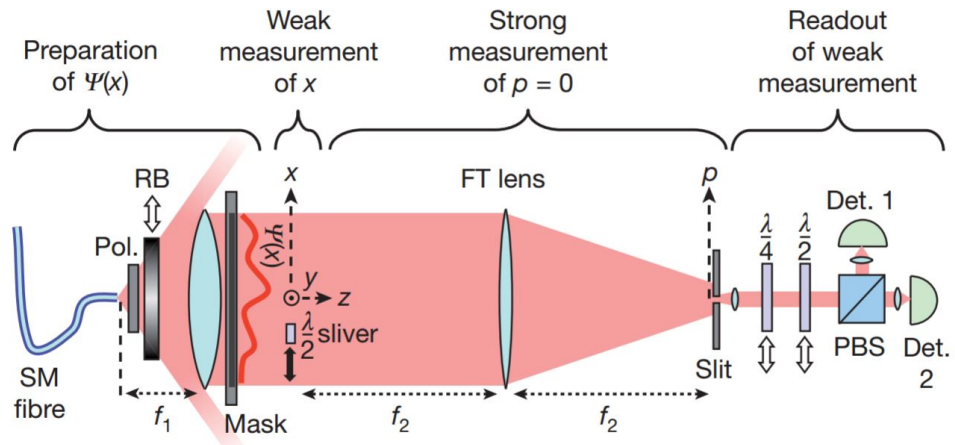


Figure 2.2: Depiction of the setup of the experiment by Lundeen et al. taken from [18].

A single mode optical fiber transmits photons with a definite wavelength to be used for the experiment which first pass through a polarizer. The beam profile, which originally is of Gaussian form, can be modified with a special attenuator

labeled RB. The preparation of the photon beam up to this point constitutes the preselection. The weak measurement scheme uses the polarization state of the photons as a pointer system. The polarization is weakly rotated by a small angle α using a $\lambda/2$ -plate that can be slid across the transverse direction x of the beam. Afterwards a Fourier transform lens selects only photons with a transverse momentum p to be able to reach the detectors, which is the postselection. The weak value of the projection operator $\hat{\Pi}_x = |x\rangle\langle x|$ is then given by

$$\langle \hat{\Pi}_x \rangle_w = \frac{\langle p|x\rangle\langle x|\Psi \rangle}{\langle p|\Psi \rangle} = \frac{e^{ipx/\hbar}\Psi(x)}{\Phi(p)}. \quad (2.11)$$

When the postselected momentum $p = 0$, this weak value is directly proportional to the transverse spatial wavefunction of the beam $\langle \hat{\Pi}_x \rangle_w \propto \Psi(x)$.

As stated in the preceding section, the real and imaginary part of the weak value are connected to shifts in q and p of the pointer state (not to be confused with x and p of the transverse beam profile Ψ). The role of position q and conjugate momentum p as complementary bases in the case of photon polarization as a pointer state is played by the linear and circular polarization bases. In order to map out the real and imaginary part of $\langle \hat{\Pi}_x \rangle_w$ and therefore the wavefunction, the polarization in these complementary bases has to be measured for different transverse beam positions x . For this, a combination of either a $\lambda/4$ or $\lambda/2$ -plate, together with a polarization dependent beam splitter and two detectors is used. With the $\lambda/2$ -plate the linear polarization is measured and therefore $\text{Re}\Psi(x)$. For $\text{Im}\Psi(x)$ the $\lambda/4$ -plate is used to measure the circular polarization. The polarization dependent beam splitter transmits photons corresponding to orthogonal basis states into two different detectors for an intensity measurement. The difference of the detector counts for the two complementary bases can then be used to directly determine $\Psi(x)$.

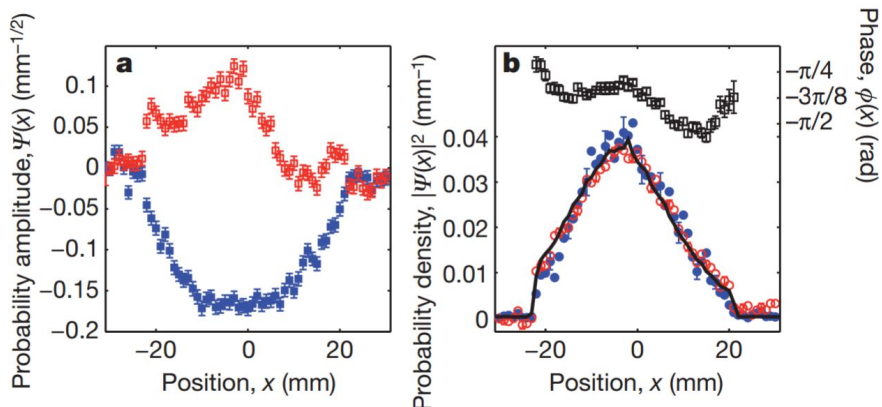


Figure 2.3: Measurement of $\Psi(x)$ taken from [18]. Left: $\text{Re}\Psi(x)$ in blue, $\text{Im}\Psi(x)$ in red. Right: Comparison with a strong measurement of transverse beam intensity (solid line) and phase plot.

The measurement results depicted in fig. 2.3 shows the direct reconstruction, i.e. the real and complex part of the transverse spatial wavefunction $\Psi(x)$. It shows good agreement with a strong measurement of the beam intensity along the transverse direction x .

2.3.2 Ultrasensitive Beam Deflection Measurement via Interferometric Weak Value Amplification

Another application of the weak value is to use it in order to amplify small changes of the system under study onto a large change of the pointer readout. In 2009 Dixon et al. used it in order to interferometrically measure very small beam deflections [19]. Their experimental setup is depicted in fig. 2.4.

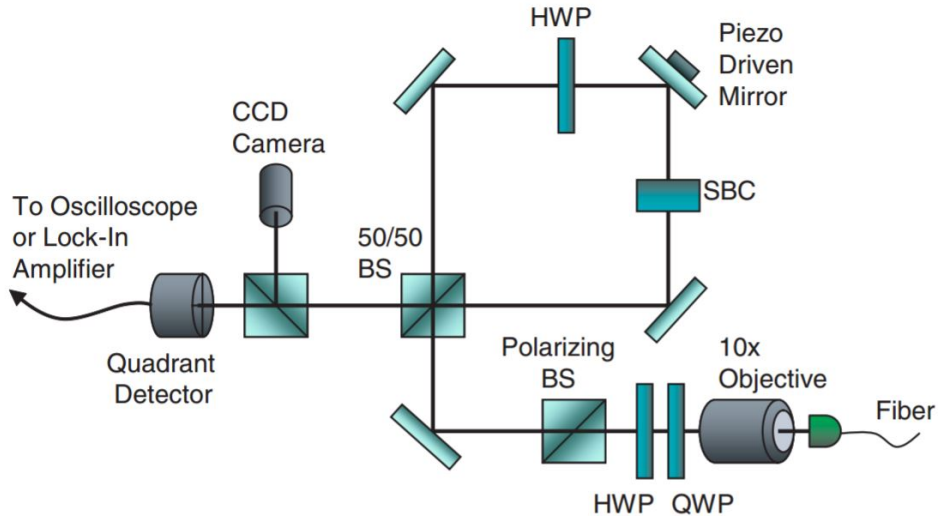


Figure 2.4: Depiction of the experimental setup of [19].

The preselected state of the system is given by

$$|\psi_i\rangle = |\Phi_i\rangle |X\rangle = \frac{1}{\sqrt{2}}(ie^{i\chi} |\circlearrowleft\rangle + |\circlearrowright\rangle) |X\rangle, \quad (2.12)$$

where the states $|\circlearrowleft\rangle$ and $|\circlearrowright\rangle$ are the two possible paths a polarized photon can take through the Sagnac interferometer, namely clockwise or counterclockwise, and $|X\rangle$ is the transverse position of the beam. A tunable phase shift χ between the two states is introduced. The weak measurement of beam deflection is produced by a slight tilt of the piezo driven mirror. This effects the beam via an impulsive interaction Hamiltonian leading to a time evolution of the form

$$\exp(-ix\hat{\mathbf{A}}k), \quad (2.13)$$

where x is the transverse beam position, k is the transverse momentum change caused by the mirror tilt, and $\hat{\mathbf{A}} = |\circlearrowleft\rangle\langle\circlearrowleft| - |\circlearrowright\rangle\langle\circlearrowright|$ accounts for the fact, that this effect comes with an opposite sign for the different interferometer states. The state after this interaction is given by

$$|\psi'\rangle = e^{-ix\hat{\mathbf{A}}k} |\psi_i\rangle \approx (1 - ix\hat{\mathbf{A}}k) |\Phi_i\rangle |X\rangle, \quad (2.14)$$

when the mirror tilt is smaller then the width of the beam profile. After this interaction, the state $|\psi'\rangle$ is projected onto the postselected state of the interferometer, which is given by

$$|\Phi_f\rangle = \frac{1}{\sqrt{2}} (|\circlearrowleft\rangle + i|\circlearrowright\rangle). \quad (2.15)$$

The resulting state after the postselection is given by

$$\begin{aligned} \langle\Phi_f|\psi'\rangle &= \langle\Phi_f| (1 - ix\hat{\mathbf{A}}k) |\Phi_i\rangle |X\rangle \\ &= (\langle\Phi_f|\Phi_i\rangle - ikx \frac{\langle\Phi_f|\hat{\mathbf{A}}|\Phi_i\rangle}{\langle\Phi_f|\Phi_i\rangle}) |X\rangle \\ &\equiv \langle\Phi_f|\Phi_i\rangle (1 - ikx\langle\hat{\mathbf{A}}\rangle_w) |X\rangle \\ &\approx \langle\Phi_f|\Phi_i\rangle e^{-ikx\langle\hat{\mathbf{A}}\rangle_w} |X\rangle. \end{aligned} \quad (2.16)$$

The result consists of the overlap between $\langle\Phi_f|\Phi_i\rangle = \sin(\chi/2)$ which can be tuned with the phase shift χ , and the transverse beam profile $|X\rangle$, which is altered by a momentum shift equal to $k\langle\hat{\mathbf{A}}\rangle_w$. The momentum shift is amplified by the weak value which in this case amounts to $\langle\hat{\mathbf{A}}\rangle_w = i \cot(\chi/2) \approx -2i/\chi$ and can become quite large for small χ . This shift in momentum leads to a displacement of the beams intensity profile at the detectors and can be used to measure changes in the signal caused by very small tilts of the mirror up to 400 ± 200 frad (see fig. 2.5).

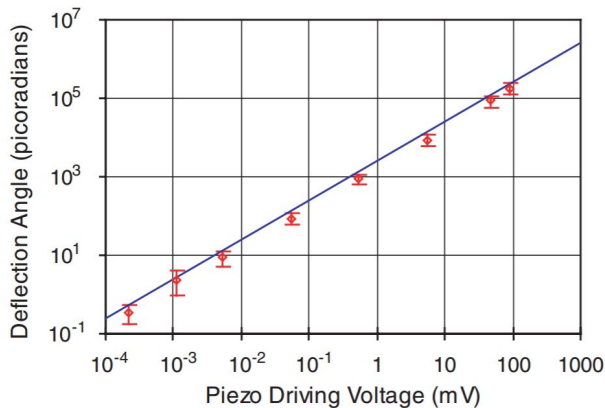


Figure 2.5: Measurement of very small angle mirror tilts by Dixon et al. [19].

2.4 Neutron Optical Approach

In his doctoral thesis of 1924 Louis de Broglie postulated the wave nature of massive particles, ascribing a wavelength of $\lambda = h/p$ to them. In 1927 Davisson and Germer gave prove of this postulate for electrons by scattering them from nickel crystals, demonstrating the Bragg law to be valid also in the case of massive particles. In the 1960s Bonse and Rauch utilized perfect silicon crystals, previously used for x-ray scattering, to measure interference for neutrons. The field of neutron interferometry has opened up a new way of investigating quantum phenomena, since the macroscopically separated wave packets inside the interferometer allow for the insertion of several optical elements in one or both beams.

2.4.1 Neutron Interferometry

As a quantum particle, the neutron is described using a wavefunction. It is a function of the neutron's momentum and its position in time and space and follows the Schrödinger equation. If one takes the absolute square of the wavefunction one gets the probability to find the particle at the specified coordinates. The best way to observe the interference effect of neutrons is to use a perfect crystal interferometer. A more thorough treatment of the working principle of a neutron interferometer is given later on. At this point only a brief overview is presented.

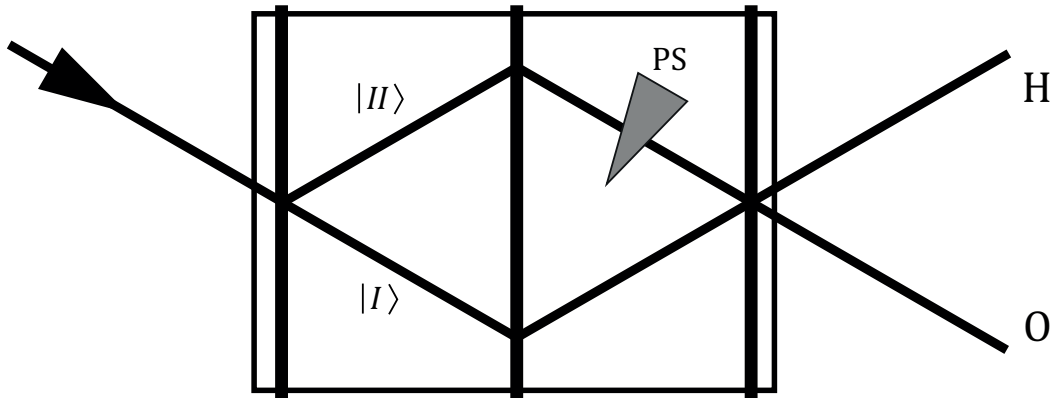


Figure 2.6: Schematic depiction of a three plate neutron interferometer with a phase shifter in path II.

A schematic depiction of a three plate neutron interferometer is given in fig. 2.6. In essence a neutron interferometer consists of a beam splitter that splits the incident wavefunction in two parts of equal amplitude (first interferometer plate). These two parts propagate along two different paths, on which each beam is reflected off a mirror (second plate). The two beams are subsequently recombined at the third plate and leave the interferometer in two distinct beams, the O beam in parallel to the incident neutron beam, and the reflected H beam. This interferometric setup is referred to as the Mach-Zehnder type. The interferometer is cut from a monolithic perfect silicon crystal. The neutrons entering the interferometer are monochromatized beforehand and all have the velocity $v \sim 2$ km/s. With typical count rates of 10 – 100 counts/s at the O detector, the chances of two neutrons being inside the interferometer at the same time are negligibly small. Therefore all interferometric phenomena observed are of type self-interference. Suppose the incident wavefunction is given by Ψ_0 , then the intensity of the O beam can be written as

$$\begin{aligned} I_O(\Delta\chi) &= |\Psi_I + \Psi_{II}|^2 = \frac{1}{2}|\Psi_0|^2|1 + e^{i\Delta\chi}|^2 \\ &= \frac{1}{2}(1 + \cos \Delta\chi), \end{aligned} \quad (2.17)$$

with a phase difference of $\Delta\chi$ between the two beams introduced by the phase shifter labeled PS in fig. 2.6. As can be seen from the last line in eq. (2.17), the intensity of the O beam oscillates with $\Delta\chi$. The law of particle conservation forbids that neutrons cease to exist midway through the interferometer and therefore, when I_O decreases due to changes in $\Delta\chi$, the intensity of the H beam goes up by the same amount. In summary one can say, that the neutron inside the interferometer exists as a superposition of two states, namely the two possible paths.

2.4.2 Neutron Spin: A Two-Level Quantum System

As its name suggests, the neutron carries no net electrical charge, however it has a magnetic moment: it is a spin- $\frac{1}{2}$ -particle. The spin of a neutron is, as is the path degree of freedom in a three plate interferometer, a two-level system. This means, that upon a definite measurement of the spin, one can only have two possible results, either the spin was in state $|\uparrow_z\rangle$ or $|\downarrow_z\rangle$. The spin direction is always given with respect to an axis, conventionally the z-axis, and can either be parallel or antiparallel to it. However, since the spin of a particle is a quantum property, every possible superposition between the two spin states can exist. Through this mathematical mechanism it is possible for the spin state to describe the orientation of the magnetic moment, a vector in three dimensional space. Suppose an arbitrary spin state given by

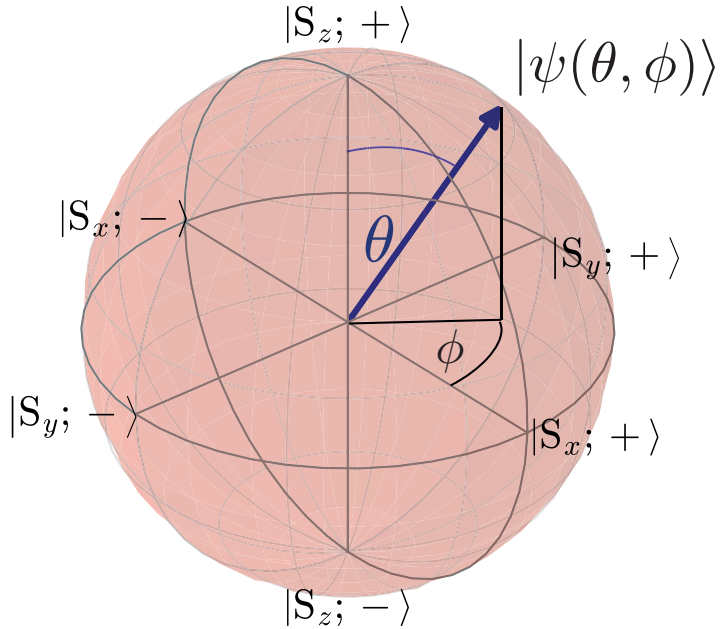


Figure 2.7: Visualization of an arbitrary spin state on the Bloch sphere.

$$|\psi(\theta, \phi)\rangle = \cos\left(\frac{\theta}{2}\right) |\uparrow_z\rangle + \sin\left(\frac{\theta}{2}\right) e^{i\phi} |\downarrow_z\rangle \quad (2.18)$$

then the vector of the magnetic moment is related to the spin by the equation

$$\vec{\mu} = \gamma \frac{\hbar}{2} \langle \psi | \vec{\sigma} | \psi \rangle, \quad (2.19)$$

where γ is the gyromagnetic ratio of the neutron ($\gamma = |2\mu/\hbar| = 1,83247172(43) \times 10^8 \text{ s}^{-1}\text{T}^{-1}$) and $\vec{\sigma}$ is the vector of spin matrices, which are

$$\sigma_x = \begin{pmatrix} 0 & 1 \\ 1 & 0 \end{pmatrix}, \quad \sigma_y = \begin{pmatrix} 0 & -i \\ i & 0 \end{pmatrix}, \quad \sigma_z = \begin{pmatrix} 1 & 0 \\ 0 & -1 \end{pmatrix}, \quad (2.20)$$

with

$$|\uparrow_z\rangle \equiv \begin{pmatrix} 1 \\ 0 \end{pmatrix} \quad \text{and} \quad |\downarrow_z\rangle \equiv \begin{pmatrix} 0 \\ 1 \end{pmatrix}.$$

An arbitrary spin state is a point located anywhere on the so called Bloch sphere specified by the polar angle ϕ and the azimuthal angle θ . The path degree of freedom is, as stated above, also a two-level quantum system and can therefore be treated mathematically in an equivalent way to the spin.

2.4.3 Manipulation of the Spin: Spin-Rotation

As stated in the preceding section, a spin- $\frac{1}{2}$ state can be represented by the two basis states $|\uparrow_z\rangle$ or $|\downarrow_z\rangle$ – parallel or anti-parallel with respect to a quantization axis, conventionally the z-axis. When the spin is located inside an external magnetic field $\vec{B} = (0, 0, B_z)^T$, the two basis states correspond to different (potential) energy levels $E = \pm\mu \cdot B_z$, with the lower energy for parallel orientation. When the spin is initially in one of these two states and the direction of this magnetic field changes, provided the rate of change is slow compared to $|\gamma B|$, i.e. the change is adiabatic, it will remain in its initial state, now with respect to the new direction of the external field. This situation is depicted in fig. 2.8.

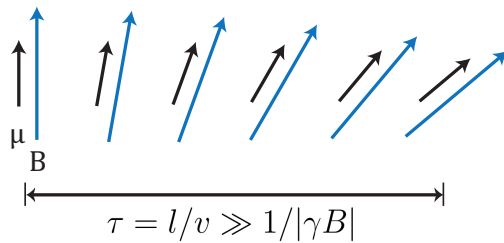


Figure 2.8: Spin following an adiabatically changing external field (blue arrow).

When the initial spin state is not purely $|\uparrow_z\rangle$ or $|\downarrow_z\rangle$, but a superposition of the two, the difference in potential energy of these two states leads to a change of the polarization vector $\vec{P} = \langle \Psi | \vec{\sigma} | \Psi \rangle$ in time. This phenomenon is called Larmor precession. When a spin is inside a region with a constant magnetic field, the polarization vector rotates around an axis parallel to the field, keeping the same inclination between magnetic moment and external field. The vector \vec{P} precesses around the magnetic field \vec{B} with the Larmor frequency $\omega_L = |\gamma B|$.

$$\frac{d}{dt} \vec{P} = \vec{P} \times \gamma \vec{B} \quad (2.21)$$

To control the spinor rotation in the experiment, a magnetic field can be applied only in a limited region of space. Also the field transition needs to be abruptly, so that the spin does not adiabatically follow the external field.

There are two ways to make controlled spinor rotations, one is to have direct-current spin turners. They work by having a constant magnetic field, around which the spin rotates, contained inside a coil (see fig. 2.9). The spin-rotation angle is proportional to the field-strength inside the coil and the time of flight through it. This method comes with the disadvantage of having material (wires) in the neutron beam, which reduces coherence of the interfering beams due to scattering, when it occurs inside the interferometer.

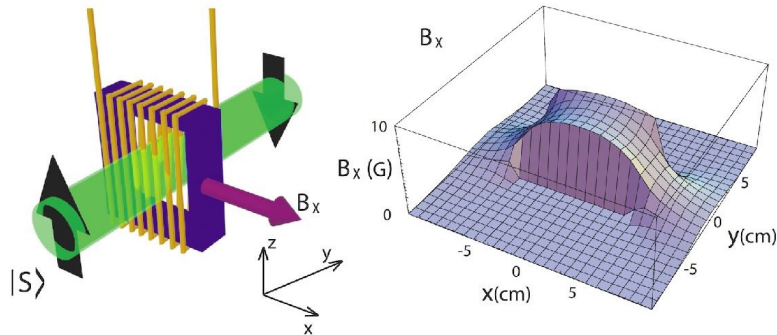


Figure 2.9: Left: Depiction of a direct-current spin-flipper doing a π -spin-rotation. Right: Simulation of the magnetic field produced by the spin-flipper. It has a non adiabatic change along the y -axis.

Another way of doing controlled spinor rotations is to use so called resonant-frequency spin-flippers. They ensure the non-adiabaticity of the field change by having the magnetic field oscillate in time. Their working principle is explained in more detail later on.

2.5 Spin and Path Weak Values and the Quantum Cheshire Cat in Neutron Optical Experiments

In the main experiment of this work the preselected state is given by

$$|\psi_i\rangle = \frac{1}{\sqrt{2}} |\uparrow_z\rangle (|I\rangle + |II\rangle), \quad (2.22)$$

which is an entangled state characterized by the direct product of the spin and path state. When a polarized spin- $|\uparrow_z\rangle$ neutron enters the interferometer its wavefunction is split 50 : 50 between the two paths $|I\rangle$ and $|II\rangle$. Before recombination of the two beams a π -spin-flip takes place in one arm of the interferometer. On its way to the detector the neutron beam passes through a spin analyzer that filters out all spin- $|\downarrow_z\rangle$ neutrons. The postselected state reads

$$|\psi_f\rangle = \frac{1}{\sqrt{2}} (|\downarrow_z\rangle |I\rangle + |\uparrow_z\rangle |II\rangle). \quad (2.23)$$

When one now takes a look at the weak values for the path projection operators defined as

$$\hat{\Pi}_I = |I\rangle\langle I| \quad \text{and} \quad \hat{\Pi}_{II} = |II\rangle\langle II|, \quad (2.24)$$

and the operators for spin rotation on a single path around an axis in the x-y-plane defined as

$$\hat{\sigma}_\xi \hat{\Pi}_I = \hat{\sigma}_\xi |I\rangle\langle I| \quad \text{and} \quad \hat{\sigma}_\xi \hat{\Pi}_{II} = \hat{\sigma}_\xi |II\rangle\langle II|, \quad (2.25)$$

with $\hat{\sigma}_\xi = \hat{\sigma}_x \cos \xi + \hat{\sigma}_y \sin \xi$, one finds

$$\langle \hat{\Pi}_I \rangle_w = 0 \quad \text{and} \quad \langle \hat{\Pi}_{II} \rangle_w = 1, \quad (2.26)$$

as well as

$$\langle \hat{\sigma}_\xi \hat{\Pi}_I \rangle_w = e^{i\xi} \quad \text{and} \quad \langle \hat{\sigma}_\xi \hat{\Pi}_{II} \rangle_w = 0. \quad (2.27)$$

The last two relations result from the fact, that $\hat{\sigma}_\xi |\uparrow_z\rangle = a |\downarrow_z\rangle$, up to a constant phase factor a , and vice versa $\hat{\sigma}_\xi |\downarrow_z\rangle = a |\uparrow_z\rangle$. With the given pre and postselected states, the weak values suggest the neutron takes path II and its spin path I.

A measurement of the weak value $\langle \hat{\sigma}_\xi \hat{\Pi}_j \rangle_w$ can be realized by having a magnetic field pointing somewhere in the x-y-plane specified by angle ξ locally interact with the neutron spin on path j . The path weak value $\langle \hat{\Pi}_j \rangle_w$ can be measured by having another interaction, that does leave the spin state unchanged, localized on path j . The strength of these interactions should be weak enough in order to avoid perturbations of the quantum state that lie outside the regime of weak measurements.

2.6 Other Experimental and Further Theoretical Studies of the Quantum Cheshire Cat Effect

The first analysis and proposal of a quantum Cheshire Cat experiment is given in [13]. As is necessary for the Cheshire Cat effect, orthogonal spin states are pre or postselected on the two arms of an interferometer. In the proposed experiment the role of the neutron spin as described above is played by the photon's polarization state.

As is argued in [20], in this experiment the pointer state needed to read out the result of the weak measurements of either polarization or path information is the transverse spatial wavefunction of a laser beam at the detector. The weak measurement of the polarization state is conducted by placing a birefringent crystal, that displaces only photons of one polarization state to the left or right, in one

arm. The path state is weakly measured by placing a glass plate, that displaces the beam independent of polarization in a direction up or down. These displacements need to be very small compared to the size of the beam profile in order to be considered a weak measurement. Analogous to the weak values given in the preceding section the measurements of path and polarization produce a change in the pointer state only on one arm of the interferometer and are effective on opposite sides.

The actually realized Cheshire Cat experiments using photons by Atherton et al. [14] and single heralded photons by Ashby et al. [15] replaced the beam displacing glass plate with a weak absorber. The polarization dependent beam displacement of the birefringent crystal is replaced with a slight polarization rotation using a half-wave plate. Therefore these experiments are exactly analogous to the one by Denkmayr et al. using neutrons [7], which is explained in more detail at the beginning of the following chapter. The authors of [14] give an explanation using the classical expressions for the electric field of the laser beam. Their experiment is not in the quantum regime and therefore the interfering photons can actually take both possible paths at once. Together with Corrêa et al. [20], the authors of [14], express the view, that the experimental situation only seems paradoxical, when a kind of physical realism is ascribed to the wavefunction between pre and postselection. They state, that the experimental outcome can also be understood from the principle of interference and refute the claim, that the spin/polarization and path degrees of freedom are actually separated from each other.

In a thorough theoretical treatment of the quantum Cheshire Cat experiments and the criticism they sparked, Duprey et al. [21] state, that the experiments [7][14][15] are not real implementations of the Cheshire Cat phenomenon, since the spin/polarization and path degree of freedom of the neutron/photon in the interferometer would need to be expanded by a third degree of freedom, an actual pointer state. They claim, that the intensity measurement at the detector is not a suitable pointer readout. An actual implementation of the Cheshire Cat experiment would indeed impact the pointer state as if the weak coupling of the interaction Hamiltonian involving the spin is only effective on one path and the coupling involving the path projector is effective on the other, when pre and post-selected states are suitably chosen. This is true, because the transition amplitude of the preselected to the postselected state corresponding to a weak interaction, with a weak value of zero, is also zero and the transition is therefore forbidden. According to Duprey et al., an actual Cheshire Cat experiment has not been observed experimentally.

3 Theory

This chapter describes the protocol for measurements of spin and path localization in order to observe the Cheshire Cat paradox. An explanation of the experimental method of spin rotation is presented together with a technique, that reveals which path in the interferometer a neutron takes by using the neutron's energy degree of freedom as a path marker. In the end a theoretical description of the experiment, which was conducted in the course of this master thesis at the Institut Laue-Langevin in Grenoble, is given.

3.1 Scheme of the Previous Quantum Cheshire Cat Experiment

The quantum 2014 Cheshire Cat experiment, the first experimental observation of the effect using matter-wave interferometry, was also carried out at the Institute Laue-Langevin in Grenoble. The experimental setup at that time is depicted in fig. 3.1. Incoming polarized $|\uparrow_z\rangle$ neutrons are rotated by an angle of $\pi/2$ into the x-y-plane by the direct-current spin-rotator DC1 before entering the interferometer. Between the first and the second plate of the interferometer the preselected state is prepared by two so called Larmor accelerators, which consist of Helmholtz coils that produce magnetic fields in the z-direction. These fields locally weaken or strengthen the z-field produced by the guide field coils surrounding the experimental region. This in turn leads to different spin directions for the paths upon exit of the two accelerator coils, when the Larmor frequency is shifted locally. This effect can be tuned in order to produce the preselected state

$$|\psi_i\rangle = \frac{1}{\sqrt{2}}(|\uparrow_x\rangle|I\rangle + |\downarrow_x\rangle|II\rangle). \quad (3.1)$$

The combination of DC2 and supermirror analyzer permits only $|\downarrow_x\rangle$ -neutrons to enter the O detector, therefore the postselected state is given by

$$|\psi_f\rangle = \frac{1}{\sqrt{2}}|\downarrow_x\rangle(|I\rangle + |II\rangle). \quad (3.2)$$

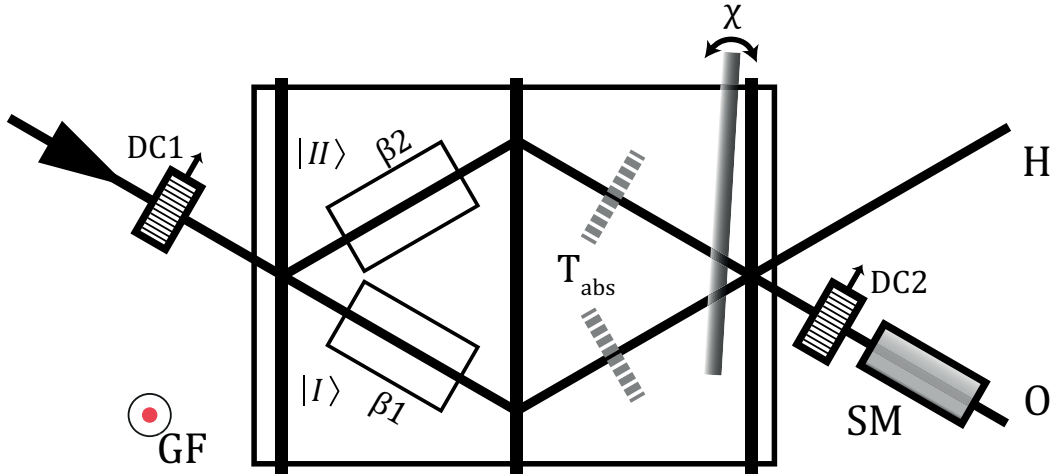


Figure 3.1: Schematic depiction of the 2014 Cheshire Cat experiment. Larmor accelerators between first and second interferometer plate depicted as rectangles. Dashed gray lines signify where the weak absorbers are placed one after the other.

The position measurement of the spin on both paths of the interferometer is now performed by introducing small perturbations, additional spin rotation angles around the z-axis, denoted by β_I and β_{II} . These perturbations are deviations from the z-field of the Larmor accelerators used for the preselection.

The effect of the modified magnetic field onto the neutron wavefunction ψ is calculated from the formula $\psi' = e^{-\frac{i}{\hbar} \int \mathcal{H}_{int} dt} \psi$, with the interaction Hamiltonian $\mathcal{H}_{int} = -\gamma \frac{\hbar}{2} \vec{\sigma} \cdot \vec{B}$ active inside the region of the Larmor accelerators. Rotation angles β_j are therefore proportional to the magnetic field strength produced by the Larmor accelerators and the time of flight through their active region. The big guide field has the same influence in both paths and therefore does not lead to a relative spin rotation. When the wavefunction after the first interferometer plate is given by $|\psi_i\rangle$, the weakly perturbed state right before the middle plate reads

$$\begin{aligned}
 |\Psi'\rangle &= \left(e^{+ix/2} e^{i\beta_I \hat{\sigma}_z} \hat{\Pi}_I + e^{-ix/2} e^{i\beta_{II} \hat{\sigma}_z} \hat{\Pi}_{II} \right) |\psi_i\rangle \\
 &\approx \left(e^{+ix/2} [1 + i\beta_I \hat{\sigma}_z] \hat{\Pi}_I + e^{-ix/2} [1 + i\beta_{II} \hat{\sigma}_z] \hat{\Pi}_{II} \right) \frac{1}{\sqrt{2}} (|\uparrow_x\rangle |I\rangle + |\downarrow_x\rangle |II\rangle) \\
 &= \frac{1}{\sqrt{2}} \left(e^{+ix/2} [1 + i\beta_I \hat{\sigma}_z] |\uparrow_x\rangle |I\rangle + e^{-ix/2} [1 + i\beta_{II} \hat{\sigma}_z] |\downarrow_x\rangle |II\rangle \right) \\
 &= \frac{1}{\sqrt{2}} \left(e^{+ix/2} [|\uparrow_x\rangle + \beta_I |\downarrow_x\rangle] |I\rangle + e^{-ix/2} [|\downarrow_x\rangle + i\beta_{II} |\uparrow_x\rangle] |II\rangle \right)
 \end{aligned} \tag{3.3}$$

with the action of the phase shifter, i.e. a factor $e^{\pm i\chi/2}$ with the sign depending on the path, and using the result $\hat{\sigma}_z |\uparrow_x\rangle = |\downarrow_x\rangle$ and $\hat{\sigma}_z |\downarrow_x\rangle = |\uparrow_x\rangle$. After the third interferometer plate, the beams I and II are recombined and pass through DC2 and the supermirror analyzer, which in combination only transmit the $|\downarrow_x\rangle$ -spin component. This corresponds to the postselection of state $|\psi_f\rangle$. The wavefunction after the analyzer is then given by

$$|\Psi''\rangle = \frac{1}{\sqrt{2}}(e^{-i\chi/2}|II\rangle + i\beta_I e^{+i\chi/2}|I\rangle)|\downarrow_x\rangle. \quad (3.4)$$

Calculating the intensity by taking the absolute square up to first order in β results in

$$I_O = |\langle\Psi''|\Psi''\rangle|^2 = \frac{1}{2} - 2\beta_I \sin \chi. \quad (3.5)$$

From the O beam intensity one can tell, that only the influence of β_I survives the postselection. In this sense the spin property takes path I. In principle both measurements of β_j can be carried out simultaneously. Then, when one of the two effects is switched off, one after the other, only one of them will have an appreciable effect onto the O beam intensity, when the disturbances are sufficiently small. This result can be interpreted using the weak values for the spin localization

$$\langle \hat{\sigma}_z \hat{\Pi}_I \rangle_w = 1 \quad \text{and} \quad \langle \hat{\sigma}_z \hat{\Pi}_{II} \rangle_w = 0.$$

The situation is different for the path measurement. This measurement was done by placing a weak absorber with a transmittance of $T_{abs} \approx 80\%$ in one of the interferometer paths as depicted in fig. 3.1. This cannot be done simultaneously for both paths, as it would only weaken the overall intensity, without gaining any path information.

When the absorber is in path I the wavefunction before the third plate is given by

$$\begin{aligned} |\Psi'\rangle &= \left(e^{+i\chi/2}\sqrt{T_{abs}}\hat{\Pi}_I + e^{-i\chi/2}\hat{\Pi}_{II}\right)|\psi_i\rangle \\ &= \frac{1}{\sqrt{2}}\left(e^{+i\chi/2}\sqrt{T_{abs}}|\uparrow_x\rangle|I\rangle + e^{-i\chi/2}|\downarrow_x\rangle|II\rangle\right). \end{aligned} \quad (3.6)$$

Since the postselection removes the $|\uparrow_x\rangle$ -spin component, the resulting intensity is just

$$I_O = \frac{1}{2}, \quad (3.7)$$

with no influence of the absorber. For the case of an absorber only in path II, the

wavefunction is given by

$$\begin{aligned} |\Psi'\rangle &= \left(e^{+i\chi/2} \hat{\Pi}_I + e^{-i\chi/2} \sqrt{T_{abs}} \hat{\Pi}_{II} \right) |\psi_i\rangle \\ &= \frac{1}{\sqrt{2}} \left(e^{+i\chi/2} |\uparrow_x\rangle |I\rangle + e^{-i\chi/2} \sqrt{T_{abs}} |\downarrow_x\rangle |II\rangle \right), \end{aligned} \quad (3.8)$$

which, after postselection, results in an intensity of

$$I_O = \frac{T_{abs}}{2}, \quad (3.9)$$

which is reduced in comparison to the intensity without an absorber in path II. In this sense a measurement of the neutron's path degree of freedom suggests it takes path II. This also corresponds to the weak value result

$$\langle \hat{\Pi}_I \rangle_w = 0 \quad \text{and} \quad \langle \hat{\Pi}_{II} \rangle_w = 1.$$

A point of critique for this method of measuring the path localization is, that the interaction of the neutron with the absorber is not of unitary nature regarding the interferometer quantum state, since the amplitude for one path is reduced. Also, this method does not allow to differentiate between the path markings of both paths. When on the other hand the energy degree of freedom is used to mark the paths, they could be subject to partial shifts in energy with different amounts of $\Delta E = \hbar\omega_j$ corresponding to the different paths. This way of measuring the path localization could be carried out simultaneously for both paths.

3.2 Resonant Frequency Spin Flippers

This section covers how the spin degree of freedom can be manipulated using so called resonant-frequency (RF) spin-flippers. In the main experiment of this work, this is of importance, not only for the postselection, but also to probe the Cheshire Cat state for its response to small localized additional spin rotations on the two paths.

As stated above, in order to have a defined spin-rotation by means of Larmor precession, a sudden magnetic field change from a region with free evolution of the quantum state to a limited region, where the desired rotation takes place, is necessary. With the RF-flipper, oscillating currents are used, in order to have the non-adiabaticity ensured by a rapid field change in time. The RF-flipper is a device that produces an oscillating magnetic field B_1 in the direction of neutron

flight which is superimposed with the guide-field B_0 [22].

$$\vec{B}(t) = \begin{pmatrix} B_1 \cos(\omega t) \\ 0 \\ B_0 \end{pmatrix} \quad (3.10)$$

In order to have a spin rotation, a resonance condition between the oscillating and constant fields has to be fulfilled. The working principle is simply described as follows:

Suppose a frame of reference, which moves with the neutron and is rotating around its center of mass with an angular velocity corresponding to the Larmor rotation. The oscillating field B_1 in the x-direction can be thought of as a superposition of two circularly counter-rotating fields in the x-y-plane with frequency ω . When the guide-field B_0 has the right magnitude, a rotation of the spin due to Larmor precession would be in phase with one of the counter-rotating components. The other component would be rotating with double the velocity in the other direction and therefore average out over time (rotating wave approximation). This would mean one of the rotating field components is fixed with respect to the spin in the rotating frame of reference. This creates a constant axis for the spin to revolve around by virtue of, again, Larmor precession. The rotation angle is proportional to the oscillating field component B_1 .

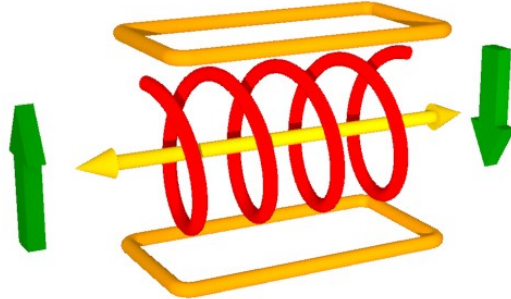


Figure 3.2: Schematic depiction of the RF-flipper doing a π -spin-flip. Locally tunable guide field coil in yellow, RF-coil in red.

The resonance condition is

$$\omega_{res} = \frac{2|\mu|B_0}{\hbar} \left(1 + \frac{B_1^2}{16B_0^2} \right), \quad (3.11)$$

the second term being a correction due to the rotating wave approximation. For the

purpose of setting up the RF-flipper, given a desired frequency f , it is convenient to use the approximate resonant condition $B_0[\text{G}] \sim \frac{1}{3}f[\text{kHz}]$ as a starting point for the guide field. The action of the RF-flipper on the spinor of a neutron wavefunction can be written as a unitary matrix [23]

$$\mathcal{U}_{RF}(\beta, \omega) = \begin{pmatrix} \cos\left(\frac{\beta}{2}\right) & -i \sin\left(\frac{\beta}{2}\right) e^{+i\omega t} \\ -i \sin\left(\frac{\beta}{2}\right) e^{-i\omega t} & \cos\left(\frac{\beta}{2}\right) \end{pmatrix}, \quad (3.12)$$

with the rotation angle $\beta \propto B_1$ and resonant frequency ω . From the off diagonal entries one can tell that the energy of the flipped parts of the spinor are shifted by $\Delta E = -\hbar\omega$. Another way of writing eq. (3.12) is given by

$$\begin{aligned} \mathcal{U}_{RF}(\beta, \omega) &= \cos\left(\frac{\beta}{2}\right) \mathbb{1} - i \sin\left(\frac{\beta}{2}\right) \begin{pmatrix} 0 & \cos\omega t + i \sin\omega t \\ \cos\omega t - i \sin\omega t & 0 \end{pmatrix} \\ &= \cos\left(\frac{\beta}{2}\right) \mathbb{1} - i \sin\left(\frac{\beta}{2}\right) (\cos\omega t \hat{\sigma}_x - \sin\omega t \hat{\sigma}_y), \end{aligned} \quad (3.13)$$

which makes clear that the spin rotation occurs around an axis that rotates with frequency ω in the x-y-plane.

For later use we write the expansion of eq. (3.12) for small β up to the first order

$$\begin{aligned} \mathcal{U}_{RF}(\beta, \omega) |\uparrow_z\rangle &= \begin{pmatrix} 1 & -i\frac{\beta}{2}e^{+i\omega t} \\ -i\frac{\beta}{2}e^{-i\omega t} & 1 \end{pmatrix} \begin{pmatrix} 1 \\ 0 \end{pmatrix} + \mathcal{O}(\beta^2) \\ &\approx |\uparrow_z\rangle - i\frac{\beta}{2}e^{-i\omega t} |\downarrow_z\rangle \end{aligned} \quad (3.14)$$

and the same for a rotation angle of $\pi - \beta$

$$\begin{aligned} \mathcal{U}_{RF}(\pi - \beta, \omega) |\uparrow_z\rangle &= \mathcal{U}_{RF}(\pi, \omega) * \mathcal{U}_{RF}(-\beta, \omega) |\uparrow_z\rangle \\ &= \begin{pmatrix} \frac{\beta}{2} & -ie^{+i\omega t} \\ -ie^{-i\omega t} & \frac{\beta}{2} \end{pmatrix} \begin{pmatrix} 1 \\ 0 \end{pmatrix} + \mathcal{O}(\beta^2) \\ &\approx \frac{\beta}{2} |\uparrow_z\rangle - ie^{-i\omega t} |\downarrow_z\rangle. \end{aligned} \quad (3.15)$$

For $\beta = \pi/2$ and incident spin $|\uparrow_z\rangle$ the resulting wavefunction is a spin rotating in the x-y-plane with frequency ω .

$$\begin{aligned} \mathcal{U}_{RF}(\pi/2, \omega) |\uparrow_z\rangle &= \frac{1}{\sqrt{2}} \begin{pmatrix} 1 & -ie^{+i\omega t} \\ -ie^{-i\omega t} & 1 \end{pmatrix} \begin{pmatrix} 1 \\ 0 \end{pmatrix} \\ &= \frac{1}{\sqrt{2}} (|\uparrow_z\rangle - ie^{-i\omega t} |\downarrow_z\rangle) \end{aligned} \quad (3.16)$$

3.3 Simultaneous Spin Localization Measurement

This section explains, how a measurement that finds the spin property of the neutron in one interferometer arm but not in the other, can be carried out using RF-flippers. Suppose a three plate interferometer with two RF-flippers in the two paths as depicted in fig. 3.3. The pre and postselected states can be written exactly as already presented in section 2.5

$$|\psi_i\rangle = \frac{1}{\sqrt{2}} |\uparrow_z\rangle (|I\rangle + |II\rangle) \quad \text{and} \quad |\psi_f\rangle = \frac{1}{\sqrt{2}} (|\downarrow_z\rangle |I\rangle + |\uparrow_z\rangle |II\rangle).$$

preselection is carried out by the magnetic prism polarizer and postselection by the two RF-flippers in the two paths, one doing a π -flip, the other doing no flip at all. Now, in order to measure the response of the system, small deviations from these rotation angles, β_I and β_{II} respectively, are introduced. From a conceptual standpoint we assume here two distinct spin rotators in path I, one that is solely responsible for postselecting the state and the other to introduce a small additional spin rotation beforehand. Since there is limited space available and the outcome is no different from the easily realizable case of only one RF-flipper, that rotates the spin around an angle that deviates from the postselection angle π by β_I , the latter option is chosen.

When the incoming wavefunction is given by $|\Psi_0\rangle = |\uparrow_z\rangle e^{-i\omega_0 t}$, the quantum state right before the last interferometer plate in this case can be written as

$$\begin{aligned} |\Psi'\rangle &= |I'\rangle + |II'\rangle \\ &= \frac{1}{\sqrt{2}} e^{-i\omega_0 t} [\mathcal{U}_{RF}(\pi - \beta_I, \omega_{RF}) |\uparrow_z\rangle |I\rangle + \mathcal{U}_{RF}(\beta_{II}, \omega_{RF}) |\uparrow_z\rangle |II\rangle]. \end{aligned} \quad (3.17)$$

Putting in the approximations for \mathcal{U}_{RF} up to the first order in β (using eqs. (3.14) and (3.15)) gives

$$\begin{aligned} |\Psi'\rangle &\approx \frac{1}{\sqrt{2}} e^{-i\omega_0 t} \left[\left(\frac{\beta_I}{2} |\uparrow_z\rangle - |\downarrow_z\rangle i e^{-i\omega_{RF} t} \right) |I\rangle e^{+i\chi/2} + \right. \\ &\quad \left. + \left(|\uparrow_z\rangle - \frac{\beta_{II}}{2} |\downarrow_z\rangle i e^{-i\omega_{RF} t} \right) |II\rangle e^{-i\chi/2} \right]. \end{aligned} \quad (3.18)$$

The supermirror filter out all the $|\downarrow_z\rangle$ -spins in the beam, therefore the wavefunction after the analyzer is given by

$$|\Psi''\rangle \approx \frac{1}{\sqrt{2}} e^{-i\omega_0 t'} \left[\frac{\beta_I}{2} |\uparrow_z\rangle e^{+i\chi/2} + |\uparrow_z\rangle e^{-i\chi/2} \right]. \quad (3.19)$$

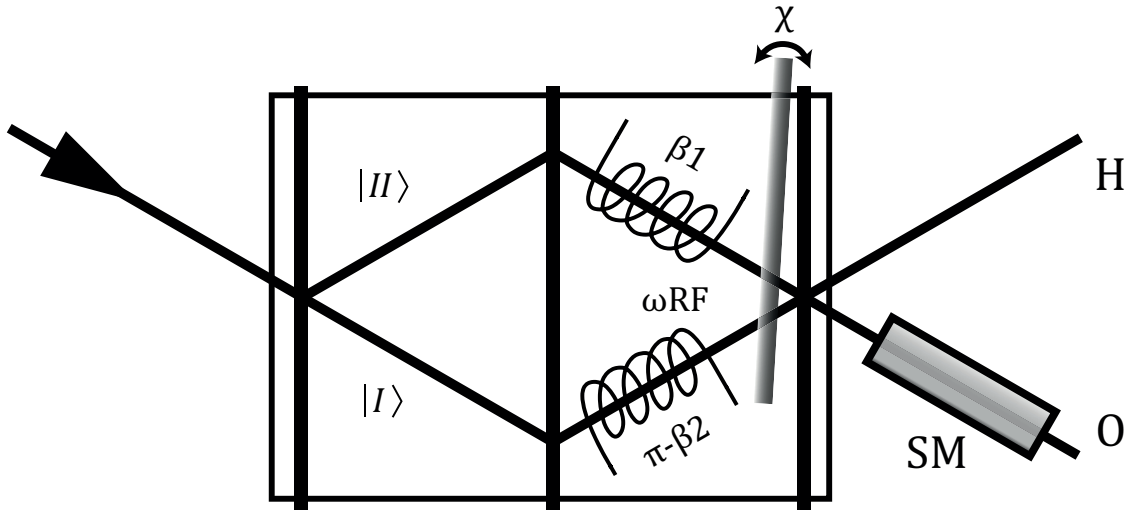


Figure 3.3: Schematic depiction of a three plate interferometer with two RF-flippers in the two paths and a supermirror analyzer before the O detector.

Now taking the absolute square, the intensity of the O beam can be written in the form

$$I_O(\chi) \approx \frac{1}{2} + \frac{\beta_I}{2} \cos \chi, \quad (3.20)$$

which only depends on β_I in the first order. If the deviation angles β are chosen sufficiently small, only the linear response is appreciable in the intensity measurement. In this sense the spin property of the neutron, given pre and postselection, takes path I.

3.4 Realization of a Which Way Measurement for Neutrons

The motivation for the experiment carried out in the course of this diploma thesis was to improve the Cheshire Cat experiment of 2014 in a way, such that the weak perturbations used in order to probe the quantum state for its spin and path localization are all applied simultaneously. As stated above, the path localization measurement using weak absorbers cannot be applied for both paths simultaneously. Also the non-unitarity of the absorbers nuclear interaction was criticized.

The first idea that was considered theoretically was to take the setup from the 2014 experiment and replace the weakly absorbing foils with two RF-Flippers operating at different frequencies ω_I and ω_{II} , which would make a small angle spin-rotation, in order to introduce an energy shift in the flipped part, i.e. a factor $e^{-i\omega_j t}$. The plan was for this factor to lead to an interference term with the initial energy $e^{-i\omega_0 t}$, which would make the intensity oscillate with frequency ω_j [9]. Then, if only one frequency, e.g. ω_I is detected in the intensity measurement, this suggests $\langle \hat{\Pi}_{II} \rangle_w = 0$. This proposed setup is illustrated in fig. 3.4. The

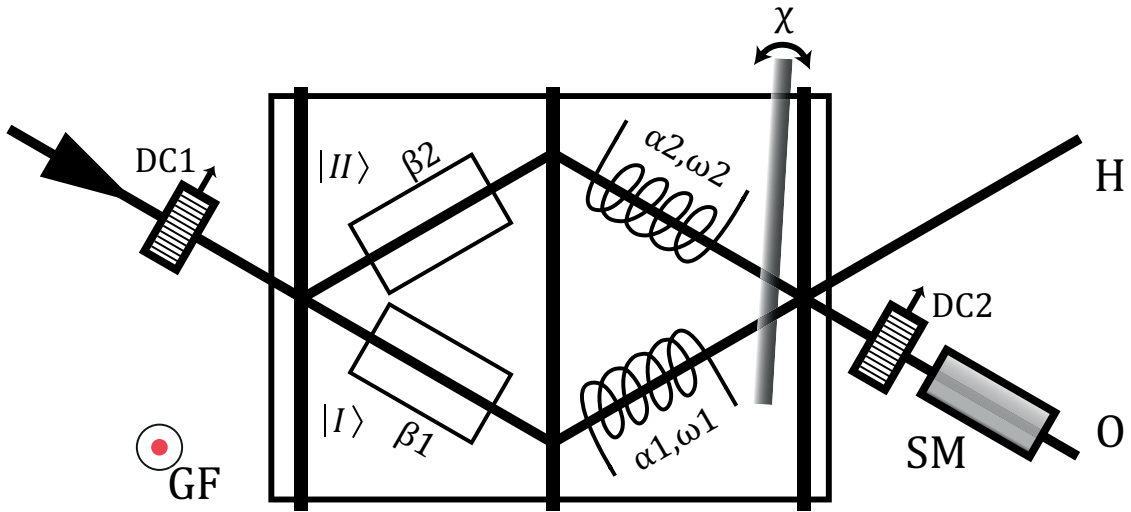


Figure 3.4: Schematic depiction of the Cheshire Cat experimental setup from 2014 with RF-flippers in place for the weakly absorbing foil between second and third interferometer plate.

problem with this setup is, that the RF-flippers produce a spin-rotation around a rotating axis in the x-y-plane. When one looks at the weak values expected for a rotation around such an axis specified by angle ξ , such that $\hat{\sigma}_\xi = \hat{\sigma}_x \cos \xi + \hat{\sigma}_y \sin \xi$, assuming pre and postselected states of the 2014 experiment, written in eqs. (3.1) and (3.2), which are given by

$$\langle \hat{\sigma}_\xi \hat{\Pi}_I \rangle_w = -i \sin \xi \quad \text{and} \quad \langle \hat{\sigma}_\xi \hat{\Pi}_{II} \rangle_w = -\cos \xi \quad (3.21)$$

one notices, that they are nonzero on both paths. Therefore, both RF-flippers would have an appreciable effect on the quantum state between pre and postselection, since ξ changes periodically in time. Also, argumentatively it is not possible

to separate the effect of the RF-flipper onto the time-dependent part of the wavefunction, i.e. the energy, from the spin rotation it causes, in order to conclude the spin and path degree of freedom are localized on opposite interferometer arms. Another way of accessing the neutrons energy without changing the spin state had to be devised.

3.5 Energy Manipulator Coils

The most easily accessible property of a neutron in the experiment is the spin, it serves to create orthogonal states in the two paths, a key element of the Quantum Cheshire Cat state. However, the spin state cannot simultaneously be used as a which-way marker for the neutron's path degree of freedom. The next property which comes to mind is the neutron's energy, being present in the time-dependent part of the wavefunction, e.g. when it is modeled as a plane wave

$$e^{i(\vec{k}\vec{x} - \omega_0 t)}, \quad \omega_0 = \frac{E_0}{\hbar}.$$

If it is possible to manipulate the energy a certain way in a finite region inside the interferometer, this could lead to a time-oscillation of the intensity at the detector with a frequency corresponding to the localized influence. For this reason the energy-manipulator coil (EM) is used, it serves as a way to shift the energy without causing a rotation of the spin. The detected frequency of the intensity oscillation is then a which-way marker for the neutron's path.

3.5.1 Theoretical Treatment

The EM-coil consists of a pair of Helmholtz coils that produce an oscillating magnetic field in the z-direction (see fig. 3.5), so that the overall field inside the coil becomes

$$\vec{B}(t) = \begin{pmatrix} 0 \\ 0 \\ B_0 + B_1 \cos \omega t \end{pmatrix} \quad (3.22)$$

with the static guide field B_0 , which surrounds the EM-coil. What happens to a neutron that traverses three consecutive regions, the middle region having a magnetic field as in eq. (3.22), and the outer regions only B_0 in the z-direction, is formally treated in [24], here only the results are presented. When the incoming neutron wavefunction is given by

$$|\psi_i\rangle = |\uparrow_z\rangle |E_0\rangle = |\uparrow_z\rangle e^{-i\omega_0 t}, \quad (3.23)$$

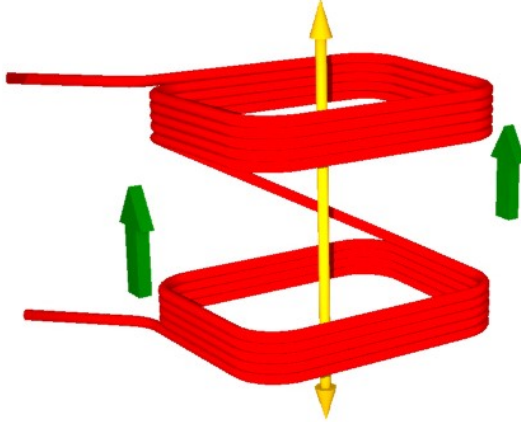


Figure 3.5: Schematic depiction of the EM-coil. Spin direction is left unchanged.

the wavefunction after the EM-coil is given by

$$|\psi'\rangle = \mathcal{U}_{EM}(\alpha, \omega) |\psi_i\rangle = \sum_{n=-\infty}^{+\infty} J_n(\alpha) |\uparrow_z\rangle e^{-i(\omega_0+n\omega)t}, \quad (3.24)$$

with the Bessel functions of the first kind J_n . The interaction strength

$$\alpha = \frac{\mu B_1}{\hbar \omega} \sin(\omega \tau / 2) \quad (3.25)$$

is a function of the magnetic field strength B_1 , the frequency ω and the time of flight trough the oscillating field region τ . One can see that the EM-coil has no effect, if τ is equal to an integer number of periods of the oscillation and the sine term vanishes. Intuitively this makes sense, because the neutron has the same potential energy upon entry and exit of the EM-coil. When the incident neutrons are polarized in the $|\uparrow_z\rangle$ state the oscillating field in the z-direction cannot change the spin direction. However, the EM-coil creates shifts in energy $\Delta E = \pm n\hbar\omega$ of the initial wavefunction with amplitudes $J_n(\alpha)$, which corresponds to a one photon exchange between the neutron and the oscillating field. In a series expansion for small α up to the first order this leads to

$$\begin{aligned} |\psi'\rangle &= |\uparrow_z\rangle e^{-i\omega_0 t} (J_0(\alpha) + J_1(\alpha)e^{-i\omega t} + J_{-1}(\alpha)e^{+i\omega t} + \mathcal{O}(\alpha^2)) \\ &= |\uparrow_z\rangle e^{-i\omega_0 t} (J_0(\alpha) + J_1(\alpha)(e^{-i\omega t} - e^{+i\omega t}) + \mathcal{O}(\alpha^2)) \\ &= |\uparrow_z\rangle e^{-i\omega_0 t} (1 - i\alpha \sin \omega t + \mathcal{O}(\alpha^2)), \end{aligned} \quad (3.26)$$

using $J_{-n} = (-1)^n J_n$, $J_0(\alpha) \approx 1$ and $J_1(\alpha) \approx \frac{\alpha}{2}$. Since the influence of the EM-coil onto the neutron wavefunction appears only in the imaginary component in the first order, this effect cannot be seen in an intensity measurement of a single beam but needs to be resolved interferometrically together with a reference beam. An interpretation of the action of the EM-coil in terms of state vectors can be written as

$$\begin{aligned} |\psi'\rangle &= \mathcal{U}_{EM}(\alpha, \omega) |\uparrow_z\rangle |E_0\rangle \\ &= |\uparrow_z\rangle (J_0(\alpha) |E_0\rangle + J_1(\alpha) |E_0 + \hbar\omega\rangle + J_{-1}(\alpha) |E_0 - \hbar\omega\rangle + \mathcal{O}(\alpha^2)) \quad (3.27) \\ &\approx |\uparrow_z\rangle (|E_0\rangle + \frac{\alpha}{2}(|E_0 + \hbar\omega\rangle - |E_0 - \hbar\omega\rangle)). \end{aligned}$$

and is visualized in fig. 3.6.

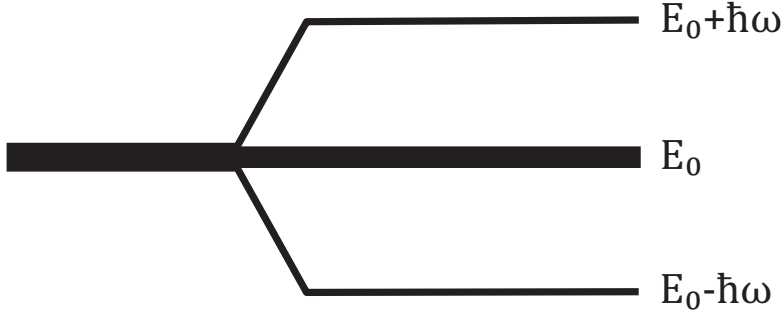


Figure 3.6: Visualization of the shift in energy caused by the EM-coil.

3.5.2 Associated Experiment by Summhammer

An experimental study of the effect an EM-coil has, when it is placed inside a neutron interferometer, was carried out by Summhammer et al. in 1995 [10]. In this work the oscillating magnetic field parallel to the external guide field is produced by a magnetic C-shaped yolk consisting of alternating layers of cardboard and metal sheet, which is placed in one arm of a two-path interferometer (see fig. 3.7). The polarized neutrons pass through the gap in the yolk above and below which driving coils are wound, which induce the oscillating field. The gap is 7 mm high, 14 mm wide, and measures 21 mm along the neutron trajectory. The field oscillates with a frequency of 7534 Hz, a value limited by the time resolution of the neutron detection. Time-dependent neutron detection in the O beam is conducted via a multichannel scaler card that runs time-locked to the field. A

period of the oscillation is divided into 64 bins of width $2.07\mu\text{s}$. An empirical expression for the intensity of the O beam presented in the paper is given by

$$I_O(\chi, t) \propto |e^{i\chi} \psi_i + \psi'|^2 = 1 + 2 \sum_{j=-\infty}^N |u_j| \cos(\phi_j + \chi - j\omega t), \quad (3.28)$$

where ψ_i and ψ' are the same as from eqs. (3.23) and (3.24), amplitudes $u_j = J_n(s\alpha)$ are the Bessel functions with a scaling constant s , and ϕ_j relative phases. From three runs with different settings of the phase shifter χ , the amplitudes $|u_j|$ could be extracted from Fourier transforms of the time-dependent intensity measurements. The result is depicted in fig. 3.8.

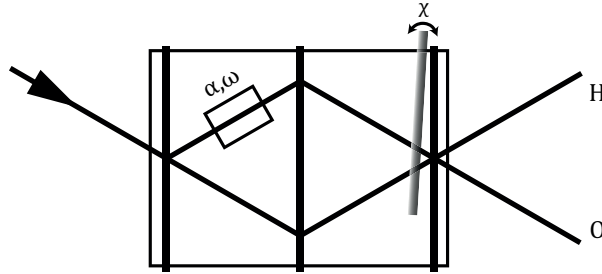


Figure 3.7: Schematic depiction of the experimental setup from the 1995 paper by Summhammer et al.

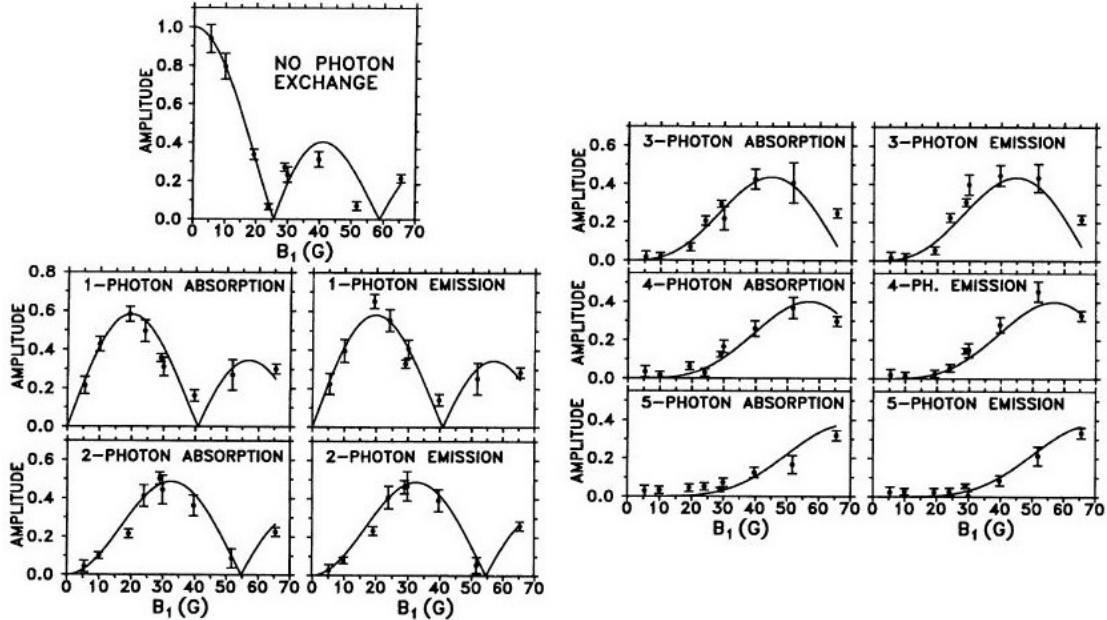


Figure 3.8: Photon exchange amplitudes extracted from Fourier data as a function of the oscillating field amplitude. Solid lines are plots of the corresponding Bessel functions fitted with the scaling constant s as the only free parameter. Normalization, such that the total exchange probability from exchanges of -10 to $+10$ photons is equal to 1. Taken from ref. [10].

3.6 Experimental Scheme

In this section the final setup for a simultaneous Cheshire Cat measurement is presented. The calculation for the intensity of the O beam is carried out, when the neutron wavefunction inside the interferometer is subject to the various manipulator devices discussed above. The experimental arrangement is depicted in fig. 3.9. The upper beam between second and third interferometer plate is used as a reference beam and is labeled $|R\rangle$, the middle beam is $|II\rangle$ and the lower beam is $|I\rangle$. The spatial separation of spin and path degree of freedom, the key feature of the Cheshire Cat state, happens on the sub loop of the interferometer between the second and fourth plate on path $|I\rangle$ and $|II\rangle$.

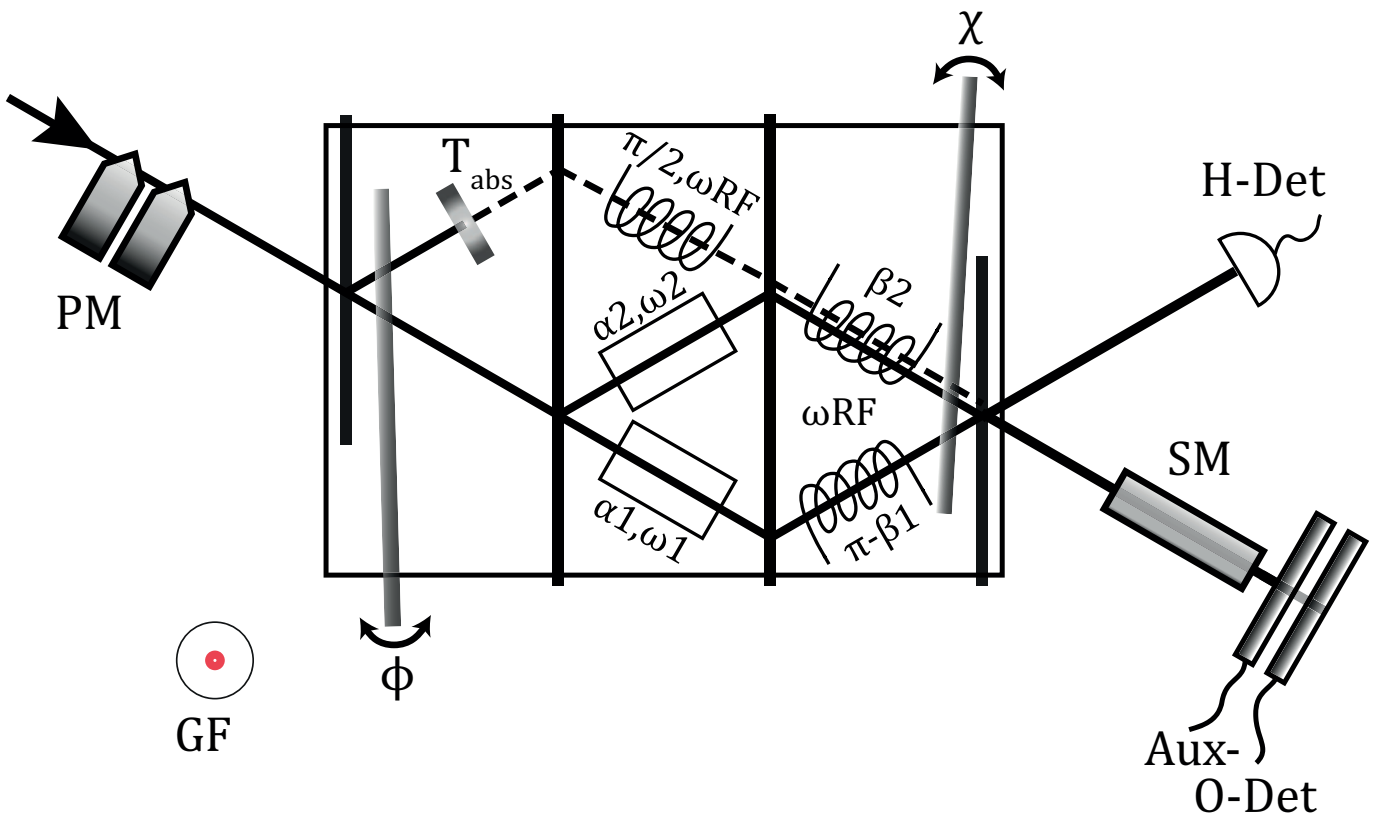


Figure 3.9: Schematic depiction of the interferometer with all parts used for the experiment.

Monochromatized neutrons with wavelength $\lambda \approx 1.9 \text{ \AA}$ go through a pair of polarizing magnets and enter the interferometer with spin $|\uparrow_z\rangle$. At the first interferometer plate the reference beam is branched off and attenuated with an absorber T_{abs} . The

reference beam subsequently undergoes a spin rotation by an angle of $\pi/2$ using an RF-flipper in order to consist of $|\uparrow_z\rangle$ and $|\downarrow_z\rangle$ in equal parts. After the second interferometer plate beam $|I\rangle$ goes through an EM-coil operating at frequency ω_I and through an RF-flipper that makes a rotation by an angle of $\pi - \beta_I$. In this case the π -rotation corresponds to the postselected state, and β_I is a weak disturbance of the spin. Beam $|II\rangle$ first goes through an EM-coil operating at frequency ω_{II} and then through an RF-flipper that makes a rotation by the small angle β_{II} . The reference beam is also rotated by β_{II} , but because of the attenuation through T_{abs} this effect can be neglected. After that, the beams recombine at the fourth interferometer plate to form the O beam, which then goes through the analyzing supermirror, that only transmits $|\uparrow_z\rangle$ -spins to pass on to the time-dependent detectors. In the notation of pre and postselection, the pre selected state is given by

$$|\Psi_i\rangle = \frac{1}{\sqrt{2}} |\uparrow_z\rangle |E_0\rangle (|I\rangle + |II\rangle) \quad (3.29)$$

and is prepared directly after the second interferometer plate and the postselected state is given by

$$|\Psi_f\rangle = \frac{1}{\sqrt{2}} (|\downarrow_z\rangle |I\rangle + |\uparrow_z\rangle |II\rangle) \quad (3.30)$$

and is selected through a combination of RF-flipper in path I and the supermirror.

3.6.1 Calculation of the O Beam Intensity

Here the calculation is carried out without the use of the formalism of pre and postselection, just by developing the initial wavefunction further using the mathematical results from above. The reference beam is needed, in order to interferometrically resolve the which-way marking of the path using the neutron's energy state. Suppose the incident neutron beam can be written as $|\Psi_0\rangle = |\uparrow_z\rangle |E_0\rangle = |\uparrow_z\rangle e^{-i\omega_0 t}$. Then, the quantum state after the first interferometer plate is given by

$$\begin{aligned} |\Psi'\rangle &= |R'\rangle + |\Psi'_0\rangle \\ &= A [\sqrt{T_{abs}} |\uparrow_z\rangle |E_0\rangle |R\rangle e^{-i\phi/2} + |\Psi'_0\rangle e^{+i\phi/2}], \end{aligned} \quad (3.31)$$

with A being a normalization constant. The $|R\rangle$ beam is weakened by an absorber with transmission T_{abs} . The preselected state is prepared after the splitting of $|\Psi'_0\rangle$ into $|I\rangle$ and $|II\rangle$ at the second interferometer plate: $|\Psi'_0\rangle \rightarrow |\Psi_i\rangle = \frac{1}{\sqrt{2}} |\uparrow_z\rangle |E_0\rangle (|I\rangle + |II\rangle)$.

Between second and third plate the quantum state is given by

$$\begin{aligned}
|\Psi''\rangle &= |R''\rangle + |II'\rangle + |I'\rangle \\
&= A \left[\mathcal{U}_{RF}(\pi/2, \omega_{RF}) \sqrt{T_{abs}} |\uparrow_z\rangle |E_0\rangle |R\rangle e^{-i\phi/2} + \right. \\
&\quad + \mathcal{U}_{EM}(\alpha_{II}, \omega_{II}) |\uparrow_z\rangle |E_0\rangle |II\rangle e^{+i\phi/2} + \\
&\quad \left. + \mathcal{U}_{EM}(\alpha_I, \omega_I) |\uparrow_z\rangle |E_0\rangle |I\rangle e^{+i\phi/2} \right],
\end{aligned} \tag{3.32}$$

The weakened beam $|R\rangle$ undergoes a spin rotation by $\pi/2$ into the x-y-plane using an RF-flipper in order to show interference with $|\uparrow_z\rangle$ and $|\downarrow_z\rangle$ spins equally. For the which-way measurement beams $|I\rangle$ and $|II\rangle$ go through two EM-coils operating at different frequencies ω_I and ω_{II} respectively. This way an intensity oscillation at the detector with frequency ω_j indicates the neutron was traveling along path $|j\rangle$. After the third plate beam $|II\rangle$ and $|R\rangle$ are combined and further referred to as only $|II\rangle$. Now beams $|I\rangle$ and $|II\rangle$ go through two RF-flippers and are turned by the angles $\pi - \beta_I$ and β_{II} respectively. This, together with the polarizing supermirror, serves to create the orthogonal spin states of the postselected state $|\Psi_f\rangle = \frac{1}{\sqrt{2}}(|\downarrow_z\rangle |I\rangle + |\uparrow_z\rangle |II\rangle)$. The small angles β_j are introduced in order to probe the spin system for its path localization. Between the third and fourth plate the state is given by

$$\begin{aligned}
|\Psi'''\rangle &= |II''\rangle + |I''\rangle \\
&= A' \left[\mathcal{U}_{RF}(\beta_{II}, \omega_{RF}) \mathcal{U}_{RF}(\pi/2, \omega_{RF}) \sqrt{T_{abs}} |\uparrow_z\rangle |E_0\rangle |II\rangle e^{-i\phi/2} e^{-i\chi/2} + \right. \\
&\quad + \mathcal{U}_{RF}(\beta_{II}, \omega_{RF}) \mathcal{U}_{EM}(\alpha_{II}, \omega_{II}) |\uparrow_z\rangle |E_0\rangle |II\rangle e^{+i\phi/2} e^{-i\chi/2} + \\
&\quad \left. + \mathcal{U}_{RF}(\pi - \beta_I, \omega_{RF}) \mathcal{U}_{EM}(\alpha_I, \omega_I) |\uparrow_z\rangle |E_0\rangle |I\rangle e^{+i\phi/2} e^{+i\chi/2} \right]
\end{aligned} \tag{3.33}$$

Putting in $|E_0\rangle = e^{-i\omega_0 t}$ and the approximations from the previous section for the unitary matrices \mathcal{U}_{RF} and \mathcal{U}_{EM} up to the first order in α and β using eqs. (3.14)–(3.16) and (3.26) gives

$$\begin{aligned}
|\Psi'''\rangle &\approx A' e^{-i\omega_0 t} \left[\sqrt{\frac{T_{abs}}{2}} \left((1 - \frac{\beta_{II}}{2}) |\uparrow_z\rangle - (1 + \frac{\beta_{II}}{2}) |\downarrow_z\rangle i e^{-i\omega_{RF}t} \right) |II\rangle e^{-i\phi/2} e^{-i\chi/2} + \right. \\
&\quad + \left(|\uparrow_z\rangle - \frac{\beta_{II}}{2} |\downarrow_z\rangle i e^{-i\omega_{RF}t} \right) (1 - i\alpha_{II} \sin \omega_{II} t) |II\rangle e^{+i\phi/2} e^{-i\chi/2} + \\
&\quad \left. + \left(\frac{\beta_I}{2} |\uparrow_z\rangle - |\downarrow_z\rangle i e^{-i\omega_{RF}t} \right) (1 - i\alpha_I \sin \omega_I t) |I\rangle e^{+i\phi/2} e^{+i\chi/2} \right]
\end{aligned} \tag{3.34}$$

The recombination of the sub beams at the fourth interferometer plate and the subsequent action of the supermirror analyzer, filtering out the $|\downarrow_z\rangle$ spin component, leaves

$$\begin{aligned} |\Psi'''\rangle \approx A'e^{-i\omega_0 t'} |\uparrow_z\rangle & \left[\sqrt{\frac{T_{abs}}{2}} (1 - \frac{\beta_{II}}{2}) e^{-i\phi/2} e^{-i\chi/2} + \right. \\ & + (1 - i\alpha_{II} \sin \omega_{II} t') e^{+i\phi/2} e^{-i\chi/2} \\ & \left. + \frac{\beta_I}{2} (1 - i\alpha_I \sin \omega_I t') e^{+i\phi/2} e^{+i\chi/2} \right]. \end{aligned} \quad (3.35)$$

Now taking the absolute square and neglecting nonlinear terms α^2 , β^2 and $\alpha\beta$, and also $\sqrt{\frac{T_{abs}}{2}}\beta$, since it is small in the experiment, results in the final intensity of the O beam

$$\begin{aligned} I_O(t) &= |\langle \Psi''' | \Psi'''\rangle|^2 \\ &\propto 1 + \frac{T_{abs}}{2} + \beta_I \cos \chi + \sqrt{2 T_{abs}} (\cos \phi + \alpha_{II} \cos \omega_{II} t \sin \phi). \end{aligned} \quad (3.36)$$

This relation suggests, that linear influences on the spin of the pre and postselected ensemble are only caused by the spin-rotation angle β_{II} in path II and the intensity oscillates only with frequency ω_I coming from the EM-coil in path I. This effect can be verified experimentally by switching off, i.e. setting zero, one of the four disturbances $\alpha_I, \alpha_{II}, \beta_I, \beta_{II}$, one after the other for the duration of one measurement, and looking for the effect on the (time-dependent) intensity measurement. In this sense the spin and path degree of freedom become spatially separated, since only α_I and β_{II} have a linear influence on the intensity, which happens on opposite interferometer arms I and II.

The effect of perturbation β_{II} influences the spin on path II and therefore the cat's grin and α_I shifts the energy on path I and therefore has an influence on the body of the cat. This corresponds to the spin and path weak values in eqs. (2.26) and (2.27)

4 Neutron Optical Setup

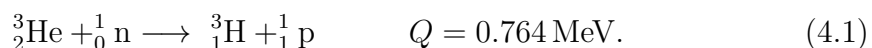
This chapter is dedicated to the parts needed for interferometric experiments with neutrons. It gives a more detailed description how the interferometer works together with the phase shifter plates and neutron detectors. The devices used for pre and postselection of the quantum state, namely the polarizing magnets and analyzing supermirror, are described. In the end it is explained, how the the RF and EM-coils introduced in the previous chapter are realized in the limited available space inside the interferometer, and how the whole experiment can be operated automatically with a computer.

4.1 Neutron Source

The experiment was carried out by using the research reactor at the Institute Laue-Langevin in Grenoble, France. With a peak flux of $\sim 1.5 \times 10^{15} \text{ cm}^{-1} \text{s}^{-1}$ at the moderator of the reactor running at 58 MW power it is the neutron source with the highest flux worldwide. Thermal neutrons are guided to the experimental areas using total reflection below the critical angle inside rectangular beam tubes. Neutrons of a definite wavelength ($\lambda \approx 1.9 \text{ \AA}$, corresponding to a velocity of $\sim 2080 \text{ m/s}$) are selected by the monochromator crystal and reflected under a Bragg angle of 30° into the experimental region. After the interferometer typical detector count rates are of the order of $\sim 10 \text{ cm}^{-1} \text{s}^{-1}$, when all spin manipulation devices are present inside the interferometer.

4.2 Neutron Detectors

The neutron as a particle without electrical charge can only be detected indirectly after producing ionized particles via a nuclear reaction, e.g.



The energy of 0.764 MeV released in this reaction is distributed onto the decay products. ${}^3_2\text{He}$ is used because it has a large cross section for neutrons in the experimental energy range. It is contained as a gas in a counter tube, where the tubing acts as a cathode and a fine wire in the center is the anode, with applied

voltages typically around 1000 – 1500 V. When the charged particles produced inside the gas volume accelerate due to the high voltage, a charge avalanche is created that leads to a sudden voltage drop between anode and cathode, which, after amplification, is registered as a neutron count signal. When no time resolved measurement is needed, bigger counter tubes are used and the neutrons enter in axial direction, having a bigger reaction volume. For a time resolved measurement, smaller detectors (diameter ~ 7 mm) are placed, such that the neutrons enter in a direction perpendicular to the cylinder axis. This allows for a time resolution of at least $\frac{7\text{mm}}{2080\text{m/s}} \sim 3.4\mu\text{s}$.



Figure 4.1: Photograph of the small neutron detector used for time-dependent measurements. Size comparison with a standard pencil. Both end parts are isolated with heat shrink tube. The bulge in the left end is produced by a clamp used to connect the outer wire of the coaxial cable with the detector tubing, a bad connection suspected to be the cause of a problematic blind count rate, as mentioned later on.

4.3 Perfect Crystal Interferometer and Phase Shifter Plates

The experiment carried out in the course of this diploma thesis makes use of a four plate interferometer (see fig. 4.2). It is cut from a perfect silicone crystal such that the (2, 2, 0) crystal plane is perpendicular to the surface of the four plates, as can be seen in fig. 4.3, which is the so called Laue configuration. When a neutron beam hits the first interferometer plate at the Bragg angle θ_B , the intensity is roughly split 50 : 50 between the reflected and transmitted beam. At the second and third plate the same situation occurs, so that the sub beams are recombined at the fourth plate, where the so called O beam leaves the interferometer in parallel to the incident neutrons, and the H beam is reflected under the Bragg angle. Sub beams leaving the interferometer at the second and third plate are not used for the experiment. In order to have a coherent superposition of the reflected neutron

wavefunctions at the third and fourth interferometer plate, it is essential that all refractive planes are aligned with a precision comparable to the lattice parameter. In comparison with a standard three plate interferometer, where the incident beam is split into two parts and then recombined, the four plate geometry offers three independent paths for the neutron to interfere.

To observe interferometric phenomena, it is necessary to tune a phase shift between the wavefunctions of the sub beams. This is done with phase shifter plates. These are plates with a thickness in the range of 3-5 mm made of sapphire or silicon, that can be rotated by an angle of $\sim \pm 1.5^\circ$. After traversing the plate, the neutron wavefunction is subject to a phase shift due to the interaction with the nuclei of the material, which is proportional to [3]

$$\chi = -Nb_c\lambda D,$$

where N is the density of scatterers, b_c the nuclear scattering length, λ the neutron's wavelength and D the thickness of the plate. When the phase shifter plate is inserted between two interferometer plates (as in fig. 4.3) and rotated, the optical path length in the material is different for the two beams, which leads to a phase difference. This phase difference is in good approximation linear with the rotation angle of the plate. A rotation of the phase plates by the angle stated above leads to a difference in phase of about 2 – 3 times 2π . When the incident wavefunction is given by Ψ_0 , the intensity at the O detector can be written as

$$\begin{aligned} I_O &= |\Psi_I + \Psi_{II} + \Psi_{III}|^2 \\ &= \frac{1}{16}|\Psi_0|^2 |rrtt e^{-i\phi/2} e^{-i\chi/2} + trrt e^{+i\phi/2} e^{-i\chi/2} + ttrr e^{+i\phi/2} e^{+i\chi/2}|^2, \end{aligned} \quad (4.2)$$

where ϕ and χ are the phase differences introduced by the phase shifters in the front and back of the interferometer, and t and r the coefficients for transmission and reflection respectively. The result is

$$I_O(\phi, \chi) = A (3 + 2 \cos \phi + 2 \cos \chi + 2 \cos(\phi + \chi)), \quad (4.3)$$

with the constant $A = \frac{1}{16}|\Psi_0|^2|r|^4|t|^4$. Similarly for the H-beam intensity one finds

$$\begin{aligned} I_H(\phi, \chi) &= |\Psi_0|^2 |rrtr e^{-i\phi/2} e^{-i\chi/2} + trrr e^{+i\phi/2} e^{-i\chi/2} + ttrt e^{+i\phi/2} e^{+i\chi/2}|^2 \\ &= |\Psi_0|^2 |r|^2|t|^2 (2|r|^4 + |t|^4 + 2|r|^4 \cos \phi + 2|r|^2|t|^2 (\cos \chi + \cos(\phi + \chi))), \end{aligned} \quad (4.4)$$

which seems a bit more complicated. This is due to the fact, that for the O beam the number of transmissions and reflections is the same for all three interferometer

paths, whereas for the H beam it is not. The calculation above is valid only for an ideal case, where all beam splitters have the same t and r . In reality eq. (4.3) has to be modified in order to reflect the imperfections of the interferometer, where each reflection and transmission is accompanied by a loss of coherence. The modified equation reads

$$I_O(\phi, \chi) = A(3 + 2C_{I,II} \cos \phi + 2C_{II,III} \cos \chi + 2C_{I,III} \cos(\phi + \chi)), \quad (4.5)$$

where the coefficients $0 \leq C_{i,j} \leq 1$ give the contrast for interference between paths i and j . In practice contrast is measured by blocking one beam with an absorber, e.g. beam Ψ_I , then taking an interferogram by varying the angle of the phase plate, in this case χ , and measuring the count rate. The intensity in the O beam is then given by

$$I_O^{II,III}(\chi) = |\Psi_{II} + \Psi_{III}|^2 = |\Psi_0|^2 |r|^4 |t|^2 (1 + C_{II,III} \cos \chi). \quad (4.6)$$

When the interferogram is fitted with a sinusoidal of the form $A + B \sin(f\chi + D)$, the contrast of the O beam is then given by

$$C_{II,III} = \frac{B}{A} = \frac{I'_{O,max} - I'_{O,min}}{I'_{O,max} + I'_{O,min}}. \quad (4.7)$$

The H beam generally shows lower contrast, since the numbers of t and r are unequal, but higher intensity, because there is one possible path, where only one reflection takes place.

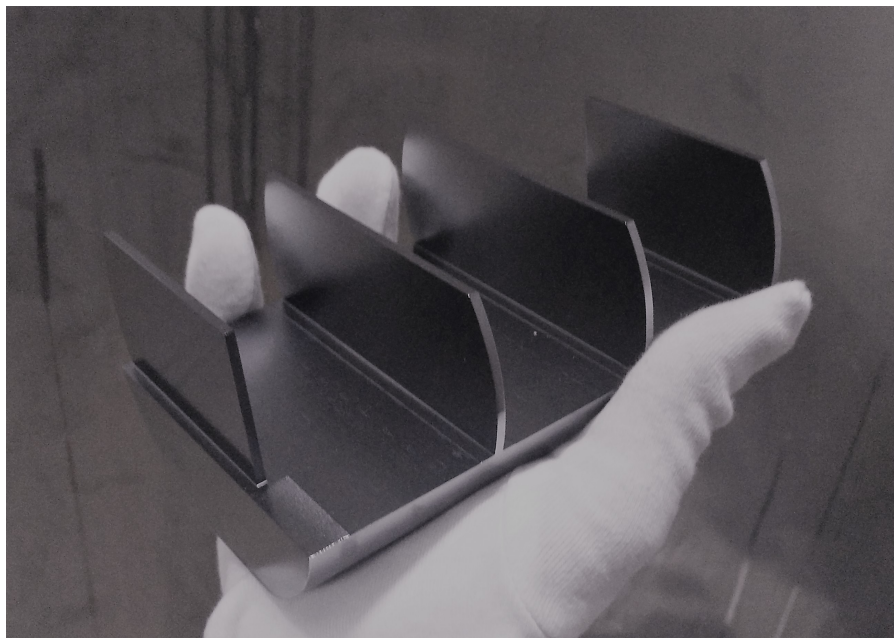


Figure 4.2: Photograph of the four plate interferometer.

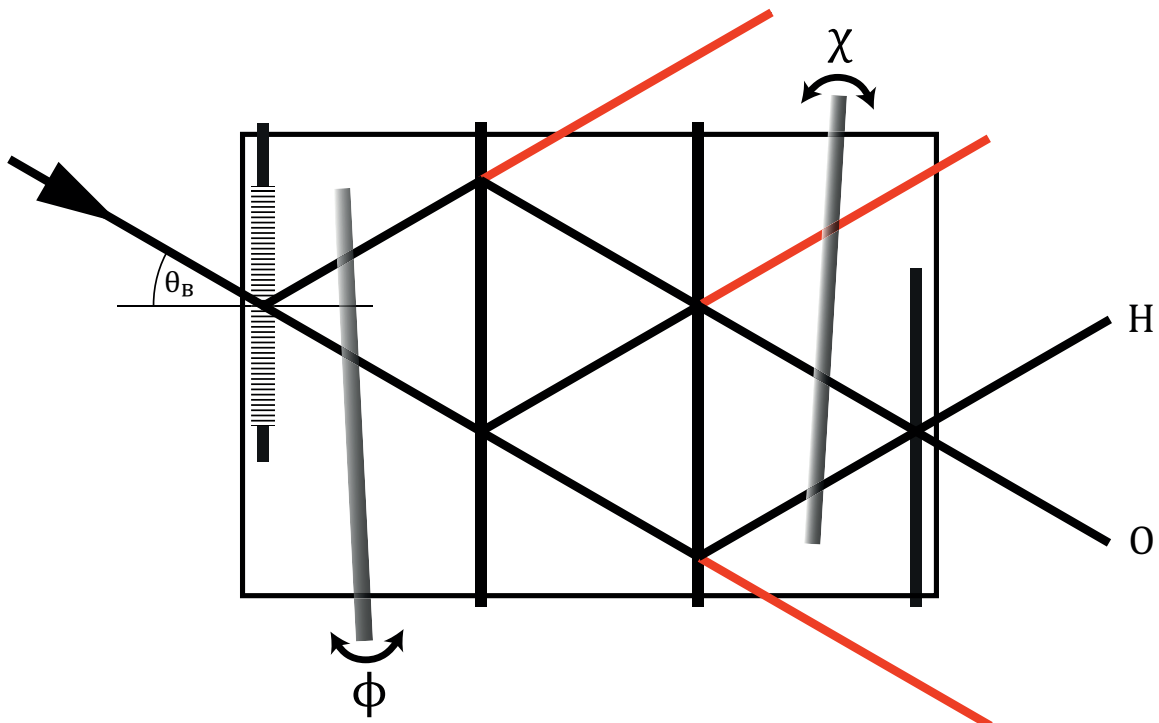


Figure 4.3: Topview of the four plate interferometer with neutron beams and phase shifter plates shown. Bragg plane orientation depicted at the first plate. Red beams are not needed for the experiment.

4.4 Polarizing Magnets

Before entering the interferometer, the neutron beam passes through the gaps of two permanent magnetic yokes, as is depicted in fig. 4.4. The magnetic field inside the gaps is shaped like a prism. Analogous to the optical case, the neutron beam is refracted upon entry and exit of the field region. Since the potential energy of the neutrons in the magnetic field is exactly opposite for $|\uparrow_z\rangle$ and $|\downarrow_z\rangle$, the beam splits into two sub beams containing only one spin state. The angle difference of the two sub beams is of the order of arcseconds, but this is large enough that only one beam fulfills the Bragg condition, whereas the other does not. This way the polarizing magnets prepare the neutrons in the desired spin state $|\uparrow_z\rangle$.

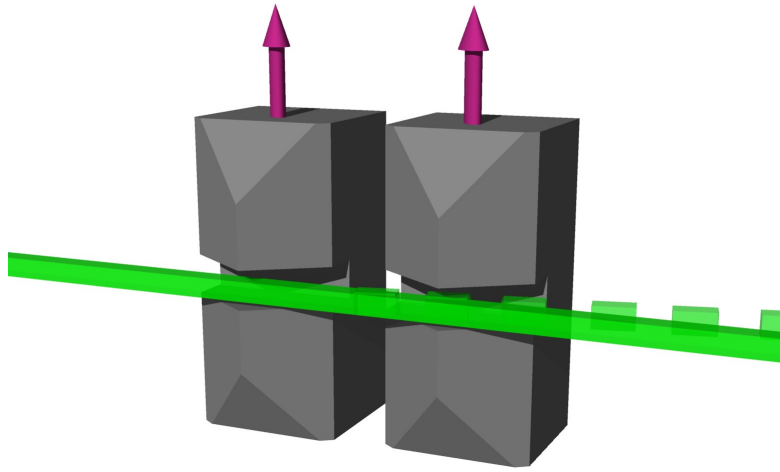


Figure 4.4: Artistic depiction of the polarizing magnets. Neutron beam in green, deflected beam with $|\downarrow_z\rangle$ neutrons dashed. Magnetic field direction indicated by the red arrows.

4.5 Supermirror

The supermirror consists of a multi-layered structure made of two materials with a different coherent scattering length, depicted in fig. 4.5. At every boundary surface between two layers one part of the incoming neutron beam is reflected and the other transmitted. If the optical path difference between two reflected sub beams is a multiple of the wavelength λ , constructive interference occurs. This way, the supermirror acts as an artificial crystal structure. If the thickness of the neighboring layers changes slightly from layer to layer, this condition is weakened, so that it is fulfilled by a variety of incoming neutron wavelengths. If now one of the materials is magnetic and the other non-magnetic, the magnetic scattering

length has to be taken into account in addition to the nuclear scattering length. This way the overall scattering length of the two materials becomes sensitive to the

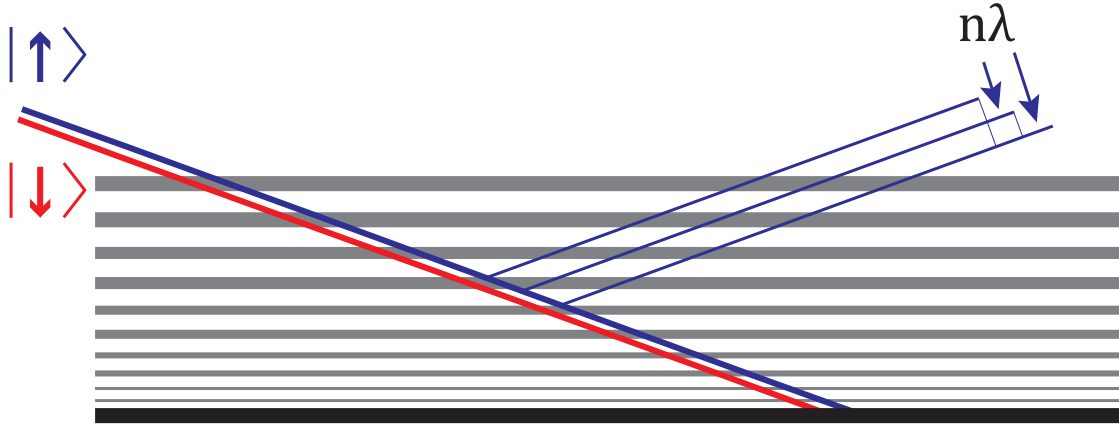


Figure 4.5: Schematic depiction of the supermirror analyzer.

incoming neutron spin direction. A situation can arise, where the scattering length is the same for $|\downarrow_z\rangle$, so that the spins effectively see only one material and become transmitted onto an absorber on the bottom of the multi-layered structure. For $|\uparrow_z\rangle$ the two materials have a different scattering length and constructive interference occurs for the reflected beam. In the experiment the supermirror is used as an analyzer, allowing only $|\uparrow_z\rangle$ to be transmitted into the detector.

4.6 Guide Field

The guide field is produced by two rectangular Helmholtz coils that are placed above and below the interferometer as is depicted in fig. 4.6. It is needed in order to provide a quantization axis for the spin and avoid depolarization. The guide field is connected to a DC power supply and is kept on a constant temperature using cooling water in order to avoid thermal disturbances of the interferometer due to the heat produced by the current. The guide field should be larger in magnitude than the oscillating field produced by the EM-coils in order to avoid a zero field crossing, which causes depolarization. In the experiment a guide field strength of 2 mT was used.

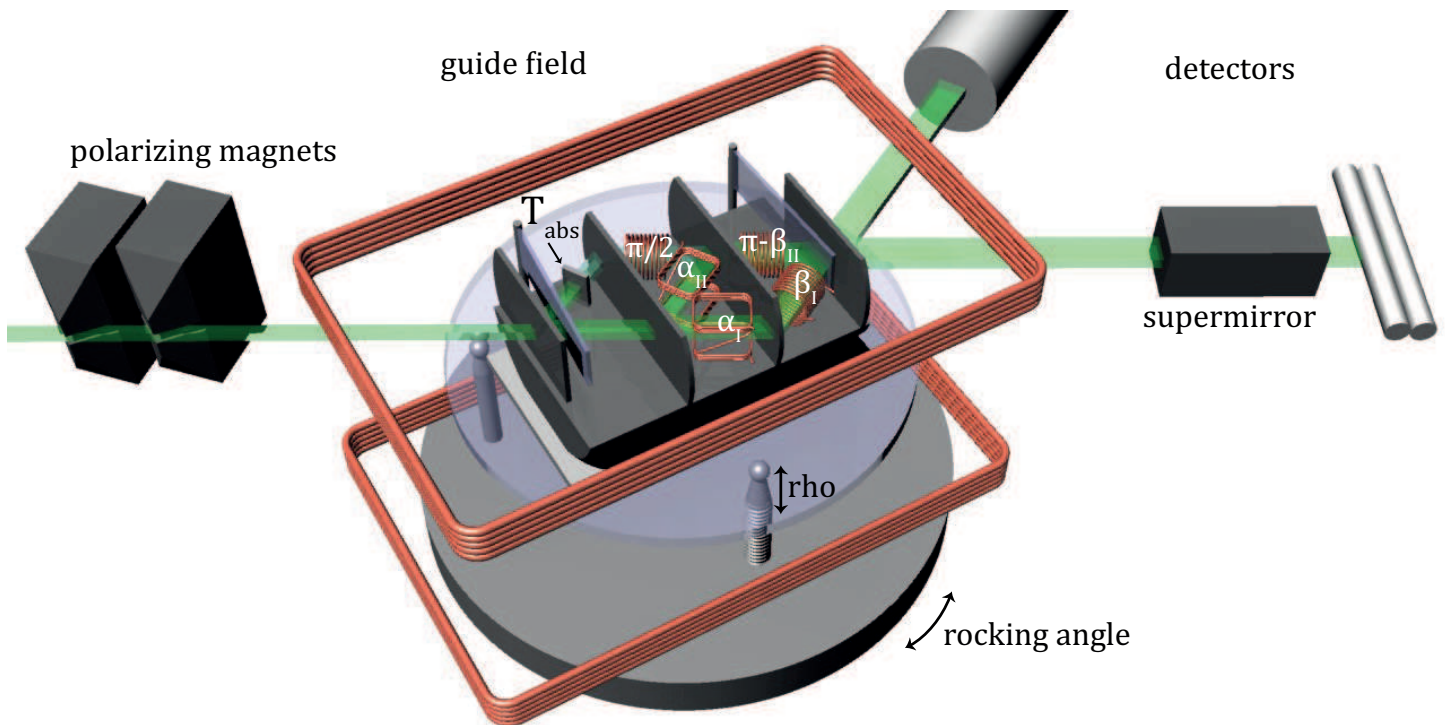


Figure 4.6: Artistic rendering of the whole experimental setup.

4.7 Optical Bench

The experiment is located inside a radiation shielded chamber, where the neutron flux can only be turned on from the outside. The chamber contains a smaller temperature controlled room inside which the so called optical bench is located. It is a steel construction that suspends a table, on which the interferometer is placed, from above by three heavy springs in order to separate the interferometric setup from outside vibrational influence. The interferometer rests upon a plastic slab lying on a glass plate that is centered on a rotational axis as is depicted in fig. 4.6. The rotation is controllable with a motor stage in coarse mode and can be fine tuned using a piezo. This enables to record the so called rocking curve, a graph of the intensity against the rocking angle. The rocking angle can be controlled with a precision in the order of 10^{-4} degrees. For the perfect alignment of the crystal planes with respect to the neutron beam, it is necessary to control the tilt of the interferometer around another axis perpendicular to the rocking axis. This is the so called rho-axis, it tilts the glass plate by lowering or raising it on one side, where it rests upon rod with threads. This motion is precise up to 0.5×10^{-2}

mm. Not depicted in fig. 4.6 is the aperture in front of the interferometer, which collimates the neutron beam into a rectangular profile of typically 5×5 mm using cadmium sheets and can be positioned automatically in the plane perpendicular to the neutron beam. With the aperture a spot of high intensity of the neutron beam and good contrast of the interferometer can be selected. The height of the spring-suspended table can be varied by adding or subtracting weights from the table.

4.8 Spin-Manipulation Assembly

A critical optical element of the experiment is the spin-manipulation assembly (SMA), a water tight container for all the coils influencing different sub beams inside the interferometer. It was designed using the CAD software Rhinoceros (see fig. 4.7) and is put together from 3d-printed parts made out of ABS plastic and coils wound from lacquer coated copper wire. It has holes for the neutron beam to pass through unobstructed and can be held on constant temperature using cooling water that enters and exits the SMA through four nozzles on the top (see fig. 4.8). The copper wires are led through channels in the plastic parts that are designed to maximize the sealing surface. When the different parts of the SMA are assembled contact surfaces are moistened with acetone, in which the ABS plastic is soluble. This way the parts are welded together creating a water-tight seal.

The three RF-coils are wound around rectangular tubes above and below which small Helmholtz coils are placed that produce a local z-field. This makes it possible to adapt to local deviations of the big guide field in order to fulfill the resonant condition for the spin flip. The two EM-coils are wound around scaffold parts glued on the top and bottom of the rectangular beam tubes. Upon assembly, the five coils are placed onto grooves in the bottom of the two vessel forms, so that they stay in the right position. After the assembly, when the acetone has evaporated, the holes for the beams are cut out and smoothed using a file.

At each interferometer plate the neutron beam profile is broadened which can be modeled with a simple geometric approximation as can be seen in fig. 4.9. This effect is accounted for by making the wholes for the neutrons in the SMA subsequently wider down the beam. The SMA is mounted on a goniometer that makes it possible to control its orientation. The goniometer is connected to a robotic arm that can be rotated around the z-axis and moved in all three directions of space automatically with a precision of 10^{-5} m. The indium absorber T_{abs} is connected to the SMA, as are three optional $\sim 100\%$ cadmium absorbers, that can be put in and out of the three holes in the front part of the SMA, which makes it possible to access the three beams separately.

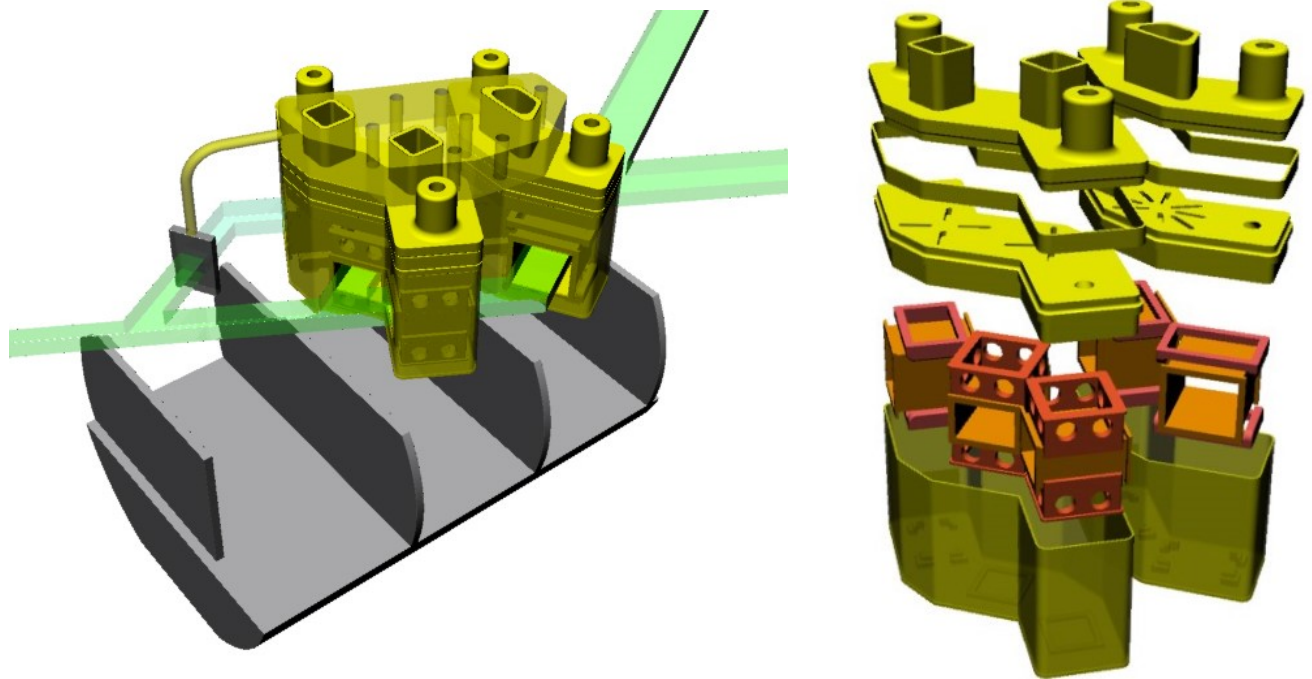


Figure 4.7: Rendering of the 3d-printed parts for the SMA.

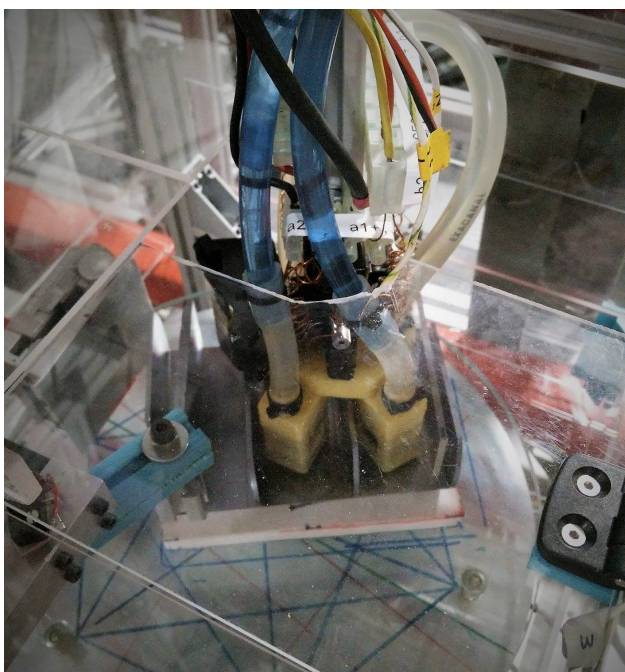


Figure 4.8: Photograph of the SMA inside the interferometer.

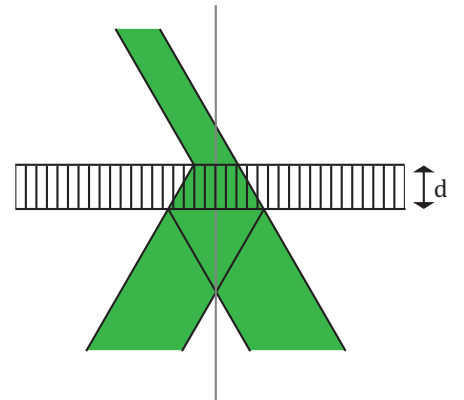


Figure 4.9: Beam broadening at an interferometer plate with thickness d .

4.8.1 Coil Assembly Dimensions

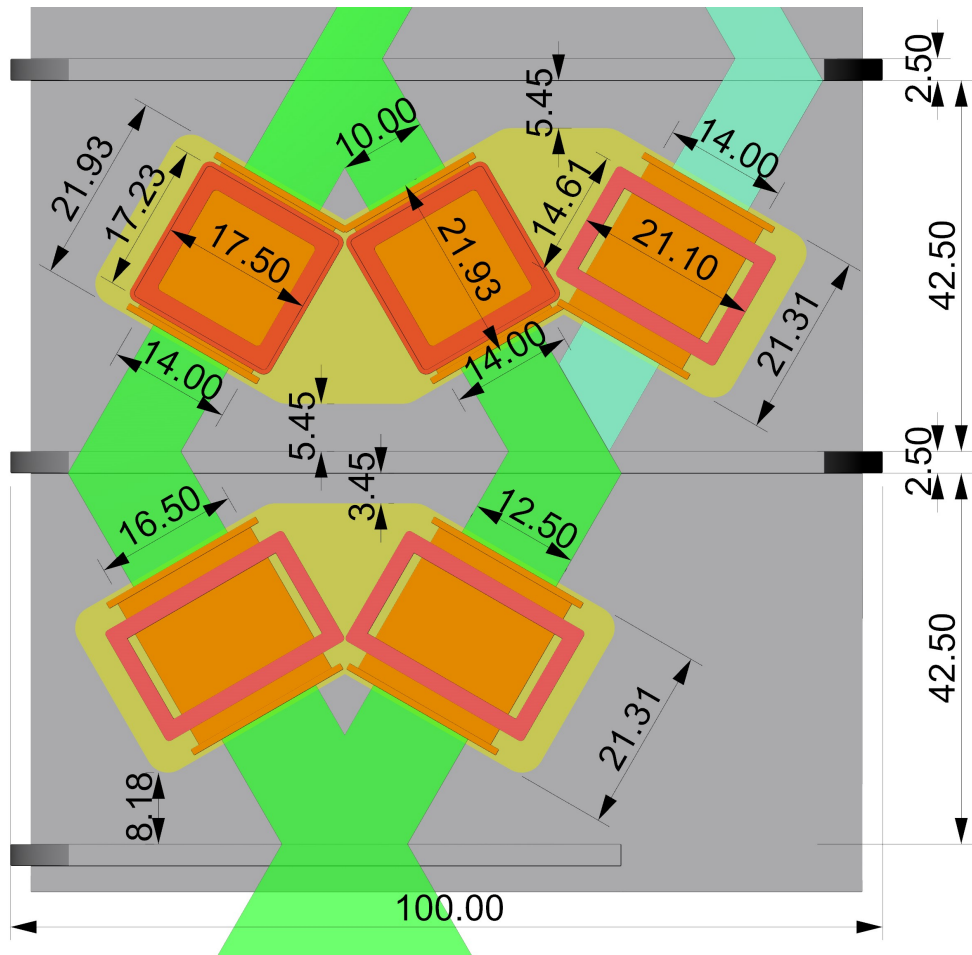


Figure 4.10: Topview section of the SMA inside the interferometer with dimensions in mm. Neutron beam cross section before the interferometer is 5×5 mm.

The SMA was designed to accommodate an incoming neutron beam with a cross section of 5×5 mm. As already mentioned, at every interferometer plate, the neutron beam is subject to a broadening, which is accounted for by making the rectangular holes in the SMA larger for the two RF-flippers downstream of the beam. The broadening only takes place in the plane where the beam separation occurs. In the perpendicular direction the beam always keeps a height of 5 mm, when the overall beam divergence of typically 1° is neglected. At every hole, the inner cross section of the rectangular tubes is made to keep a distance of at least 2 mm to the neutron beam. This is needed in order to account for imperfections in assembling the parts and to have some tolerance when positioning the SMA in the

experiment. The vessel forms and rectangular tubes of the SMA were printed with a wall thickness of 0.55 mm and only one perimeter of filament, a setting found best to work for making the parts watertight. The neutron beam is centered at a distance of 13.5 mm from the bottom of the SMA. Holes for the RF-flippers have a height of 14 mm and for the EM-coils a height of only 9 mm, which makes it easier to produce the strong oscillating magnetic z-fields necessary for the experiment to work. The rectangular scaffold parts for the EM-coils have round holes in order to allow the cooling water to flow more freely. The design of the RF-flippers is very similar to the ones used in other experimental works carried out by Denkmayr et al. [25] and Geppert et al.[26], which were also made with 3d-printing. Another critical point which was accounted for is the minimum distance of about 8 mm needed in order to fit the phase shifter plate χ between SMA and the fourth interferometer plate.

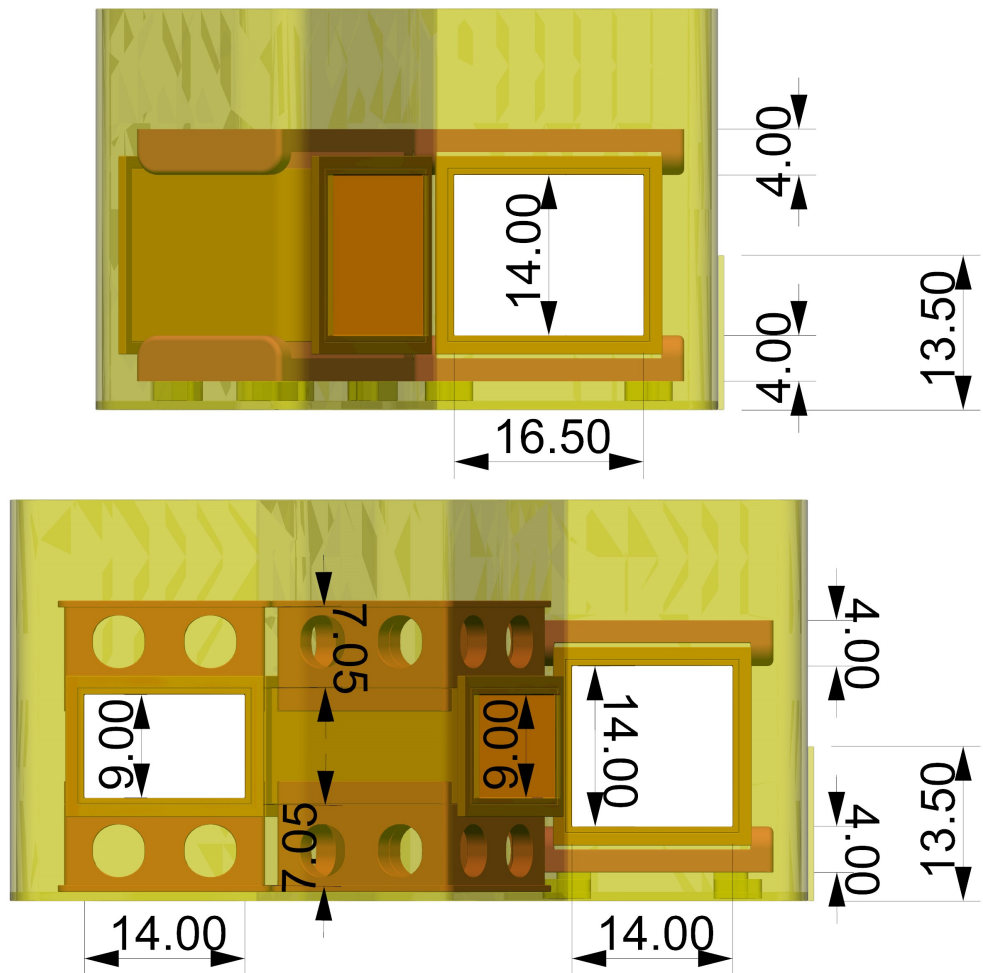


Figure 4.11: Sideview of the two SMA parts, dimensions in mm.

4.8.2 EM-Coil Field Simulation

A simulation of the magnetic field produced by the EM-coil was conducted using Mathematica. The EM-coils are modeled as two surface currents along the outer walls of a cuboid with a square base of side length 17.5 mm and height 7 mm that keep a distance of 10.5 mm (see fig. 4.12). An analytic expression for the field produced by this configuration is evaluated numerically. The result suggests that the field between the two coils, inside the volume of the neutron beam, is homogeneously pointing in the z-direction and stray fields are very small in magnitude ($\max(B_{x,y}/B_z) = 0.013$). The coils are modeled to have 15 windings around each cuboid with a current of 2 A. Figure 4.13 shows a plot of the z-field magnitude along the neutron trajectory.

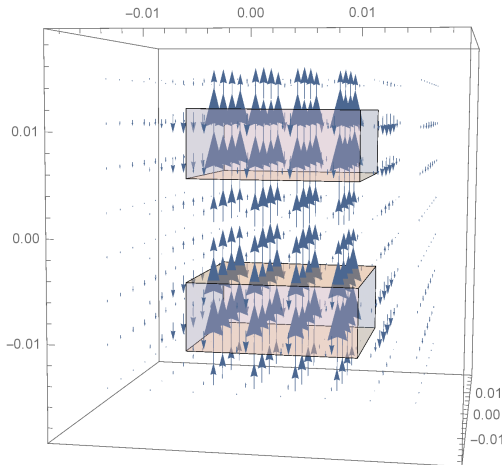


Figure 4.12: 3d vector plot of the magnetic field produced by the EM-coil. Dimensions in m. Current carrying wires modeled as outer surfaces of the two cuboids.

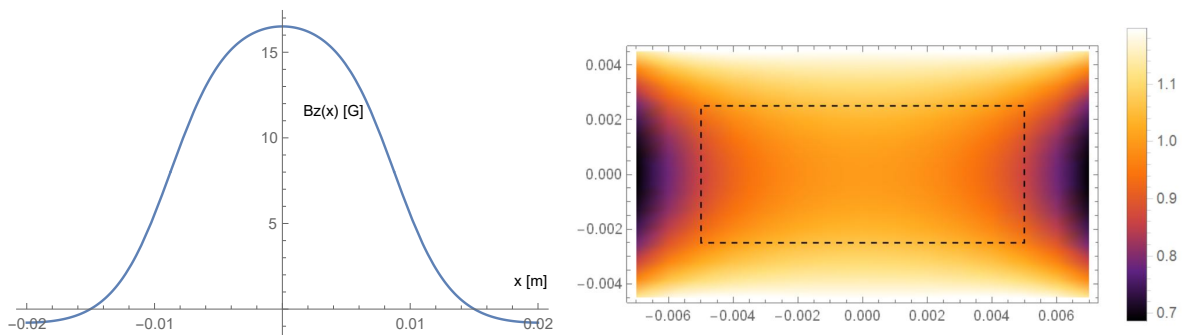


Figure 4.13: Left: Plot of $B_z(x, 0, 0)$ of the magnetic field produced by the EM-coil along a line in the direction of neutron flight through the center of the hole for the neutron beam. Right: Heatmap of $\int dx B_z(x, y, z) / \int dx B_z(x, 0, 0)$ over the cross section of the neutron beam normalized to the center (dashed rectangle shows expected beam profile at the location of the EM-coils when the incoming beam is 5×5 mm).

4.9 Measurement Control and Data Acquisition

The experimental setup is located inside a radiation shielded chamber and is remotely controlled from a small room about 5 m away. All in and outputs are connected to a computer running a Labview program responsible for the experiment control. Most measurements, e.g. preparatory parameter scans, are done by varying one parameter, say the rocking angle, and then registering neutron counts for a fixed duration, thus recording a scan. A typical application is to record an interferogram, i.e. a scan of one phase shifter plate. By varying the aperture position in the plane perpendicular to the neutron beam it is possible to record a 2d-map of the interferometer contrast, measuring an interferogram at each position. Motor axes that can be varied automatically include the rocking angle, the rho-axis, horizontal supermirror position, two phase shifters, sample holder robot (holds the SMA) rotation and position, monochromator orientation, and H detector position. It is also possible to set constant and alternating currents and voltages by addressing different power supplies and function generators, which in turn are connected to AC amplifiers, via automated GPIB commands. This is needed in order to control the RF-flippers, EM-coils and guide-field.

Another possible mode of data acquisition is to perform a time-dependent measurement. For this purpose a field-programmable gate-array (FPGA) is used. The FPGA runs a continuous-cycle with a given loop-time and records the occurrence of neutron-counting events, which are sorted into bins of constant width, creating a histogram. This way it is possible to measure an oscillating intensity signal as can be produced, when an EM-coil is present in one arm of the interferometer. As already mentioned above for this purpose the 1/4" detectors are used, being placed with their axis perpendicular to the neutron beam, since they offer a better time resolution. In order to have the oscillating magnetic fields of the EM-coils running synchronous to the FPGA loop, the two function-generators producing the sinusoidal control voltages are operating in burst-mode. They are started at the same instant by a burst signal, a sharp voltage pulse, and produce a fixed number of sine periods, such that an integer multiple of this period is equal to the loop time. The RF-coils are not time-locked to the FPGA-loop and operate in continuous mode.

It should be noted that neutron counting events obey Poissonian statistics, where a recorded countrate of N neutrons per second is associated with an error of \sqrt{N} . By measuring for a longer time, therefore registering more neutron counts, the relative error in the count rate decreases.

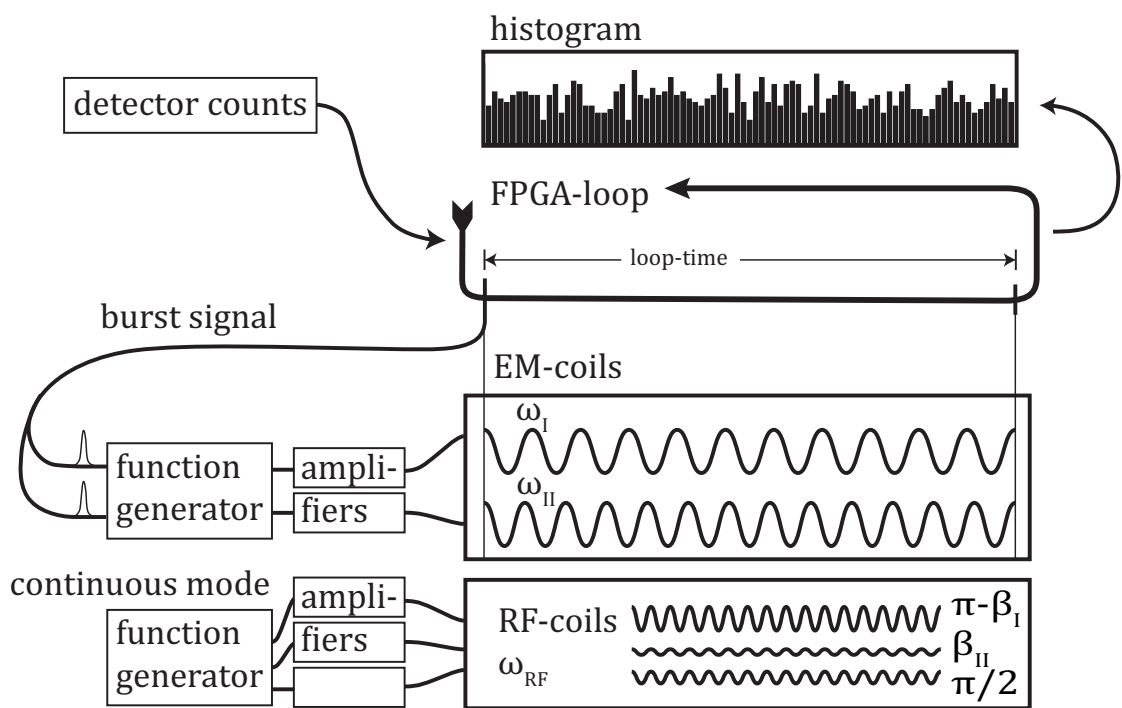


Figure 4.14: Schematic depiction of the time-dependent measurement process and generation of oscillating coil-currents.

5 Measurement

This chapter covers, how the experiment was set up, starting from the right placement of the interferometer and finding the Bragg peak, to measuring interferograms and adjusting the 1/4" detectors, and different coils, RF and EM alike. All preparatory measurements are presentend and in the end we arrive at the starting point for the final measurement.

5.1 Search of the Interferometer Sweet Spot

From the previous experiment in the last reactor cycle by my colleagues Bülent Demirel and Armin Danner, the monochromator crystal and polarizing magnets are already set in a good position, which is left unchanged for the current experiment. As the first step, the big O detector is placed in the direct beam. The aperture, which is positioned after the polarizing magnets and in front of the IFM, is set to 5×5 mm and scanned horizontally and vertically to find the position of highest neutron intensity. Then the interferometer is placed onto the rotary table on top of a plastic slab. The O detector is moved so that it catches the neutron beam reflected inside the interferometer, in parallel to the original beam.

As a next step, the rocking angle is varied in coarse mode (with a motor) to find the peak position, where the incoming neutron beam fulfills the Bragg condition for the interferometer. From this position the rocking angle can be varied using a piezo, in order to record a rocking curve (fig. 5.1). The rocking curve shows two Gaussian peaks, essentially the beams with $|\uparrow_z\rangle$ and $|\downarrow_z\rangle$ neutrons separated by the polarizing magnets. Later on, when the spin-analyzer is put in place in front of the O detector, the right peak of the curve for the O beam vanishes (only $|\uparrow_z\rangle$ neutrons of the left peak reach the detector, see fig. 5.3).

Now the rho-axis, which controls the tilt of the interferometer around its longer axis is adjusted. For this purpose, the outer beams between second and fourth interferometer plate are blocked with a folded cadmium sheet, so that only the middle beam can pass through to the detectors. The cadmium absorbers simply rest on the interferometer between the plates. This setup makes the interferometer more sensitive for the following rho-axis scan. The reason is, that the middle beam gets reflected three times before it hits the H detector and only reflection, not transmission, is dependent on the precise alignment of the Bragg planes. The sum

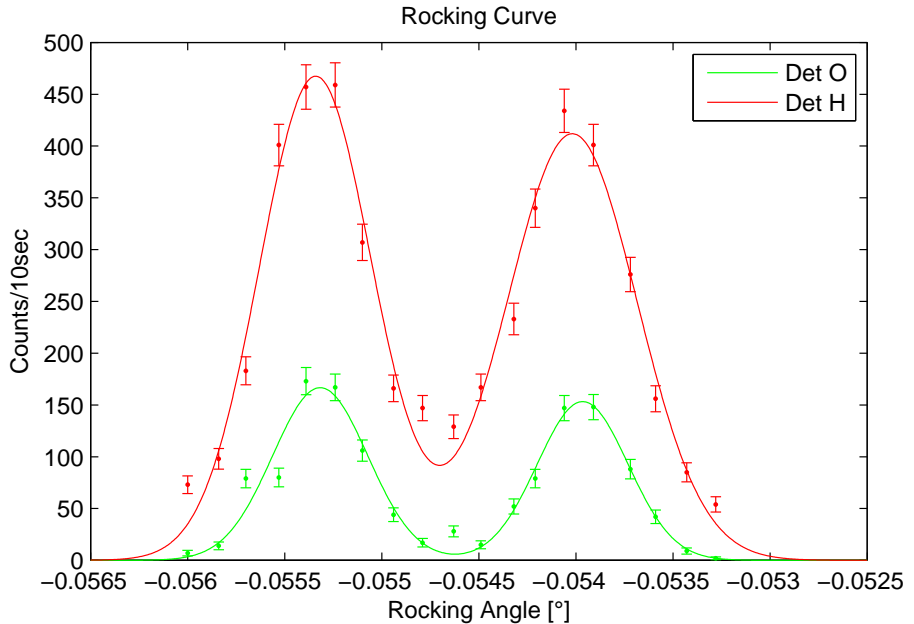


Figure 5.1: Rocking curve of the empty interferometer (without supermirror, all three beams free, measured with big O detector). Fit curves are a sum of two Gaussians of the form $y_0 + Ae^{-(\frac{x-x_0}{\sigma})^2}$.

of O and H detector counts for the left peak of the rocking curves obtained for different values of rho is fitted with a Gaussian. The FWHM of these fits is then plotted against rho. From this curve the minimum, i.e. the optimum rho value, is determined from another Gaussian fit (fig. 5.2).

For the following measurements, the rocking angle is always set to the peak position of the rocking curve, which can be done automatically in the measurement software.

Next, interferograms are recorded by scanning the rotation angle of phase shifter χ . The contrast and intensity of the interferograms are obtained from sinusoidal fits (contrast $C = B/A$ from fit function $A + B \cos(f\chi + D)$, intensity B , see figs. 5.4 and 5.5). By varying the aperture position horizontally and vertically in the plane perpendicular to the neutron beam, taking an interferogram at each step, a 2d-map of contrast and intensity is recorded (fig. 5.6). The intensity is not homogeneous over this 2d-map, because the beam profile in front of the interferometer is influenced by the placement of the polarizing magnets. Also the contrast shows variation, because the interferometer plates have a certain roughness on the

surface due to manufacturing.

The aperture is now set to a position of high contrast and intensity for the O beam. After that, the supermirror is put in place in front of the O detector and scanned horizontally with linear motors on its front and back end to get good alignment with the neutron beam. The raster scan is repeated (fig. 5.7). Again the aperture is set to the new optimum position. The contrast in the O beam is now higher than in the previous raster scan, which is due to the neutron beam being free of incoherent $|\downarrow_z\rangle$ -components after the supermirror.

Finally, the SMA is introduced into the interferometer. To find the optimum position for the SMA, first the middle hole was blocked with a cadmium plate and the SMA was moved in parallel to the interferometer plates while measuring the count rate. Then the two outer beams were blocked and the scan was repeated. The maxima of the two scans were differing only by fractions of a mm, so the SMA was positioned to a value in between. Then the SMA was scanned vertically and placed at the maximum count rate position. At last a final raster scan was carried out (fig. 5.8).

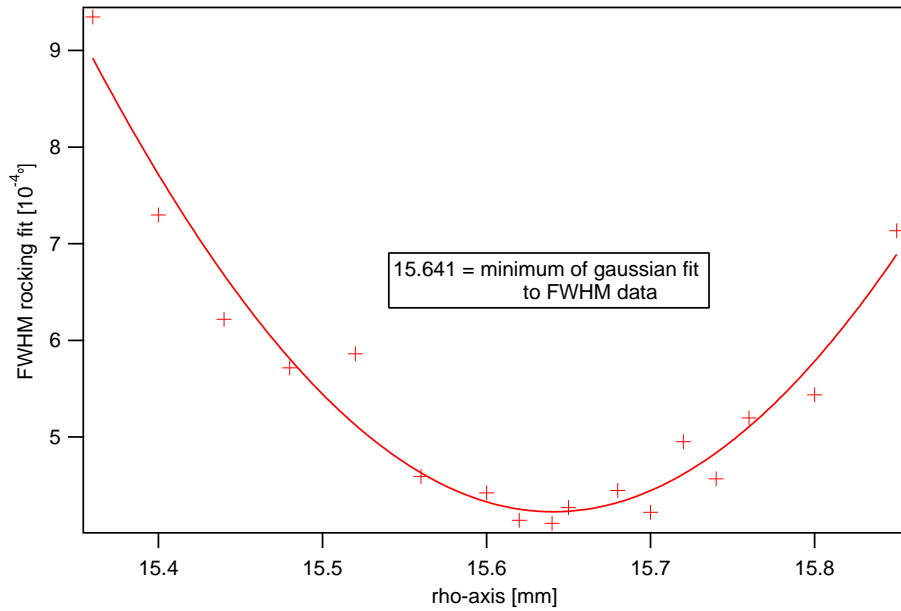


Figure 5.2: Rho-axis scan: FWHM obtained from the gauss fitted rocking curves of the sum of both O and H detector intensity against rho-axis. The left peak of the rocking curve is used for the data-fit.

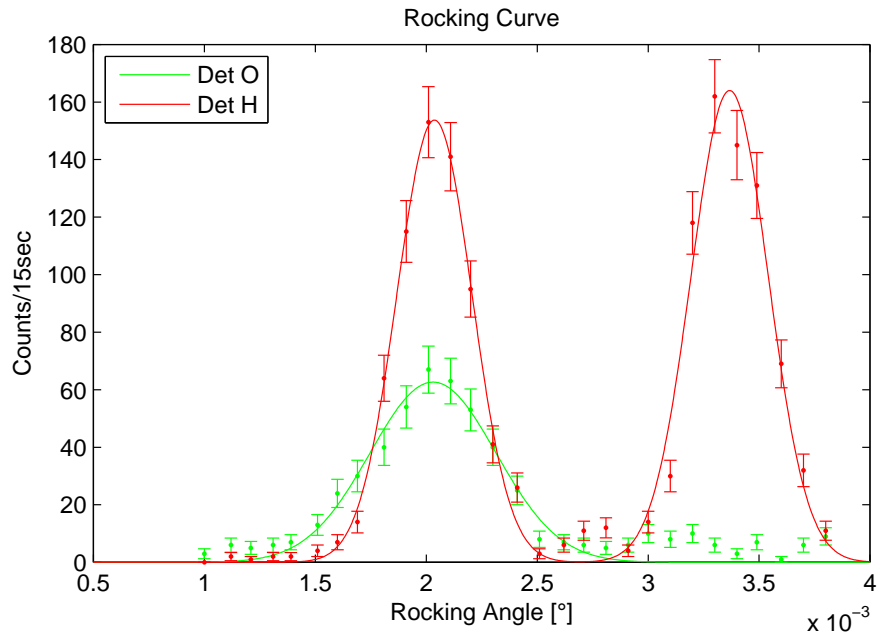


Figure 5.3: Rocking curve with supermirror in place, two outer beams blocked with Cd sheet, measured with small O+Aux detector (higher noise).

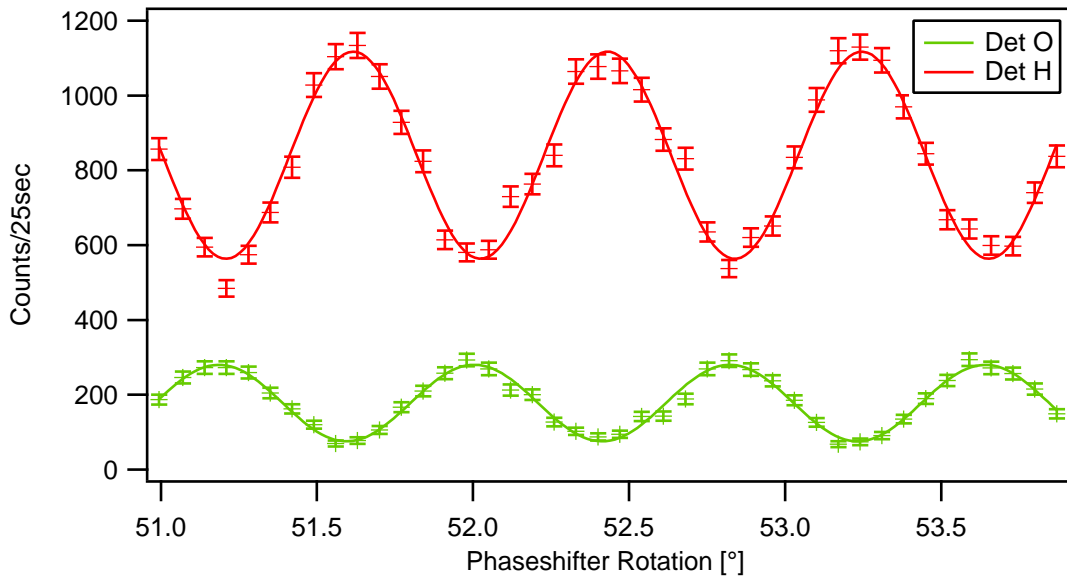


Figure 5.4: Interferogram recorded with phase shifter χ , middle beam blocked. The two curves are in anti-phase because by varying χ , the intensity becomes shifted between O and H beam.

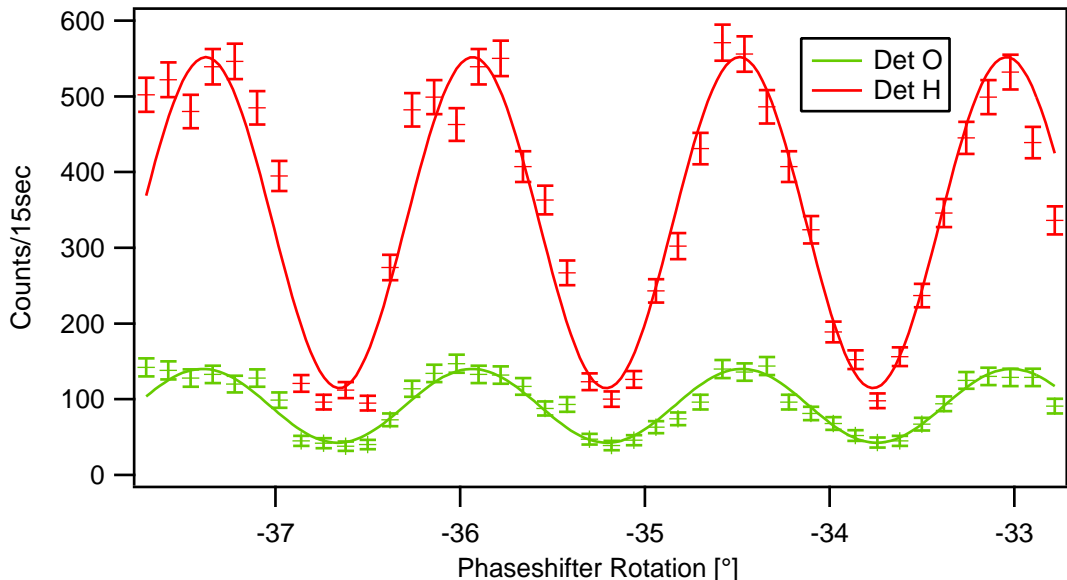


Figure 5.5: Interferogram recorded with phase shifter ϕ , reference beam blocked. Both curves are in phase, because the phase shifter effects the first interferometer loop, and when the intensity is low, the beam, that in turn has a high intensity, leaves the interferometer without hitting a detector.

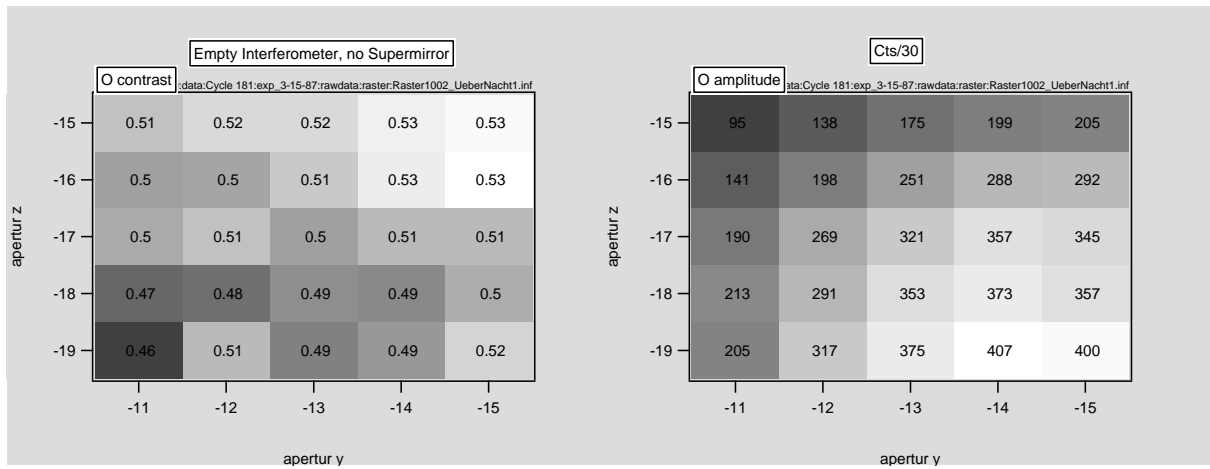


Figure 5.6: Contrast and amplitude of the O beam obtained from a raster scan of the empty interferometer, interferogram recorded with phase shifter χ .

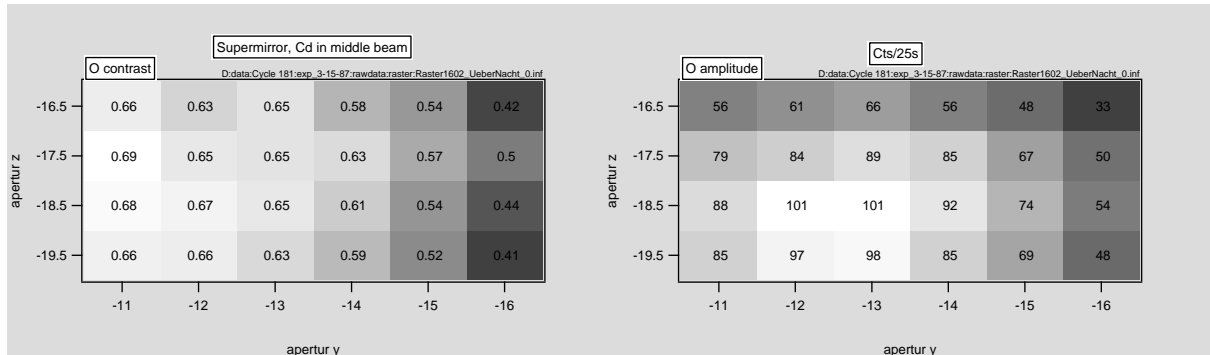


Figure 5.7: Raster scan with supermirror in place, middle beam blocked with cadmium absorber, interferogram recorded with phase shifter χ .

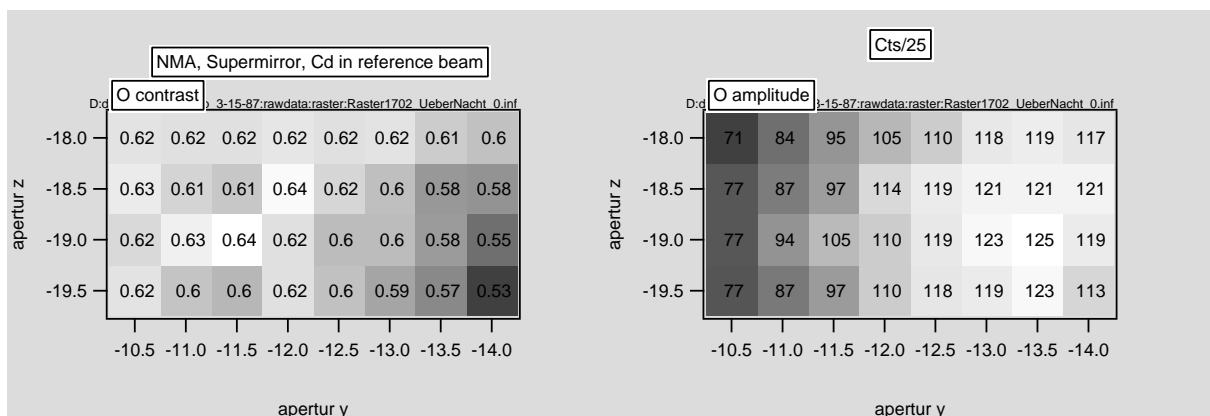


Figure 5.8: Raster scan with SMA and supermirror in place, reference beam blocked with cadmium absorber, interferogram recorded with phase shifter χ .

5.2 Adjustment of the RF-Flippers

To adjust the RF-flippers β_I , β_{II} and $\pi/2$ the corresponding beams are isolated, meaning the other beams are blocked with a 1mm thick cadmium plates with $\sim 100\%$ absorption. Then the guide-field is adjusted, so that it fulfills the approximate resonance condition $B[\text{G}] \sim \frac{1}{3}f[\text{kHz}]$. The frequency used for all RF-flippers is 60 kHz.

The coils are connected to an amplifier in series together with a capacitance. The capacitance is chosen, so that the LC-circuit has resonance frequency around the desired 60 kHz. For this purpose, the inductance of the coils is determined with an electronic RLC-meter. The corresponding capacitance can be calculated from the formula

$$f_0 = \frac{1}{2\pi\sqrt{LC}}. \quad (5.1)$$

The RF-currents from the amplifier are driven via a function generator producing a sinusoidal voltage oscillation. First, an amplitude scan of the function generator voltage is carried out. This amplitude is proportional to the oscillating field strength B_1 and therefore to the spin-rotation angle. For a spin rotation around an axis perpendicular to the spin-analysis direction a sinusoidal behavior of the intensity against the rotation angle is expected. The measured count rates from the amplitude scan are fitted with a sine wave and the minimum is chosen for the subsequent scan over the guide field current. This scan serves to find the optimal guide field strength in order to fulfill the resonance condition of the RF-flipper. For the $\pi/2$ -flipper, the big guide field is varied (fig. 5.9 right). A dip in the count rate is expected, when the resonance condition is fulfilled. The measured curve is fitted with a Gaussian and the minimum is chosen as a final value for the guide field strength. Then, the amplitude of the function generator is scanned again to arrive at the minimum count rate, from which the driving voltage corresponding to a $\pi/2$ -flip is calculated (fig. 5.9 left).

This process is repeated for the other coils, but now the local guide-fields are varied (see figs. 5.10 and 5.11). Since all RF-flippers operate at the same frequency this is not strictly necessary, but the local guide field coils exist in order to account for possible deviations of the big guide field. The currents for the minimum count rate of the scans are very near zero, signifying that the big guide field has good homogeneity, so the local guide fields are left turned off.

The final amplitudes for the RF-flippers in the experiment are calculated from the sinusoidal fits by taking the maximum (0 amplitude), plus 15° from the fitted period when β_{II} is turned on for the RF-flipper in path II, the minimum (π -flip), minus 15° when β_I is turned on for path I, and the minimum minus 90° for the $\pi/2$ -flipper. The flip-ratios are calculated by dividing the counts for no flip through the counts for a π -flip.

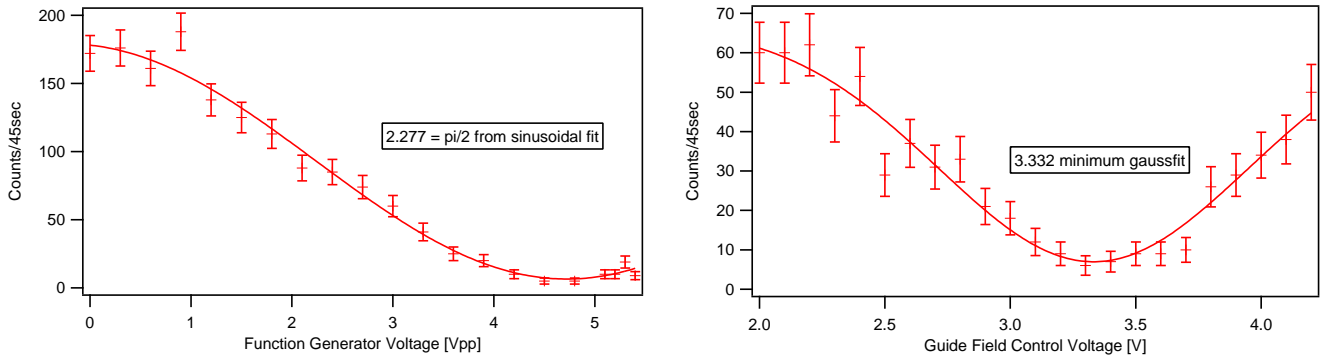


Figure 5.9: Adjustment of the $\pi/2$ -flipper. Left: Amplitude scan of the RF-field. Right: Scan of the big guide field magnitude when the RF-field strength is set to a π -flip. Flipratio: 27.0

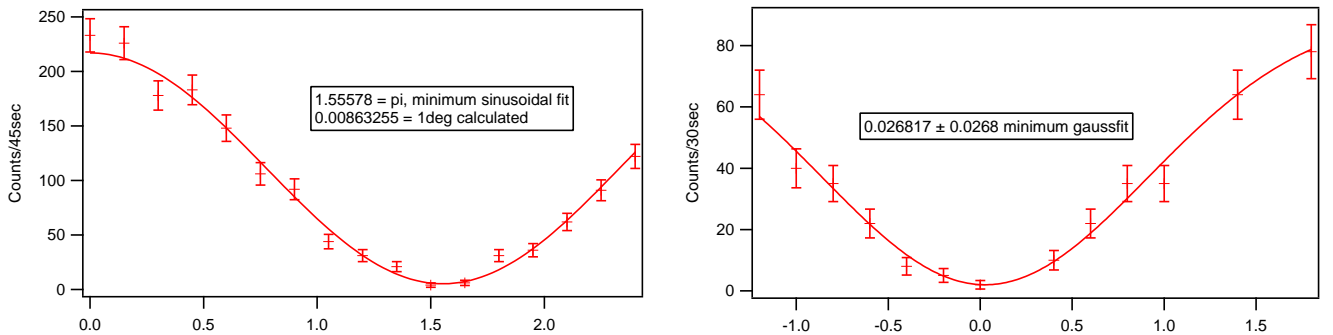


Figure 5.10: Adjustment of RF-flipper β_I . Left: RF-amplitude scan. Right: Scan of local guide field when the RF-coil does a π -flip. Flipratio: 44.3

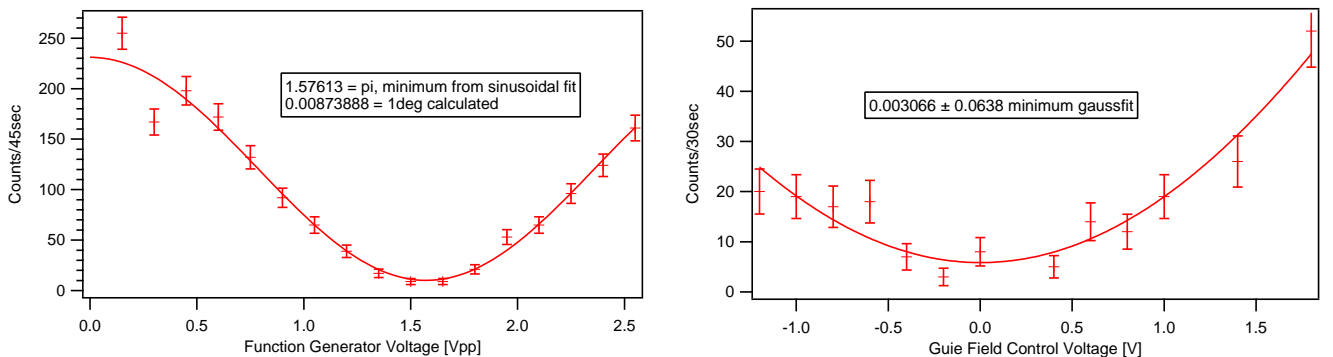


Figure 5.11: Adjustment of RF-flipper β_{II} . Left: RF-amplitude scan. Right: Scan of local guide field when the RF-coil does a π -flip. Flipratio: 26.6

5.3 Setting up the Detectors for Time-Dependent Measurements

For setting up the two 1/4" detector tubes, they were placed at the neutron guide exit before the polarizing magnets in the direct beam, one after the other. As already mentioned above, the small width of ~ 7 mm offers for a better time resolution, since the time a neutron spends inside the detector volume is limited. The detectors are each connected to an electronic device that works as an amplifier and signal shaper in one. There were two different devices, one with a specified maximum count rate of 50 kHz, the other of 150 kHz. Both values are more than enough to cover the frequencies of ~ 25 kHz used for the EM-coils with count rates on the order of 10 counts per second. Each device has two input ports, a DC power supply and a high voltage supply. Outputs are the amplified detector signal and the shaped signal, which consists of logic voltage pulses corresponding to neutron counting events.

First, the amplifier gain is adjusted to factory settings. Then, a measurement of the high voltage supply against the count rate is conducted. The HV is set on top of the small plateau in the graph of fig. 5.12. Next, the amplifier output is connected to a multi-channel-analyzer (MCA). The MCA records a histogram of the signal pulse peak height, sorted into 1024 bins equally distributed in a range of

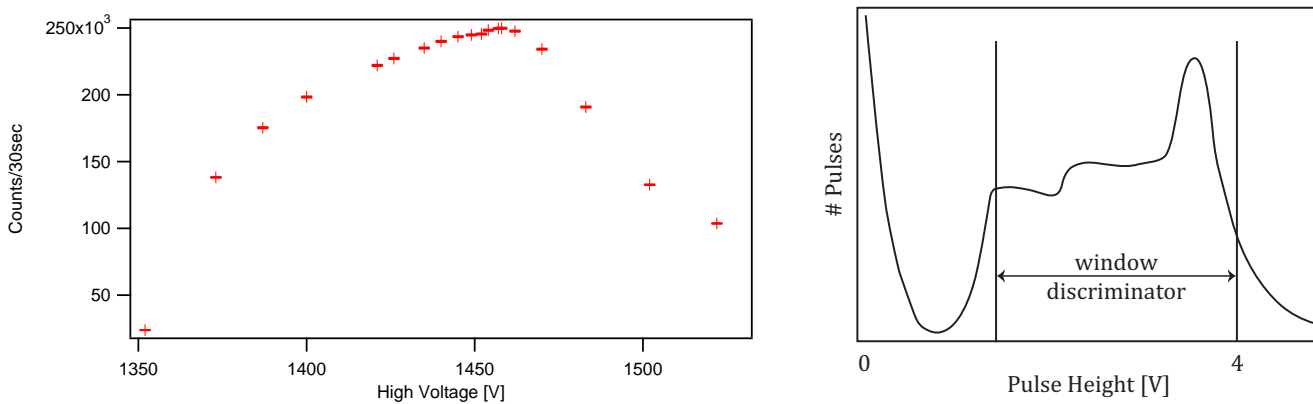


Figure 5.12: Left: Graph of count rate against high voltage supply of one of the small detectors. Right: Illustration of a MCA spectrum. Unfortunately, no screen-shot of the spectrum in the MCA software was taken. Signal inside the window selected by the discriminator from left to right: proton peak, tritium peak, combination of the two. Low voltage flank produced by electronic noise.

0 – 10 V. This spectrum is needed in order to determine the lower cut-off voltage, below which a pulse is ignored. The MCA histogram consists of three peaks, one produced by the lighter decay product of the detector reaction eq. (4.1), namely the proton, the other one by the tritium nucleus, and the third peak is produced by both. The MCA spectrum should contain these peaks inside a region between 0 and 4 V, because the higher cut-off voltage of the amplifier and shaper device is fixed at 4 V. If not, the gain has to be adjusted. The lower cut-off voltage is then set at the edge of the plateau, where the proton peak is located. This prevents electronic noise located in the lower voltage range from polluting the data.

This process was repeated for the second small detector. After both were set up, they were placed inside a pouch of folded cadmium sheet directly at the exit window of the supermirror analyzer, such that their cylindrical axis is perpendicular to the neutron beam, and they lie one after the other in the direction of neutron travel. The cadmium shielding is to block stray neutrons.

At first, measurements of the count rate without neutron flux showed good results of roughly two counts in 120 seconds. Later it was noticed, that this number fluctuates unpredictably and was at times as high as 0.5 per second. The suspected reason for this is a bad connection between the high voltage coaxial cable outer electrode and the detector tubing, which acts as the cathode. This connection is only clamped and should be soldered for future experiments.

For this reason, the detectors can be used in order to make a time-dependent measurement, to find the frequency, with which the count rate oscillates via fast Fourier transformation. For a measurement of neutron intensity over a longer time period, to be comparable to other such measurements, the data obtained with the smaller detectors is not reliable. Such a measurement must be done with the big O detector.

5.4 Adjustment of the Energy Manipulator Coils

To see the effect of the energy manipulation it is essential to have interference with the reference beam. In order to save on measurement time the 30% absorber was removed during the adjustment. For the adjustment of coil α_I , beam II was blocked with a 1mm cadmium beam-stopper and vice versa for α_{II} . All other coils were turned off and the phase shifter angle ϕ was set to $\pi/2$ to maximize the effect on the oscillating intensity. The coils are in series with a capacitance chosen to support resonant frequencies of the circuit at around 20-25 kHz and connected to an amplifier, which is driven by a function generator. The frequencies for the two coils, $\omega_I = 26$ kHz and $\omega_{II} = 22$ kHz, are chosen, because they produce the desired detectable intensity oscillation after unsuccessful tries with 50 kHz beforehand.

Now a time-dependent measurement is carried out, where the logic pulses cor-

responding to neutron counts from detectors O and Aux are fed into an FPGA card, where they are sorted into bins of width $5 \mu\text{s}$ in a repeating sequence with a certain loop time. At the beginning of each loop the FPGA card sends out a burst signal, starting the function generator, which produces an integer number of sine waves with frequencies ω_I and ω_{II} on two channels, such that the loop time is a multiple of the sine periods. The counts from both detectors are registered separately because the time of flight between the detectors, which are placed approximately 1 cm apart, can not be ignored in comparison with the binwidth. Two detectors are used in order to have a higher overall count rate. They are placed one after the other in the direction of neutron flight, because this placement gives the highest overall count rate.

Different amplitudes of the function generator signal are applied and time-dependent measurements are performed. The recorded histograms are analyzed via a fast Fourier transform (FFT) algorithm that calculates amplitude spectra as can be seen in figs. 5.13 and 5.14.

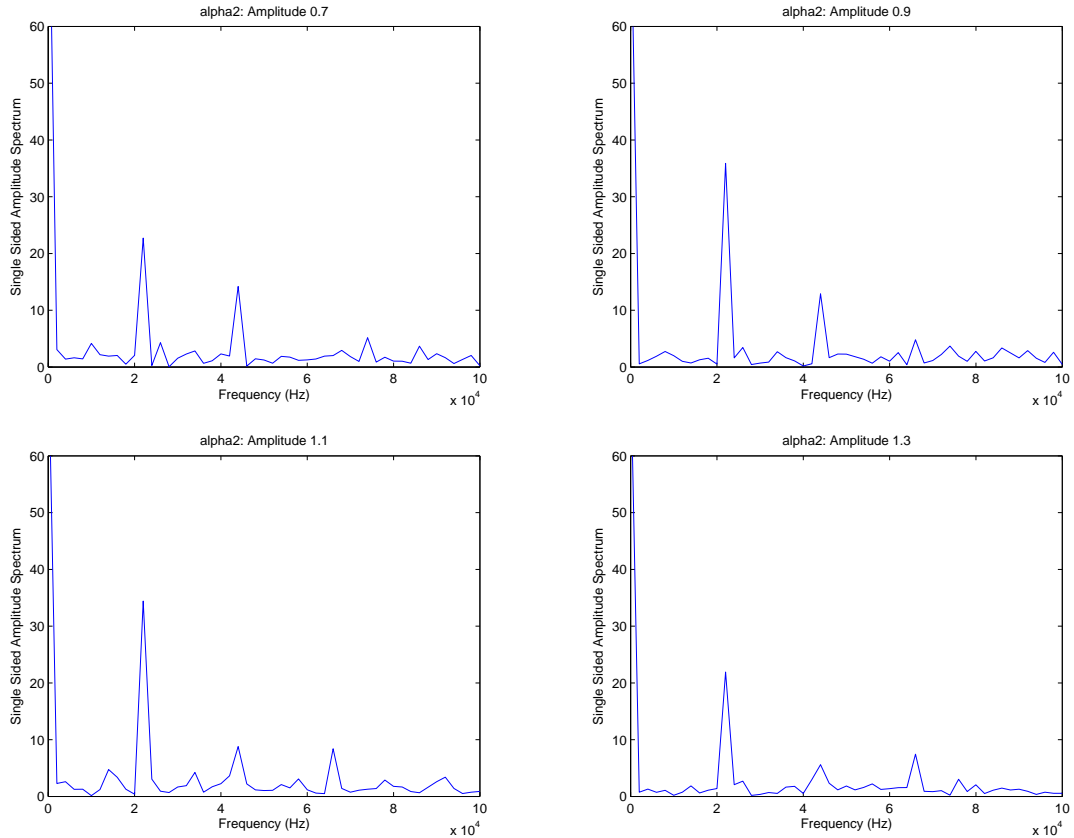


Figure 5.13: Time-dependent measurements for different function generator amplitudes for α_{II} . Measurement time 1200 s, loop time 500 μs , binwidth 5 μs .

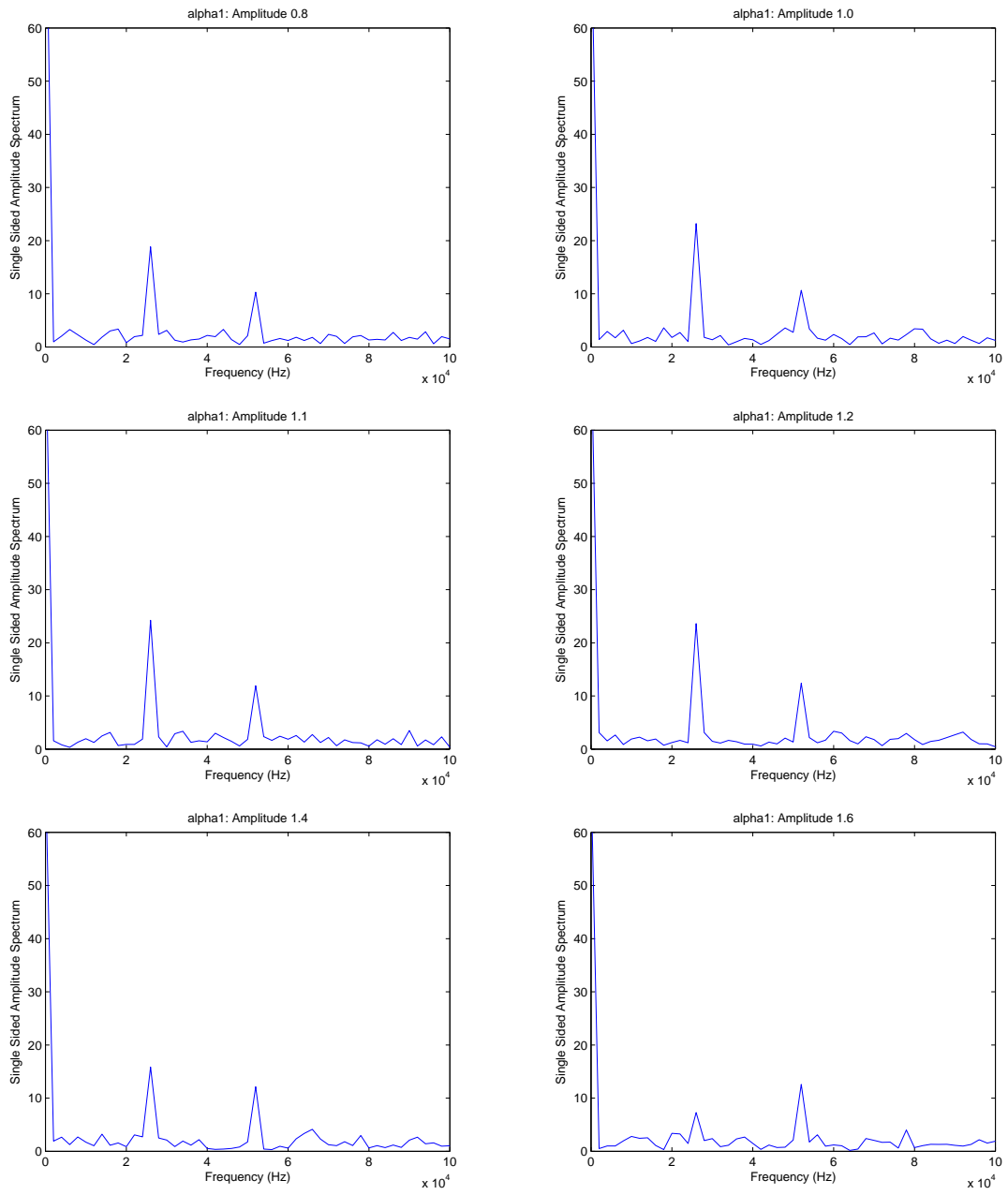


Figure 5.14: Time-dependent measurements for different function generator amplitudes for α_I . Measurement time 1200 s, loop time 500 μ s, binwidth 5 μ s.

What can be seen in the FFT spectra is a dominant peak at zero frequency corresponding to a constant count rate in time, i.e. no photon exchange between neutron and EM-coil. The second peak is located at the operating frequency of the EM-coils, either at 22 kHz or 26 kHz, corresponding to one photon exchange. Other peaks can appear at multiples of the operating frequency and correspond to multi-photon exchange.

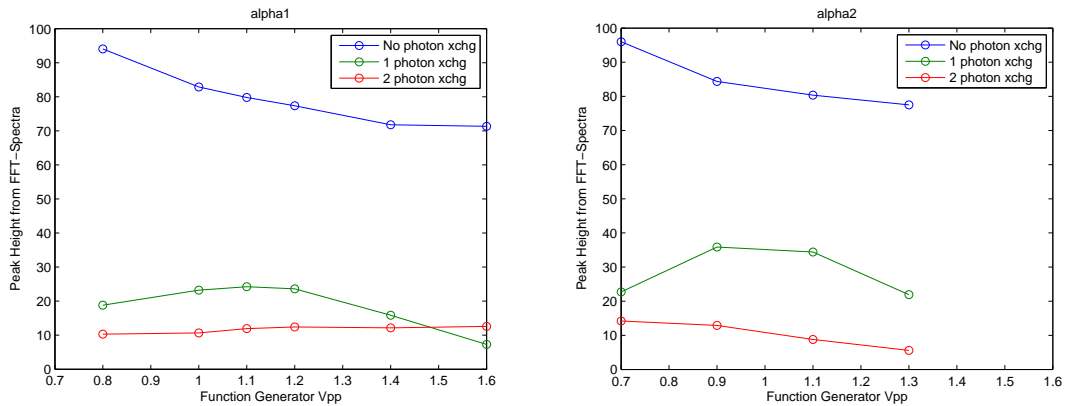


Figure 5.15: Plots of peak height extracted from above FFT-spectra against function generator voltage.

To compare the FFT data with the expected amplitudes for the energy-shifted components of the wavefunction, namely the Bessel functions, the peak heights of the FFT spectra were plotted against the peak to peak voltage of the function generator fig. 5.15. The plots are to be taken with skepticism, since the zero frequency peak height, i.e. the amplitude for no photon exchange, is also influenced by the incoherent part of the intensity, as well as by the problematic count rate of the small detectors without neutrons. The incoherent part of the intensity is also responsible for the reduced contrast of the interferometer.

The value chosen for the final experiment is 0.6 Vpp for both coils, test measurements for 0.5 Vpp can be seen in fig.5.16 and fig.5.17 together with the time-dependent histograms. These measurements took place after the temperature regulation of the interferometer chamber had a breakdown under conditions of worse contrast, as is mentioned later on. The final amplitude values are chosen because the FFT shows good peak height at the corresponding frequencies $\omega_I = 26$ kHz and $\omega_{II} = 22$ kHz and no or small peaks at multiples of that frequencies (higher order effects).

From the behaviour of the graph in fig. 5.15 for one photon exchange (green line), a rough approximation of the parameters α_j can be extracted. Since the first maximum of $J_1(\alpha)$ is located at $\alpha \approx 1.84$ and the maxima of the plots in fig. 5.15

lie at around 1 to 1.2 Vpp, the experimental values for α_j (corresponding to 0.6 Vpp) must be below 1, when assuming the relation between function generator driving voltage and oscillating magnetic field strength B_1 to be linear. For this reason a crude guess approximates them to be at $\alpha_j \approx 0.9$. This would lead to an overlapping of wavefunctions for $\alpha_j = 0$ and $\alpha_j = 0.9$ of $\sim 80\%$.

The occurrence of peaks with frequencies double or even triple the frequencies of the EM-coils corresponds to higher order terms of eq. (3.24) and is an indicator that the intensity oscillation is really caused by the effect in question. In addition to the one photon exchange also multi-photon exchange is possible. The linear order approximations used in order to arrive at the oscillating intensity eq. (3.36) do not cover the multi-photon effects, which can cause the intensity to oscillate with double or even triple the frequency of the EM-coil.

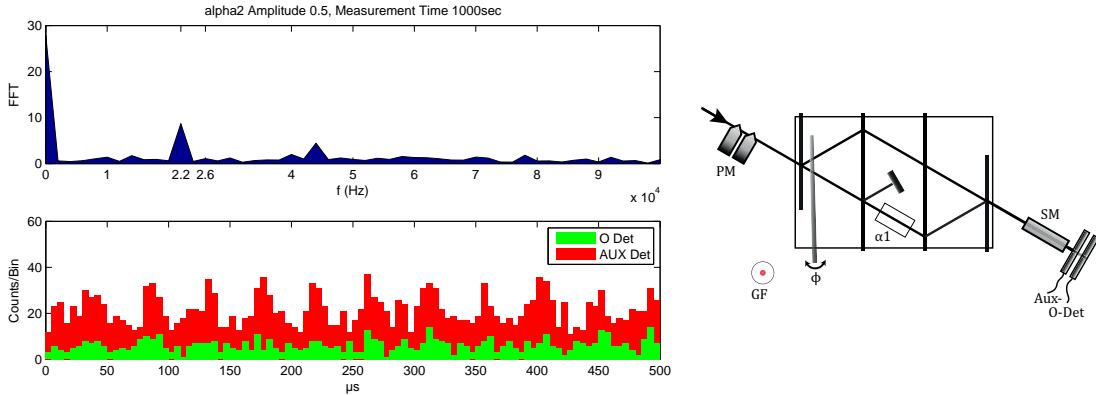


Figure 5.16: Test of α_I , function generator amplitude 0.5 Vpp, binwidth 5 μs , loop time 500 μs , measurement time 1000 s.

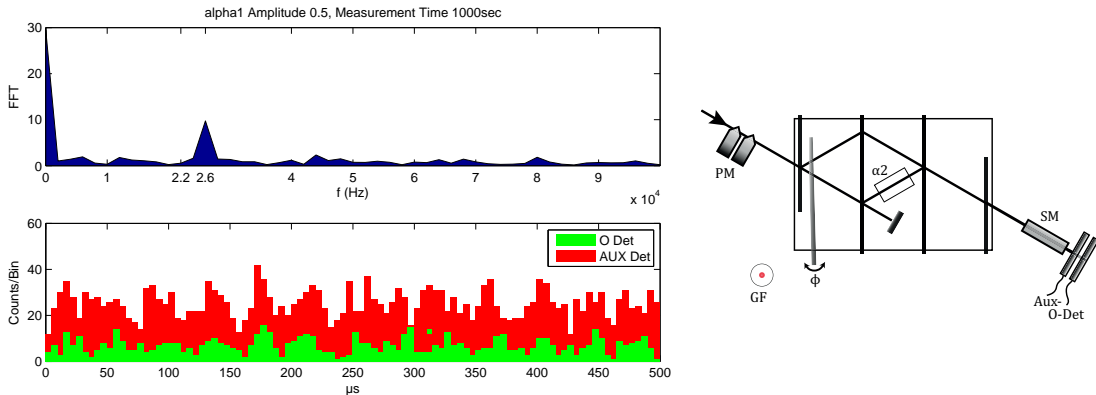


Figure 5.17: Test of α_{II} , function generator amplitude 0.5 Vpp, binwidth 5 μs , loop time 500 μs , measurement time 1000 s.

5.5 Phase Shifter Scans

Before the final measurement the phase shifter angles ϕ and χ , as defined in eq. (4.2), are set to the required values. First, the phase shifter χ in the back is scanned while the reference beam is blocked with a cadmium plate (fig. 5.18). Then the middle beam II is blocked and the 30% absorber introduced into the reference beam for the ϕ scan (fig. 5.19). Both scans are done using the big O detector to avoid electronic noise from the smaller detectors.

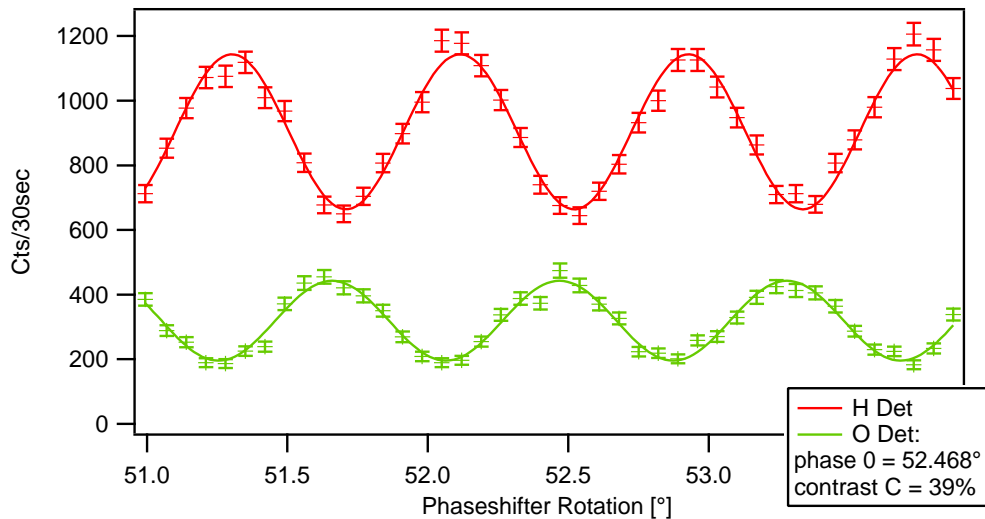


Figure 5.18: χ scan before final measurement.

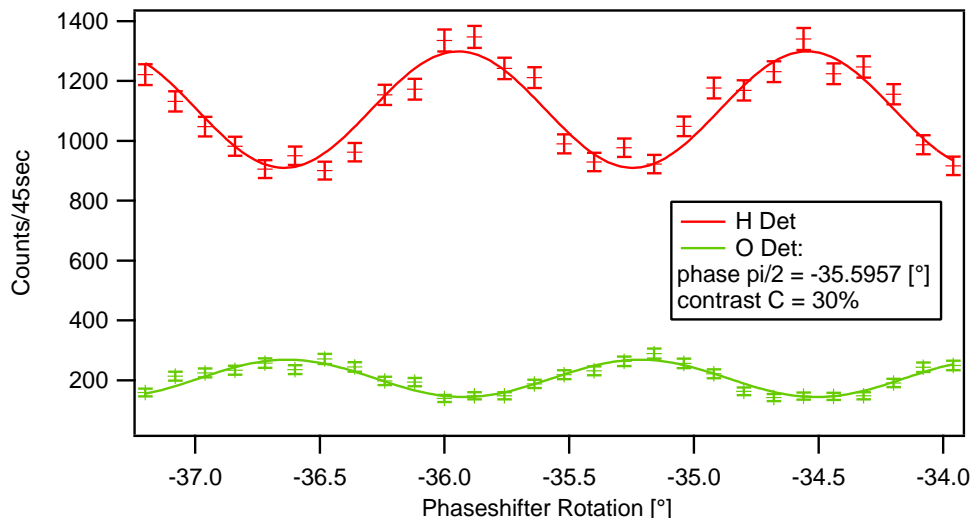


Figure 5.19: ϕ scan before final measurement. The contrast with an inserted absorber is reduced by a factor of $\sqrt{T_{abs}}$, therefore the contrast without absorber would be $30\%/\sqrt{0.3} \approx 54\%$.

The interferograms have different periods of the oscillation, because the two phase shifters in the front and back of the interferometer are made out of different materials, sapphire and silicon, with different widths. The counts per second for the scan of ϕ are lower than for χ , because the 30% absorber is present in one path.

6 Results

Unfortunately, the night before the final measurement, the temperature regulation of the interferometer setup had a breakdown. It took about half a day for the system to stabilize again and the contrast did not return completely. Before the measurement, the phase shifters are set to the required positions $\chi = 0$ and $\phi = \pi/2$. Then, the time-dependent measurements are started automatically in the order: 'all on', ' β_I off', ' β_{II} off', ' α_{II} off' and ' α_I off', each taking 1.5 hours, using the $1/4''$ detectors in the O beam. Afterwards, a second round of measurements is carried out using the big O detector, where the intensity is averaged over a period of 600 seconds, in order to compensate the blind count rate fluctuations of the $1/4''$ detectors.

Parameters of the final measurement are:

- final contrast: $C_\chi \approx 39\%$ for phase shifter χ and
 $C_\phi \approx 54\%$ for ϕ
- $\alpha_I \approx 0.9$ function generator amplitude 0.6 Vpp
 $\omega_I = 2\pi * 26$ kHz
- $\alpha_{II} \approx 0.9$ function generator amplitude 0.6 Vpp
 $\omega_{II} = 2\pi * 22$ kHz
- $\beta_I = \beta_{II} = 15^\circ \approx 0.26$ rad
 $\omega_{RF} = 2\pi * 60$ kHz
- $T_{abs} \approx 0.3$

single beam intensities (counts/180 s):

ref. beam (with T_{abs})	beam I	beam II
320	916	1018

- blind count rate of the small detectors after the final measurement (counts/300 s):

small O	Aux
92	51

Again I give the expression for the expected intensity of the O beam (eq. (3.36)):

$$I_O \propto 1 + \frac{T_{abs}}{2} + \beta_I \cos \chi + \sqrt{2 T_{abs}} (\cos \phi + \alpha_{II} \cos \omega_{II} t \sin \phi)$$

When the values for the phase shifter angles $\chi = 0$ and $\phi = \pi/2$ are put into this intensity, the result becomes:

$$I_O \propto 1 + \frac{T_{abs}}{2} + \beta_I + \alpha_{II} \sqrt{2 T_{abs}} \cos \omega_{II} t \quad (6.1)$$

To recapture, parameters α_I and β_{II} do not appear in this intensity and should not induce a change when they are switched on and off. Parameter α_{II} is expected to cause an intensity oscillation with frequency ω_{II} , however it does not change the mean intensity recorded over a longer time interval, since the cosine term is centered at zero. Only when β_I is switched off, the intensity is expected to decrease significantly.

In order to compare the final measurements with the expected behavior, a calculation using the estimated experimental parameters is carried out. An expression of the O beam intensity is evaluated as in eq. (3.33), by taking the absolute square of the wavefunction and approximating the matrices \mathcal{U}_{RF} and \mathcal{U}_{EM} up to second order in $\alpha_j = 0.9 * \delta_{\alpha_j}$ and $\beta_j = 0.26 * \delta_{\beta_j}$, also using the value for $T_{abs} = 0.3$. In this notation the variables δ_{ij} can either be one, when the perturbation is switched on, or zero when it is off. The incident wavefunction in this calculation is normalized to $|\langle \Psi_0 | \Psi_0 \rangle|^2 = 3$. Finally, if numerical coefficients in the resulting expression under $\frac{1}{10}$ are neglected, the result reads

$$I_O \propto 1 + 0.15 + 0.26 * \delta_{\beta_I} + 0.69 * \delta_{\alpha_{II}} \cos \omega_{II} t, \quad (6.2)$$

where the terms have the same order as in the expression directly above. Now this numerical result needs to be corrected for the contrasts $C_\chi = 0.39$ and $C_\phi = 0.54$, which can easily be done by introducing these values as factors in front of the terms, where originally the trigonometric functions with arguments χ and ϕ have been. This yields

$$I_O \propto 1 + 0.15 + 0.10 * \delta_{\beta_I} + 0.37 * \delta_{\alpha_{II}} \cos \omega_{II} t, \quad (6.3)$$

which is a numerical expression that can be compared with the final measurements.

6.1 Data

The time dependent measurement results for the five cases: 'all on', ' α_I off', ' α_{II} off', ' β_{II} off' and ' β_I off' are plotted in figs. 6.2–6.6 as histograms together with the corresponding FFT spectra. In fig. 6.1 the time independent measurement of the mean intensity over 600 seconds with the big O detector is depicted for these five case.

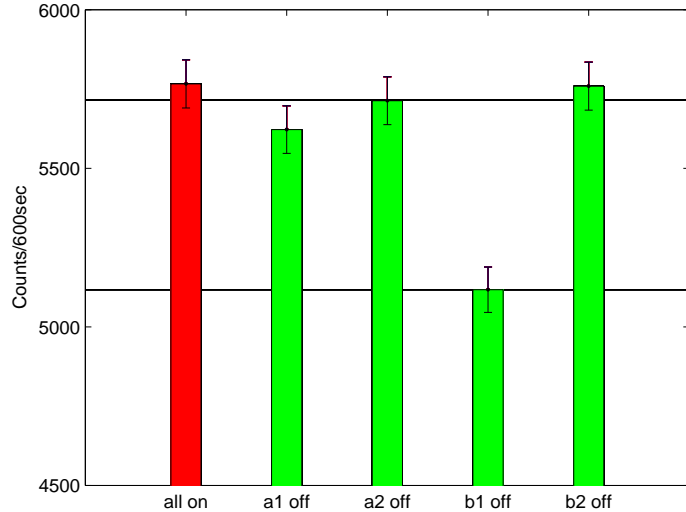


Figure 6.1: Counts per 600 s, measured with big O detector.

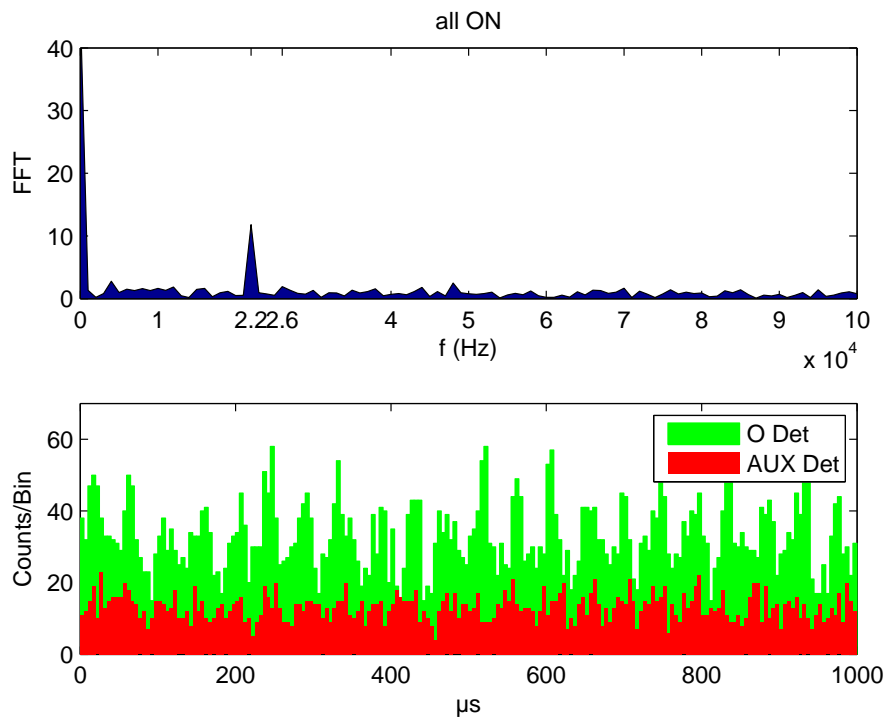


Figure 6.2: α_I , α_{II} , β_I , β_{II} turned on, loop time 1000 μ s, binwidth 5 μ s, measurement time 1.5 h. Measured with two 1/4" detectors.

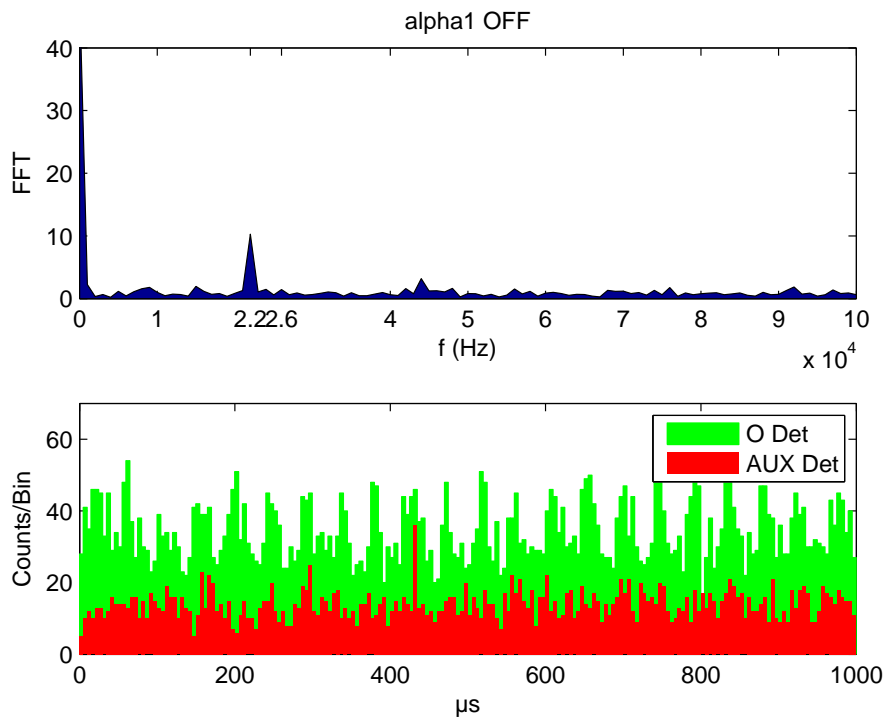


Figure 6.3: α_I turned off, loop time $1000 \mu\text{s}$, binwidth $5 \mu\text{s}$, measurement time 1.5 h . Measured with two $1/4''$ detectors.

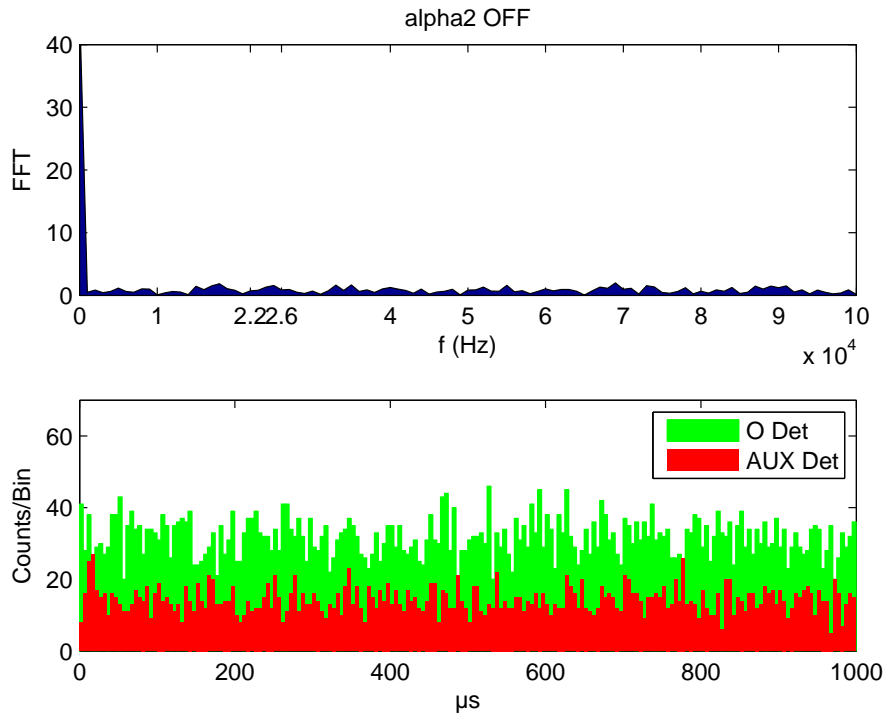


Figure 6.4: α_{II} turned off, loop time $1000 \mu\text{s}$, binwidth $5 \mu\text{s}$, measurement time 1.5 h . Measured with two $1/4''$ detectors.

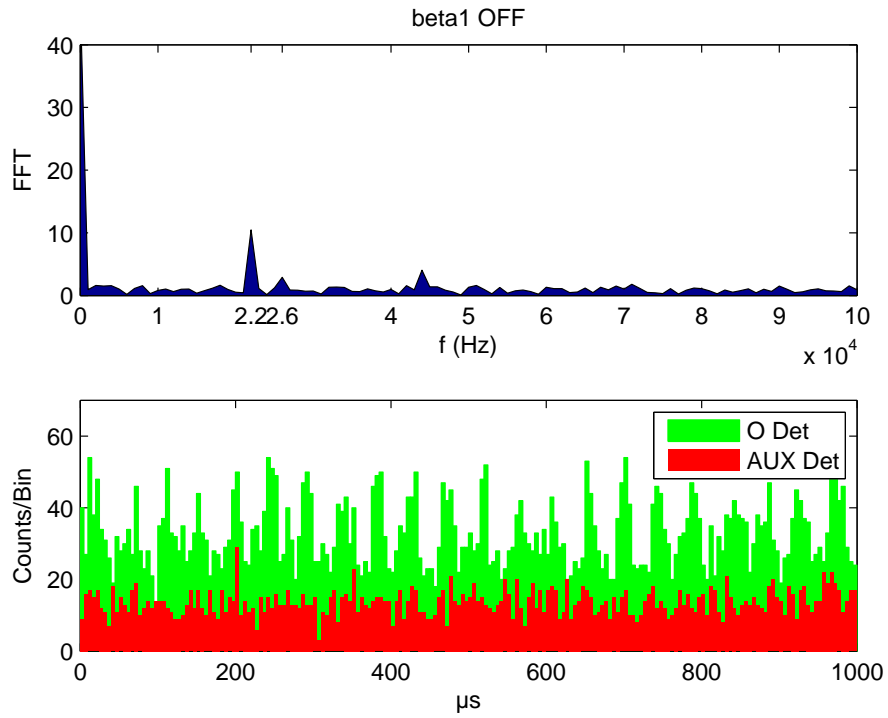


Figure 6.5: β_I turned off, loop time $1000 \mu\text{s}$, binwidth $5 \mu\text{s}$, measurement time 1.5 h . Measured with two $1/4''$ detectors.

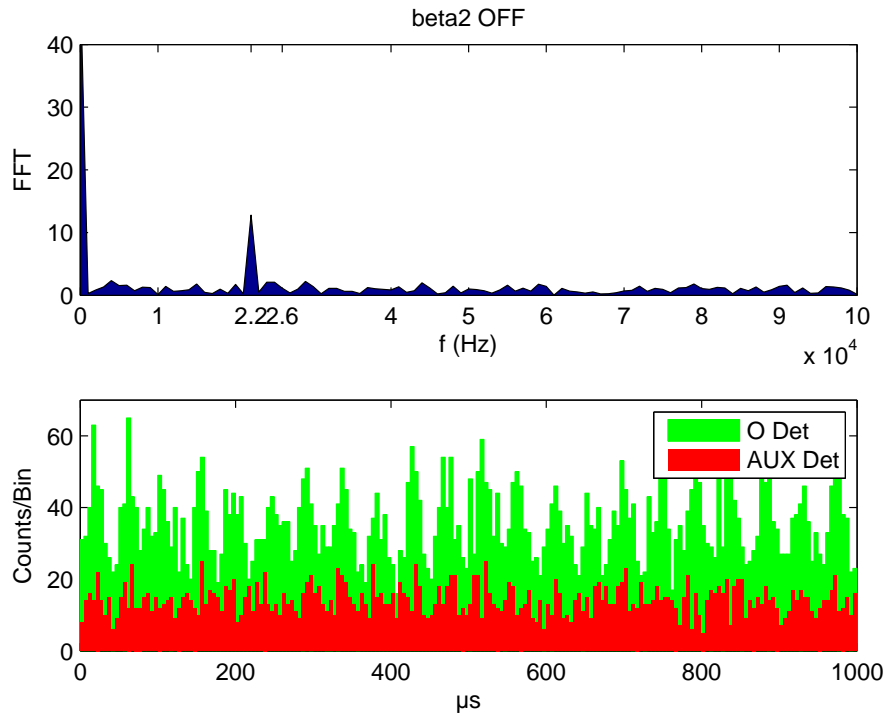


Figure 6.6: β_{II} turned off, loop time $1000 \mu\text{s}$, binwidth $5 \mu\text{s}$, measurement time 1.5 h . Measured with two $1/4''$ detectors.

6.2 Discussion

The overall behaviour is qualitatively in accordance with eq. (3.36), meaning the intensity goes down, when magnetic perturbation β_I is switched off (see fig. 6.1) and no oscillation of the intensity in time can be seen when the energetic perturbation α_{II} is switched off (fig. 6.3), although in measurements when α_{II} is switched on, a distinct peak in the FFT spectrum at 22 kHz can be seen. Other influences leave the system more or less unchanged.

One can see that the intensity for the case ' α_I off' is slightly diminished in comparison to the other three cases where the intensity should be unchanged. This can be explained by the fact, that the energy manipulator coils in reality do not completely leave the spin unchanged. Therefore a slight rotation away from the $|\uparrow_z\rangle$ state caused by α_I introduces a small amount of spins $|\uparrow_z\rangle$ where there should be almost none after the RF- π -flip. When α_I is turned off this effect vanishes and so the intensity goes down slightly.

Quantitatively, the reduction in counts per 600 s from 5766 for 'all on' to 5117 for ' β_I off', which is roughly 11% is in good agreement with the intensity estimation using experimental parameters (eq. (6.3)), which approximates it as $\frac{0.10}{1+0.15+0.10} = 8\%$.

The amplitude of the time-dependent intensity oscillation is a little bit harder to compare with the measurements. A comparison between the FFT spectra and cosine fits of the form $a + b \cos(2\pi ft + c)$ to the data (see fig. 6.7) reveals their connection to each other. The FFT peak at zero frequency is equal to the average number of counts per bin and the peak at 22 kHz is equal to the amplitude of the fitted cosine function with the same frequency, as summarized in the table below. The advantage of the fits is that they give a direct value for the error.

Counts/Bin	FFT peak height		cosine fit parameters	
	0 kHz	22 kHz	average counts a	amplitude of 22 kHz osc. b
all on	46.22	11.80	46.22 ± 1.01	11.80 ± 1.44
α_I off	48.6	10.28	48.62 ± 1.01	10.30 ± 1.40
β_I off	46.53	10.46	46.54 ± 1.08	10.48 ± 1.52
β_{II} off	50.10	12.79	50.10 ± 1.06	12.80 ± 1.49

Table 6.1: Comparison between FFT peaks and cosine fits to the time-dependent data. The case ' α_{II} off' cannot be fitted, since it shows no oscillation in time corresponding to a distinct frequency.

Now the background count rate due to electronic noise has to be subtracted from the time resolved data. The average of such counts per bin for the measurement time of 1.5 h is calculated as $\frac{92+51}{300}$ cts/s * 1000 bins * 5 μ s * 1.5 * 3600 s = 12.87 for

the sum of both detector counts. When this value is subtracted from the average number of counts per bin, e.g. for the case 'all on', which gives $46.22 - 12.87 = 33.35$ the result can be related to the amplitude of the 22 kHz oscillation, i.e. $\frac{11.80}{33.35} \approx 0.35$ which is in good agreement with the numerical estimate from eq. (6.3), namely $\frac{0.37}{1+0.15} \approx 0.32$.

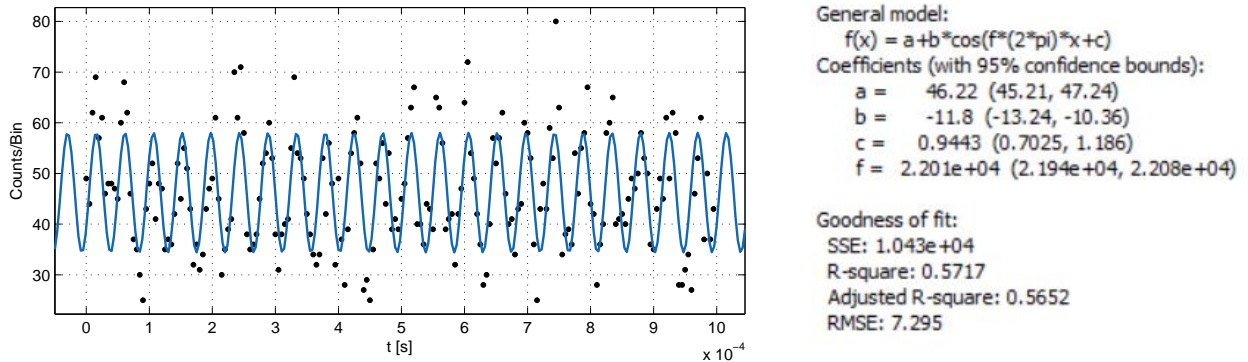


Figure 6.7: One of the cosine fits to the time-dependent count rate of both small detectors for the case of 'all on'.

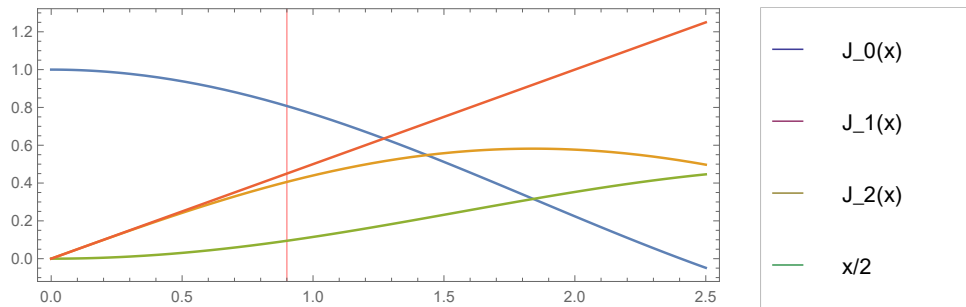


Figure 6.8: The first three Bessel functions $J_n(x)$ and the first order approximation for $J_1(x) \approx \frac{x}{2}$. Vertical red line at $x = 0.9$ where the parameters α_j are estimated to be.

A comparison of the Bessel functions and their linear approximation used in the calculations with \mathcal{U}_{EM} is presented in fig. 6.8. The deviation of $J_1(0.9)$ from $\frac{0.9}{2}$ is less than 10%, but the deviation of $J_0(0.9)$ from 1 is almost 20% and $J_2(0.9) \approx 0.1$. A better value for the strength of the EM-coils would be $\alpha_j = 0.5$, which would give $J_0(0.5) \approx 0.94$, $J_1(0.5) \approx 0.24$ and $J_2(0.5) \approx 0.03$. Together with a 10% absorber the resulting intensity oscillation would be (see eq. (6.1))

$\alpha_{II}\sqrt{2T_{abs}} = 0.5 * \sqrt{2 * 0.10} \approx 0.22$, limited by contrast, which under ideal practical circumstances can be up to $C \approx 70\%$, to $0.7 * 0.22 \approx 0.16$. A change in the intensity due to $C\beta_I \approx 0.16$ that has the same magnitude would in turn be caused by a magnetic rotation angle of $\beta_I \sim 13^\circ$.

The relative error of an intensity oscillation in time can alternatively be calculated as $\frac{\sqrt{N}}{N} = \frac{1}{\sqrt{N}}$, when N is the number of counts per bin, with which the intensity oscillates, and the error is given by the Poisson statistics, which neutron counting events obey. In the time-dependent measurement of 'all on' this amounts to $\frac{1}{\sqrt{11.80}} \approx 0.29$. Now, when the same average count rate of 33.35/bin/1.5h is assumed, a relative count rate oscillation of amplitude 0.16 would give $N = 0.16 * 33.35 \approx 5.34$. Then, in order to have the same relative error, the measurement time would have to be increased, so that $1/\sqrt{5.34 \frac{t}{1.5h}} = 0.29$. This gives $t \approx 3.34$ h, therefore, for the same relative error or better, the time-dependent measurement would have take upwards of 3.34 h.

7 Conclusion and Outlook

Inspired by the first experimental demonstration of the quantum Cheshire Cat effect by Denkmayr et al. using neutron interferometry in 2014 [7], a new experiment was explored, that seeks to demonstrate the same effect using four localized perturbations which all act simultaneously and are of unitary nature. The four perturbations exist to probe the interferometer quantum state, which is subject to pre and postselection, for the localization of its spin and path degree of freedom.

In order to measure the path degree of freedom, a novel experimental approach was implemented, that makes use of the neutron’s energy state by causing an energy shift dependent on the path, without a change of the spin state. This approach is inspired by multiphoton exchange processes observed in [10].

By switching off only one of the four perturbations, one after the other, an appreciable effect is only caused by two of them, effective on opposite paths of the interferometer. On path I, the spin is influenced by a small additional spin rotation, leading to an O beam intensity increase for the pre and postselected ensemble. On path II, a local magnetic field in the z-direction, oscillating with frequency ω_{II} , causes a shift in energy without turning the spin. The energy shifted beam leads to an oscillation of the O beam intensity with the same frequency, when it shows interference with an additional reference beam weakened by an absorber with transmittance $T_{abs} \approx 30\%$. The other two perturbations, which have no measurable effect on the intensity, are of the same nature as just described, only on opposite paths.

The measurement results qualitatively suggest the neutron’s spin degree of freedom to be spatially separated from its path degree of freedom, given pre and postselection, which is known as the Cheshire Cat paradox.

In the future, the experiment could be repeated with weaker interactions and a stronger absorber with $T_{abs} = 10\%$ in order to better fulfill the linear order approximations for the perturbations of energy (α_I, α_{II}) and spin (β_I, β_{II}) on the two paths, used in the weak measurement scheme. The adjustment of the EM-coils should be carried out with higher accuracy in order to reach a better quantitative agreement between theory and experiment. Under these conditions, assuming contrasts of $C = 70\%$, in order to have influences onto the intensity on the order of 1/10, the parameters for the perturbations should be reduced to $\alpha_j = 0.5$ and $\beta_j = 0.22 \approx 13^\circ$. In this case, the measurement time for the time dependent measurements would have to take upwards of ~ 3.5 h.

Bibliography

- [1] D. Greenberger, K. Hentschel and F. Weinert, *Compendium of quantum physics: concepts, experiments, history and philosophy* (Springer Science & Business Media, 2009).
- [2] J. Von Neumann, *Mathematical foundations of quantum mechanics* 2 (Princeton university press, 1955).
- [3] H. Rauch and S. A. Werner, *Neutron Interferometry: Lessons in Experimental Quantum Mechanics, Wave-Particle Duality, and Entanglement* (Oxford University Press, USA, 2015).
- [4] P. R. Berman and V. Kharchenko, Atom interferometry (1997).
- [5] Y. Aharonov, D. Z. Albert and L. Vaidman, How the result of a measurement of a component of the spin of a spin-1/2 particle can turn out to be 100, *Phys. Rev. Lett.* **60**, 1351 (1988).
- [6] J. Klepp, S. Sponar and Y. Hasegawa, Fundamental phenomena of quantum mechanics explored with neutron interferometers, *Progress of Theoretical and Experimental Physics* **2014**, 082A01 (2014).
- [7] T. Denkmayr, H. Geppert, S. Sponar, H. Lemmel, A. Matzkin, J. Tollaksen and Y. Hasegawa, Observation of a quantum Cheshire Cat in a matter-wave interferometer experiment, *Nature communications* **5** (2014).
- [8] L. Carroll and J. Pertwee, *Alice in wonderland* (Children's Press, 1947).
- [9] H. Geppert-Kleinrath, *Experimental studies of a Bell-like inequality and a which-way measurement in neutron interferometry*. Ph.D. thesis, Technische Universität Wien (2017).
- [10] J. Summhammer, K. A. Hamacher, H. Kaiser, H. Weinfurter, D. L. Jacobson and S. A. Werner, Multiphoton Exchange Amplitudes Observed by Neutron Interferometry, *Phys. Rev. Lett.* **75**, 3206 (1995).
- [11] S. Sponar, T. Denkmayr, H. Geppert and Y. Hasegawa, Fundamental Features of Quantum Dynamics Studied in Matter-Wave Interferometry—Spin Weak Values and the Quantum Cheshire-Cat, *Atoms* **4**, 11 (2016).

- [12] Y. Aharonov and D. Rohrlich, *Quantum paradoxes: quantum theory for the perplexed* (John Wiley & Sons, 2008).
- [13] Y. Aharonov, S. Popescu, D. Rohrlich and P. Skrzypczyk, Quantum cheshire cats, *New Journal of Physics* **15**, 113015 (2013).
- [14] D. P. Atherton, G. Ranjit, A. A. Geraci and J. D. Weinstein, Observation of a classical Cheshire cat in an optical interferometer, *Optics letters* **40**, 879 (2015).
- [15] J. M. Ashby, P. D. Schwarz and M. Schlosshauer, Observation of the quantum paradox of separation of a single photon from one of its properties, *Phys. Rev. A* **94**, 012102 (2016).
- [16] I. Duck, P. Stevenson and E. Sudarshan, The sense in which a "weak measurement" of a spin-1/2 particle's spin component yields a value 100, *Physical Review D* **40**, 2112 (1989).
- [17] J. Dressel, M. Malik, F. M. Miatto, A. N. Jordan and R. W. Boyd, Colloquium: Understanding quantum weak values: Basics and applications, *Reviews of Modern Physics* **86**, 307 (2014).
- [18] J. S. Lundeen, B. Sutherland, A. Patel, C. Stewart and C. Bamber, Direct measurement of the quantum wavefunction, *Nature* **474**, 188 (2011).
- [19] P. B. Dixon, D. J. Starling, A. N. Jordan and J. C. Howell, Ultrasensitive Beam Deflection Measurement via Interferometric Weak Value Amplification, *Phys. Rev. Lett.* **102**, 173601 (2009).
- [20] R. Corrêa, M. F. Santos, C. Monken and P. L. Saldanha, 'Quantum Cheshire Cat'as simple quantum interference, *New Journal of Physics* **17**, 053042 (2015).
- [21] Q. Duprey, S. Kanjilal, U. Sinha, D. Home and A. Matzkin, The Quantum Cheshire Cat effect: Theoretical basis and observational implications, *arXiv preprint arXiv:1703.02959* (2017).
- [22] W. H. Kraan, *Instrumentation to handle thermal polarized neutron beams*. Ph.D. thesis, TU Delft, Delft University of Technology (2004).
- [23] S. V. Grigoriev, W. H. Kraan, F. M. Mulder and M. T. Rekveldt, Neutron-wave-interference experiments with two resonance coils, *Phys. Rev. A* **62**, 063601 (2000).

- [24] J. Summhammer, Coherent multiphoton exchange between a neutron and an oscillating magnetic field, *Phys. Rev. A* **47**, 556 (1993).
- [25] T. Denkmayr, H. Geppert, H. Lemmel, M. Waegell, J. Dressel, Y. Hasegawa and S. Sponar, Experimental Demonstration of Direct Path State Characterization by Strongly Measuring Weak Values in a Matter-Wave Interferometer, *Phys. Rev. Lett.* **118**, 010402 (2017).
- [26] H. Geppert, T. Denkmayr, S. Sponar, H. Lemmel and Y. Hasegawa, Improvement of the polarized neutron interferometer setup demonstrating violation of a Bell-like inequality, *Nuclear Instruments and Methods in Physics Research Section A: Accelerators, Spectrometers, Detectors and Associated Equipment* **763**, 417 (2014).